Universitá degli Studi di Pavia
Facoltá di Ingegneria
Dipartimento di Meccanica Strutturale

Corso di Laurea Specialistica in Ingegneria Biomedica

Stent Fatigue Life Prediction: an analytical and experimental approach

Tesi di Laurea di
Umberto Bargiggia

Relatore:
Chiar.mo Prof.
Ferdinando Auricchio ....

Correlatore:
Ing. Michele Conti . . ..

Candidato:
Umberto Bargiggia

Anno Accademico 2007/2008

A mia madre e mio padre

Abstract

Stents are tubular devices which are implanted in atherosclerotic vessels to restore their original lumen. These endovascular devices are subjected to the repeated loads induced by vessel deformation under diastolic and systolic pressure.

Fatigue is the process of progressive, localized, permanent, structural change occurring in a material subjected to conditions which produce fluctuating stresses and strains at some point or points and that may culminate in cracks or complete fracture, after a sufficient number of fluctuations.

Recently fatigue failure has emerged as one main cause of stent drawback particularly in high deformable peripheral vessels as Superficial Femoral Artery or Carotid Artery. Consequently fatigue life of stent can influence the clinical outcomes and clearly the assessment of stent fatigue life endurance is an important issue of stent design.

For a correct stent fatigue life prediction it is necessary to consider the synergetic utilization of experimental evaluation and analytic calculation of such variables and parameters which describe fatigue phenomenon.

The aim of the present work is to define a framework to investigate fatigue life of a metallic stent using analytical, experimental and numerical methods. Firstly, a literature review is performed to define an analytical method able to evaluate the initial dimension and orientation of a macrocrack. Moreover the methodology to evaluate fatigue macrocrack propagation to final device failure is discussed.

Secondly, a customized fatigue test machine is designed in order to evaluate the fatigue behaviour of stent material.

Finally a demonstration of the developed framework is performed evaluating the fatigue life of metallic coronary stent (Cypher stent, Cordis corporation, NJ, USA) using Finite Element Method to evaluate the stent stress state under a cardiac cycle.

The developed framework allows the evaluation of stent fatigue life considering the position, the size and the orientation of the macrocrack.

Further improvements will take into account the fatigue characterization of the stent material by the designed customized machine and the experimental validation.

Contents

List of Figures

List of Tables

Abbreviations and Symbols

Chapter 1

$R \longrightarrow$ load ratio
$\Delta S \longrightarrow$ stress range
$S_a \longrightarrow$ stress amplitude
$S_m \longrightarrow$ mean stress
$N_f \longrightarrow$ number of cycles to failure
$N_i \longrightarrow$ number of cycles to crack initiation
$N_p \longrightarrow$ number of cycles to crack propagation
$LCF \longrightarrow$ low cycles fatigue
$HCF \longrightarrow$ high cycles fatigue
$CF \longrightarrow$ corrosion fatigue
$S_y \longrightarrow$ yield stress
$K_c \longrightarrow$ fracture toughness
$S_e \longrightarrow$ endurance limit
$K \longrightarrow$ stress intensity factor
$S \longrightarrow$ applied stress
$a \longrightarrow$ crack length
$f(g) \longrightarrow$ specimen shape function
$w \longrightarrow$ specimen width
$\delta K \longrightarrow$ stress intensity factor range
$da/dN \longrightarrow$ crack growing size during a cycle
$c \longrightarrow$ Paris law coefficient
$n \longrightarrow$ Paris law exponent
$K_{max} \longrightarrow$ maximum stress intensity factor
$K_c \longrightarrow$ stress intensity factor value for static failure
$MFM \longrightarrow$ Microstructural Fracture Mechanics

$S_f \longrightarrow$ true fracture strength
$b \longrightarrow$ fatigue strength
$S_{TS} \longrightarrow$ tensile strength stress
$S_U \longrightarrow$ ultimate strength stress
$\varepsilon \longrightarrow$ strain
$\Delta\varepsilon \longrightarrow$ stress range

Chapter 2

$CDM \longrightarrow$ continuum damage mechanics
$\vec{n} \longrightarrow$ normal to the RVE cutting plane
$RVE \longrightarrow$ representative volume element
$D \longrightarrow$ damage variable
$S \longrightarrow$ free area
$S_D \longrightarrow$ damaged area
$\sigma_{ij} \longrightarrow$ stress
$\varepsilon_{ij} \longrightarrow$ strain
$\tilde{\sigma} \longrightarrow$ effective stress
$T \longrightarrow$ temperature
$s \longrightarrow$ entropy associated variable
$\varepsilon_{ij}^{p} \longrightarrow$ plastic strain
$r, R \longrightarrow$ hardening variables
$\alpha_{ij}, X_{ij} \longrightarrow$ kinematic hardening variables
$Y \longrightarrow$ damage associated variable
$\psi \longrightarrow$ Helmoltz specific free energy
$\psi_e \longrightarrow$ elastic Helmoltz specific free energy contribution
$\psi_p \longrightarrow$ plastic Helmoltz specific free energy contribution
$\psi_T \longrightarrow$ thermal Helmoltz specific free energy contribution
$\psi^{\star} \longrightarrow$ Gibbs free enthalpy
$C \longrightarrow$ linear kinematic hardening parameter
$\omega_s \longrightarrow$ stored energy
$\rho \longrightarrow$ density
$F \longrightarrow$ dissipation potential
$f \longrightarrow$ plastic criterion function
$F_X \longrightarrow$ non linear kinematic hardening
$\lambda \longrightarrow$ plastic multiplier

$p \longrightarrow$ plastic multiplier with von Mises stress
$E \longrightarrow$ Young's modulus
$\nu \longrightarrow$ Poisson's ratio
$\alpha \longrightarrow$ thermal expansion coefficient
$\sigma_{TH} \longrightarrow$ hydrostatic stress
$\sigma_{eq} \longrightarrow$ von Mises equivalent stress
$\sigma_{ij}^{D} \longrightarrow$ stress deviator
$\sigma_H/\sigma_{eq} \longrightarrow$ stress triaxiality
$\omega_D \longrightarrow$ stored energy threshold
$D_c \longrightarrow$ damage critical value
$\sigma_f^{\infty} \longrightarrow$ asymptotique fatigue limit
$\sigma_u \longrightarrow$ ultimate stress
$\varepsilon_p^{D} \longrightarrow$ strain threshold for damage initiation
$A, m \longrightarrow$ material parameters
$R_{\infty}, b, C, \gamma, X_{\infty} \longrightarrow$ hardening parameters
$\sigma_R \longrightarrow$ rupture stress
$Z \longrightarrow$ necking parameter
$N_R \longrightarrow$ number of crack for mesocrack initiation
$FEM \longrightarrow$ finite element analysis
$SED \longrightarrow$ strain energy density method
$\delta_0 \longrightarrow$ initial crack length

Chapter 3

$G_c \longrightarrow$ critical amount of energy required for crack opening
$K \longrightarrow$ stress intensity factor
$S-N \longrightarrow$ stress stress based approach
$\varepsilon-N \longrightarrow$ strain based approach
$\Delta S \longrightarrow$ stress range
$\Delta K \longrightarrow$ stress intensity factor range
$LEFM \longrightarrow$ linear elastic fracture mechanics
$EPFM \longrightarrow$ elasto$-$plastic fracture mechanics
$U_0 \longrightarrow$ strain energy density
$S \longrightarrow$ applied stress
$E \longrightarrow$ Young's modulus
$V \longrightarrow$ volume
$a \longrightarrow$ crack length

$B \longrightarrow$ crack thickness
$U \longrightarrow$ total energy realesed from the body
$W \longrightarrow$ adsorbed surface energy
$\gamma_s \longrightarrow$ surface area
$\gamma_{eff} \longrightarrow$ plastic energy adsorption around the crack tip
$r \longrightarrow$ distance from crack tip
$\theta \longrightarrow$ orientation from the distance
$K_I \longrightarrow$ stress intensity factor for Mode I opening
$K_{II} \longrightarrow$ stress intensity factor for Mode II opening
$K_{III} \longrightarrow$ stress intensity factor for Mode III opening
$K_{Ic} \longrightarrow$ fracture toughness for Mode I opening
$K_{IIc} \longrightarrow$ fracture toughness for Mode II opening
$K_{IIIc} \longrightarrow$ fracture toughness for Mode III opening
$T \longrightarrow$ traction
$J \longrightarrow$ line integral
$\Gamma \longrightarrow$ boundary contour

Chapter 4

$l \longrightarrow$ specimen length
$D \longrightarrow$ specimen diameter
$E_{aust} \longrightarrow$ austenitic Young's modulus
$E_{mart} \longrightarrow$ martensitic Young's modulus
$\varepsilon_{res} \longrightarrow$ residual stress
$F \longrightarrow$ applied load
$A \longrightarrow$ specimen section area
$F_{res} \longrightarrow$ resisting load
$C_{res} \longrightarrow$ resisting static applied torque
$t_a \longrightarrow$ time for 'Step I' realization
$v_m \longrightarrow$ medium speed
$\omega_{min} \longrightarrow$ minimum actuator I angular speed
$P \longrightarrow$ actuator I power
$s \longrightarrow$ gear wheel step
$th \longrightarrow$ gear wheel thickness
$a \longrightarrow$ gear wheel addendum
$d \longrightarrow$ gear wheel dedendum
$m \longrightarrow$ gear wheel modulus

$i \longrightarrow$ gear wheel transmission rate parameter
$\nu \longrightarrow$ actuator efficiency
$p \longrightarrow$ screw-nut step
$d_{maj} \longrightarrow$ screw major radius
$d_r \longrightarrow$ screw minor radius
$d_m \longrightarrow$ screw medium radius
$F_t \longrightarrow$ shear force
$R_{II} \longrightarrow$ actuator II power
$\omega_{reg} \longrightarrow$ actuator II regime speed
$R \longrightarrow$ primitive cam radius
$\alpha_0 \longrightarrow$ rest angle
$\alpha_s \longrightarrow$ slope angle
$\alpha_k \longrightarrow$ kept angle
$\alpha_r \longrightarrow$ return angle
$d_{II} \longrightarrow$ actuator II shaft diameter
$p_{max} \longrightarrow$ pressure acting on contact area
$P_{max} \longrightarrow$ maximum pawls surfaces pressure
$q \longrightarrow$ pawls surfaces applied load
$c \longrightarrow$ elastic gear wheels coefficient
$K_{spring} \longrightarrow$ Hook's elasticity coefficient
$FEA \longrightarrow$ Finite Element Analysis

Chapter 5

$d_0 \longrightarrow$ initial external stent diameter
$th \longrightarrow$ strut thickness
$d_{ext} \longrightarrow$ expanded diameter
$d_{recoil} \longrightarrow$ recoil diameter
$l_i \longrightarrow$ longitudinal initial length
$l_{exp} \longrightarrow$ longitudinal expanded length

Introduction

Stents are endosurgical devices commonly used to dilate vessels narrowed by an atherosclerotic plaque. These devices are usually associated with angioplasty and their implant has the goal to support the vessel avoiding the elastic recoil after vessel dilation.
Fatigue is the process of progressive, localized, permanent, structural change occurring in a material subjected to conditions which produce fluctuating stresses and strains at some point or points and that may culminate in cracks or complete fracture, after a sufficient number of fluctuations.
Recently fatigue failure has emerged as one main cause of stent drawback particularly in high deformable peripheral vessels as Superficial Femoral Artery or Carotid Artery.
In 10 years a stent will be subjected to about 400 million of heart beats, plus any other externally induced stress. Consequently FDA (Food and Drugs Administration) in order to ensure stent durability requires to simulate 10 years of a new stent design by in−vitro tests before to introduce it in the market.
The investigation of stent durability corresponds to fatigue life prediction where fatigue is the process of progressive material damaging leading to final failure.
Stent fatigue life prediction embodies two arguments with a huge social impact:

- Cardiovascular diseases are the first cause of death in the U.S.A and in Europe and stents are the most effective endosurgical device for therapeutic diseases approach. More than one million stents are implanted every years in human arteries exceeding 7 billion dollars by the year 2006 [17] ;

- Fatigue causes the 70% of structural failure [78].

The aim of the present work is to define a framework to investigate fatigue life of a metallic stent using analytical, experimental and numerical methods and is organized as follows:

- In Chapter 1, fatigue failure phenomenon will be presented from a qualitative point of view.
  Firstly, fatigue is defined and the main aspects characterizing fatigue failure are introduced. Subsequently, fatigue failure evolution, 'small fatigue cracks' and 'fatigue crack closure' are briefly discussed. Finally the most common fatigue design approaches are introduced providing also an overview of experimental procedures for fatigue life investigation and characterization.

- In Chapter 2, crack initiation dynamics is deeply investigated presenting mathematical model of 'J. Lemaitre' able to evaluate the evolution of the crack from initial microscopic scale to macroscopic one. To obtain a complete fatigue crack initiation analysis, a procedure based on 'Continuum Damage Mechanics'(CDM) is presented; it allows to evaluate the number of cycle for mesocrack initiation, initial macrocrack size and macrocrack orientation.
  For the purpose of this work, only the simplest application of the so called 'Theory of Damage' is presented.

- In Chapter 3, the connection between microscopic and macroscopic cracks is discussed and the variables to evaluate fatigue macrocrack evolution are defined.

- In Chapter 4, the design of a customized fatigue test machine is discussed. The machine is designed to be able also to perform fatigue tests on Nitinol wires since this shape memory alloys is used to form peripheral stents.

- In Chapter 5 a demonstration of the developed framework is performed evaluating the fatigue life of metallic coronary stent (Cypher stent, Cordis corporation, NJ, USA) using finite element method (FEM) to evaluate the stent stress state under a cardiac cycle.

Chapter 1

Fatigue of Materials

In this chapter, fatigue failure phenomenon will be presented from a qualitative point of view. First, fatigue will be defined and the main aspects that characterized fatigue failure will be introduced (i.e. load characterization and environmental conditions). Second, fatigue failure evolution will be presented, remanding at chapter 2 and 3 the mathematical formulation of the problem. A brief description of 'small fatigue cracks' and 'fatigue crack closure' will be treated in this chapter. Third, the most common design approaches will be introduced. Finally an overview on the experimental procedures for fatigue life investigation and characterization will be presented.

1.1 Introduction to Fatigue Phenomenon

Fatigue is the process of progressive, localized, permanent, structural change occurring in a material subjected to conditions which produce fluctuating stresses and strains at some point or points and that may culminate in cracks or complete fracture, after a sufficient number of fluctuations [1]. Fatigue damage results from the synergy of cyclic stress, tensile stress, and plastic strain; a fatigue crack will not initiate and propagate if any one of these three events is not present. Fatigue failure is dominated by two main aspects: applied load history and environmental conditions.

1.1.1 Load Characterization

Load characterization is fundamental to an appropriate fatigue evaluation, and there are essentially four classes of fatigue loading [2]:

- Constant Amplitude, Proportional Loading;
- Constant Amplitude, Non-Proportional Loading;
- Non-Costant Amplitude, Proportional Loading;
- Non-Costant Amplitude, Non-Proportional Loading.

The amplitude identifier underlines if the loading is a variant of a sine wave with a single load-ratio or if it varies randomly, with the load-ratio changing with time. Proportionality identifier, describes whether the changing load causes the principal stress axes to change. If the principal stress axes do not change, then it is proportional loading. If the principal stress axes do change, then the cycles cannot be counted simply and it is non-proportional loading.

Costant Amplitude, Proportional Loading : it describes a load which has a constant maximum and minimum value, which periodically varies with time. We could give the following definitions in function of S_{min} and S_{max}, which are respectively the minimum and the maximum applied stress:

- **Load-Ratio:** $R = (\frac{S_{min}}{S_{max}})$;
- **Stress-Range:** $\Delta S = (S_{max} - S_{min})$;
- **Stress-Amplitude:** $S_a = (\frac{S_{max}-S_{min}}{2})$;
- **Mean-Stress:** $S_m = (\frac{S_{max}+S_{min}}{2})$.

There are three basic types of constant-amplitude loading: 'tensile-to-tensile load' (Fig.1.1a), 'fully-reversed load' (Fig.1.1b), 'zero-to-full tensile load' (Fig.1.1c).

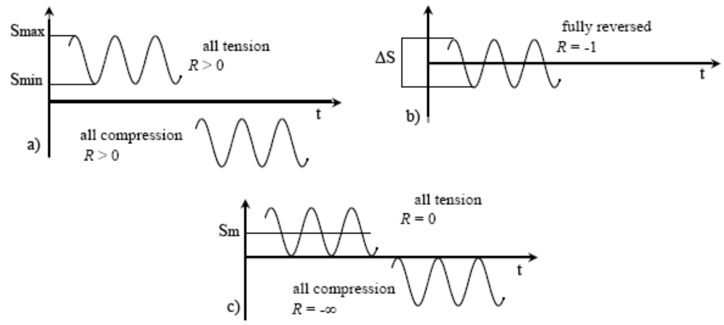

Figure 1.1: Example of constant amplitude, proportional loading. (a) 'tensile-to-tensile load', (b)'fully-reversed load', (c) zero-to-full tensile load'.

Costant Amplitude, Non-Proportional Loading : load shows constant amplitude but non-proportional, because of principal stress or strain axes are free to change between two different sets. Since the loading is non-proportional, the critical fatigue location may occur at a spatial location that is not easily identifiable by looking at both of the base loading stress states. This type of fatigue loading could describe common fatigue loadings as follows:

- Alternating between two distinct load cases (like a bending load and torsion load);
- Applying an alternating load superimposed on a static load;
- Every case where loading is proportional but results are not: this happens under conditions where changing the direction or magnitude of loads causes a change in the relative stress distribution in the specimen. This may be important in situations with non-linear contact and compression-only surfaces.

Non-Constant Amplitude, Proportional Loading : it describes a situation where instead of using a single R to calculate alternating and mean values, load-ratio becomes time-dependent (Fig.1.2). The fatigue loading which causes the maximum damage cannot easily be determined. Thus, cumulative damage calculations need to be

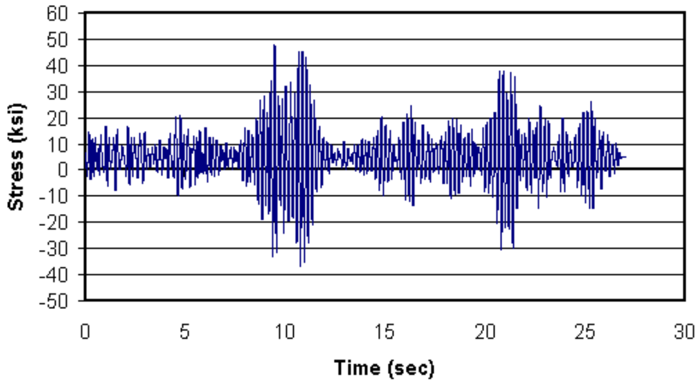

Figure 1.2: Example of non constant amplitude loading, varying with time.

done to determine the total amount of fatigue damage and which cycle combinations cause that damage. Cycle counting is a way to reduce a complex load-history into a number of events, which can be compared to available constant-amplitude data test.

Non-Constant Amplitude, Non-Proportional Loading : it is the most general case and is similar to constant amplitude, non-proportional loading, but in this loading class there are more than two different stress cases involved that have no relation between each other. Not only is the spatial location of critical fatigue life unknown, but also unknown is what combination of loads cause the most damage. Consequently, more advanced cycle counting method are required (e.g. path independent peak or multi-axial critical plane methods).

Fatigue failure as a consequence of cyclic stress history, allows to clarify fatigue as function of N_f . N_f identifies the fatigue life in terms of number of cycles for crack initiation, N_i, and number of cycles for crack propagation, N_p :

$$\mathbf{N_f} = (\mathbf{N_i} + \mathbf{N_p}) \tag{1.1}$$

The N_f associated to specimen fatigue life, allows to introduce the following definitions:

- **Low-Cycle Fatigue(LCF):** characterized by high amplitude cyclic stresses ($N_f \leq 10^4$ and $S \simeq S_c$); where S_c is the critical treshold to induce plastic deformations: fatigue life is markedly shortened.

- **High-Cycle Fatigue(HCF):** characterized by low amplitude cyclic stresses ($N_f \geq 10^5$ and $S << S_c$).

1.1.2 Environmental Impact in Fatigue Failure

Fatigue life is a function of stress-range, strain-range, mean stress and also of environment; there are two principal environmental conditions which accelerate fatigue phenomenon:

- 'Corrosion-Fatigue'(CF);
- 'Creep-Fatigue';

Corrosion-Fatigue(CF) is a term which is commonly used to underline the progressive damage and final failure of a material under the simultaneous action of cyclic stresses and any aggressive medium. In particular for our purposes we will refer in details at the effects of aqueous environments. CF includes two principal mechanisms of environmental damage:

- 'Anodic Slip Dissolution'
- 'Hydrogen Embrittlement'

Anodic slip dissolution causes advance in cracks by:

- Diffusion of the active species (e.g., water molecules or halide anions);
- Rupture of the protective oxide film at a slip step or in the immediate wake of a crack tip by strain concentration or fretting contact between the crack faces, respectively;
- Dissolution of the exposed surface;
- Nucleation and growth of oxide on bared surface.

Hydrogen embrittlement in aqueous media involves:

- Diffusion of water molecules or hydrogen ions between the crack walls toward the crack tip;
- Reduction of these species to create absorbed hydrogen atoms at the crack tip surface;
- Surface diffusion of absorbed atoms to preferential surface locations;
- Absorption of the atoms to a critical location (e.g. a grain boundary or a void).

It is shown from the crack tip strain measurements that deformation fields ahead of a fatigue crack are strongly affected by the presence of an aggressive environment [3].

Creep-fatigue considers temperature effects on fatigue process, and could be divided in two different families:

- Fatigue at Low Temperature;
- Fatigue at High Temperature.

Considering a metallic material at sub-zero temperatures it should be observed that yield strength, S_y, increases, and its ductility and fracture toughness, K_c, decrease. The endurance limit, S_e (which is the amount of stress below which no fatigue failure will be expected), of the material will increase with a drop in temperature. Since ductility drops with decreasing temperature, the short life fatigue resistance also deteriorates with decreasing temperature.
At long lives, where the fatigue is controlled by strength, lower temperatures will be expected to promote a higher number of cycles to failure. In low-temperature fatigue there is a reduction of cyclic plasticity which provides significant variations in fatigue crack growth rates, from observed behavior at room temperature. At temperature close to 'homologous temperature'(which expresses the temperature of a material as a fraction of its melting point temperature using the Kelvin scale), the mechanisms responsible for fracture become time

dependent rather than cycle dependent. At very high temperatures and low test frequencies, the inelastic zone becomes dominant with respect to specimen dimensions. Furthermore, at elevated temperatures, flow strength decreasing of the material causes a greater increase of non-linear deformation to develop.

1.2 Fatigue Failure Evolution

Fatigue failure process can be divided into five stages:

- Cyclic Plastic Deformations Prior to Fatigue Cracks Initiation;
- Micro-Cracks Initiation;
- Micro-Cracks Propagation to Form Macro-Cracks;
- Macro-Cracks Propagation;
- Final failure.

These stages are influenced by a wide range of mechanical, microstructural and environmental factors [4].

Every stage can be described by several theoretical models and each model introduces different approximations with respect to the physics of fatigue phenomenon. In detail, the initial cyclic plastic deformations which give rise to micro-crack initiation are widely described with the theory of elasto-plasticity and their location should be found with finite element analysis (Chapter 2). Micro-crack initiation and propagation to give evidence to macro-crack are the object of 'Continuum Damage Mechanics' (CDM) (Chapter 2). Macro-crack propagation is described by 'Fracture Mechanics' (Chapter 3).

In this section fatigue is presented from a physical point of view, in order to qualitatively describe the phenomenon dynamics.

1.2.1 Cyclic Plastic Deformation Prior to Fatigue Crack Initiation

Notches, inclusions and flows are present as consequence of material processing, chemical precipitation or other events which emphasize micro-structural discontinuity (comparable with crystallographic material structure). Such defects will concentrate the stresses due to a localized lost of stiffness of material. Induced micro-plasticity may provide to material dechoesion and if sufficient high alternating or monotonous plastic strain is induced, small micro-cracks can initiate. Alternately, if an ideal material (with elastic behavior and no initial defects) is considered in a 'fully reverse load' cycle on the same slip plane conditions (e.g., constant amplitude,proportional loading), this step is canceled in consequence of crack closure induced by compression; however, in the practice, slip occurs on many different planes, and material could be assumed as non perfect. Slip step accumulation in a local region may culminate in an increasing of surface's roughening, consequently, resistance to fatigue failure is greater for such materials that are not subject to intensive localization of plastic deformations. Events called 'extrusions' and 'intrusions' will form consequently from plastic strain on the surface as described by Cottrell's and Hull's model (Fig.1.3) [5]. This model supposes that sequential slip on two intersecting slip planes occurs. In the first half-cycle, first one slip system and then the other are imagined to operate, producing indentation. Alternately, a protrusion would form if the dislocations have Burgers vectors (often denoted by 'b', it is a vector that represents the magnitude and direction of the lattice distortion due to dislocation in a crystal lattice [6]) of opposite sign.
During the second half-cycle, the first slip system and then the second are imagined to operate again, giving rise to an intrusion and extrusion pair.

Laird and Duquette [7] clarified that intrusion-extrusion pairs appears when there is only one operative slip system, but it is not clear whether intrusions and extrusions are always paired [8].

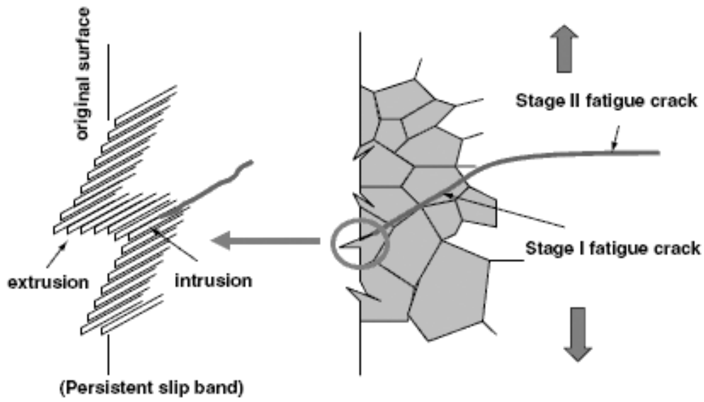

Figure 1.3: Cottrell-Hull model describing formation of intrusions and extrusion. Operation of two interesting slip system is assumed to occur in the sequence shown. Fatigue Testing And Analysis - Theory And Practice; Yung-Li Lee, Jwo Pan, Richard B. Hathaway, Mark E. Barkey; Elsevier.

Neumann [9] postulated that an intrusion or extrusion may form by a dislocation avalanche along parallel neighboring slip planes containing dislocation accumulation of opposite sign.
The term 'persistent slip band' was introduced by Thompson et al. [10]. They examined polished surfaces of copper and nickel after various amounts of cyclic deformations and observed many slip bands. Although most were removed easily by electro-polishing, some required extensive electro-polishing for removal; when the samples were retested, slip bands formed again in these places, consequently authors defined 'persistent' such slip bands. Hence, plastic deformation in slip bands produces regions of intense surface roughness, and this is quite general for all metals. Considerable slip bands or plastic strain localization occurs more probably as a result of cyclic deformation instead of monotonic deformation. Localized regions of surface roughness occur because certain regions are softer or have become softer than others.

1.2.2 Micro-Cracks Initiation

Micro-cracks initiation have been observed to occur in association to slip bands, in grain boundaries, in second-phase particles, and in inclusion or second-phase interfaces with the matrix phase as demon-

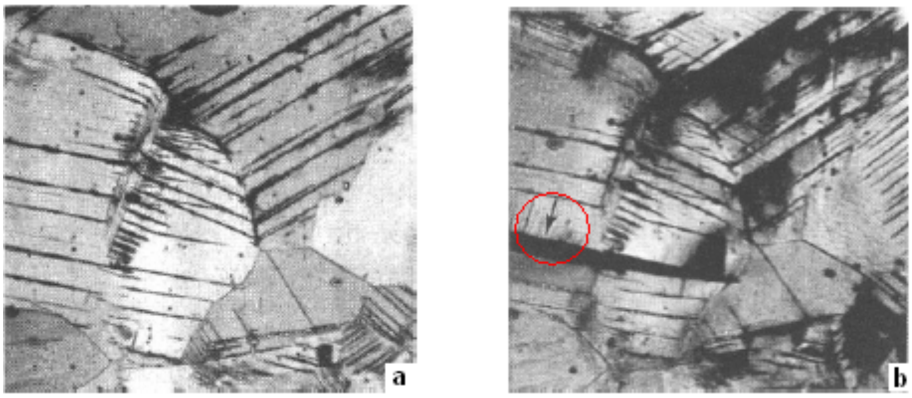

Figure 1.4: Development of cyclic slip bands and a micro-cracking in a pure copper specimen; in Fig.1.4a, slip line are clearly visible and in Fig.1.4b, we have a plastic strain of about 5% which open a micro-crack (see arrow). Fatigue of Structures and Materials; Jaap Schijve.

strated by several microscopic investigations (Fig. 1.4) [11]. Slip is discontinuous across grain boundaries, and many slip systems must be active to keep the grains from pulling apart. Therefore, grain boundaries are often responsible to fatigue crack initiation. Dynamics of fatigue crack initiation develops as follow: during cyclic plastic deformation, dislocations either emerge at the surface of the metal or accumulate against obstacles. If the dislocations continuously emerge at the surface rather than accumulate against obstacles, then slip bands (potentially becoming cracks) appear in the central portions of the grains, where the flow stress is lower. Resistance to slip-band initiation in the central portion of a grain decreases with increasing grain size, following the Hall-Petch relation [12] [13].
Many types of obstacles can cause dislocation accumulation during cycling, including grain boundaries, inclusions, oxide films, and domain boundaries. Dislocation accumulation result in elastic strain energy increasing (e.g. potential energy that is stored when a body is deformed in the elastic region). When this energy density exceeds twice the surface free energy(which derives from the unsatisfied bonding potential of molecules at a surface, giving rise to 'free energy'), a condition of instability occurs that energetically enable the initiation of micro-cracks. This can lead to a slip-band crack in the matrix, de-cohesion

along a grain boundary, or cracking of a second-phase particle that may lie in the matrix or grain boundary. From a potential strain energy point of view, the intrusion is related to cyclic slip in a slip band [14]. If the grain-boundary regions in a precipitation-hardened alloy are free of precipitates, then plastic flow at low plastic strains may be concentrated in these regions and initiate fatigue cracks. Even if an isolated second-phase particle cracks, it must spread into the matrix to initiate fatigue crack. Thus, not all cracked inclusions leas fatigue cracks.
In conclusion fatigue micro-crack initiation is a material surface phenomenon.

1.2.3 Micro-Cracks Propagation to Form Macro-Cracks

In anisotropic elastic material with a crystalline structure and a number of different slip system, it is possible to talk about micro-crack as long the size of the micro-crack is still in the order of a single grain. On a micro level, an inhomogeneous stress distribution is observed due to material micro-defects or micro-plastic concentration. So, more than one slip system may be activated. Moreover, if the crack is growing into the material in some adjacent grains, the constraint on slip displacements will increase due to the presence of the neighboring grains.
Micro-crack growth direction will be initially inclined of about 45° from the applied load direction and when the crack dimensions reaches a macroscopic value it grows perpendicular to the loading direction (Fig.1.5).
As previously discussed, micro-crack growth depends on cyclic plasticity and barriers to slip should determinate a threshold for crack growth. The crack growth rate measured as the crack length increment per cycle decreases when the crack tip approaches the first grain boundary. After penetrating through the grain boundary the crack growth rate increases during growth into the next grain, but it decreases again when approaching the second grain boundary. After

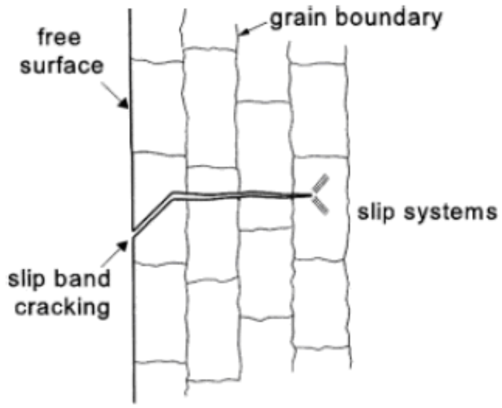

Figure 1.5: Cross section of micro-crack.

that the micro-crack continues to grow with a steadily increasing rate (Fig.1.6) [15].

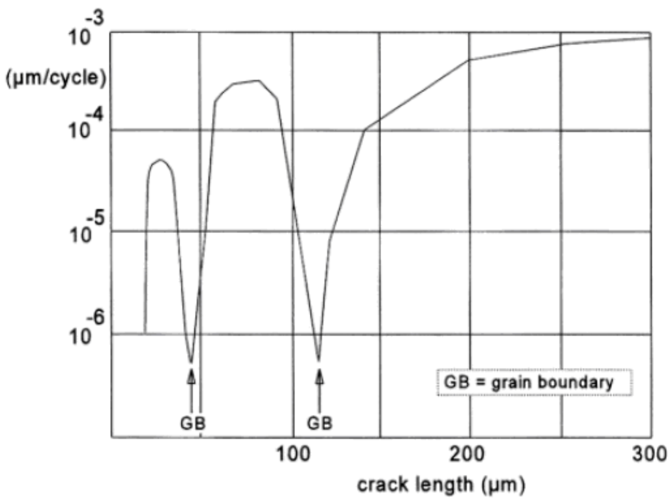

Figure 1.6: Grain boundary effect on crack growth in an Al-alloy.

1.2.4 Macro-Cracks Propagation

While crack initiation is a surface phenomenon (due to plasticity accumulation and with no material initial defects assumption), crack growth depends on the material as a bulk property, when crack penetrates into the material. During loading the crack will be opened by crack tip plastic deformations, which are supposed to occur on

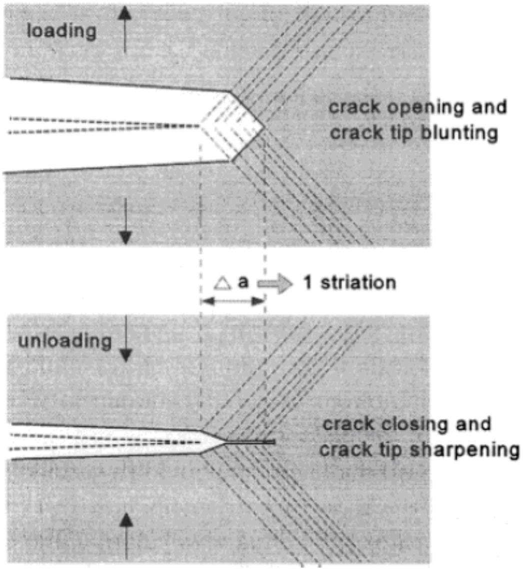

Figure 1.7: Crack extension in a single load cycle.

two symmetric slip systems (Fig.1.7). The slip zones are indeed the zones with the maximum shear stress, both during loading and unloading. Crack propagation is consequence of stress concentration near the crack tip zone, which is described by the 'stress intensity factor', K :

$$\mathbf{K} = \mathbf{S} \cdot \sqrt{\mathbf{a} \cdot \mathbf{f(g)}} \tag{1.2}$$

where:

- S: applied stress;
- a: crack length;
- $f(g)$: function of specimen geometry, loading conditions and the ratio of crack length to specimen with,$(\frac{a}{w})$.

Formulas for $f(g)$ have been derived for a wide variety of conditions and tabulated in a number of books.
With reference to cyclic loading we could give the definition of stress intensity factor range:

$$\mathbf{\Delta K} = \mathbf{\Delta S} \cdot \sqrt{\mathbf{a} \cdot \mathbf{f(g)}} \tag{1.3}$$

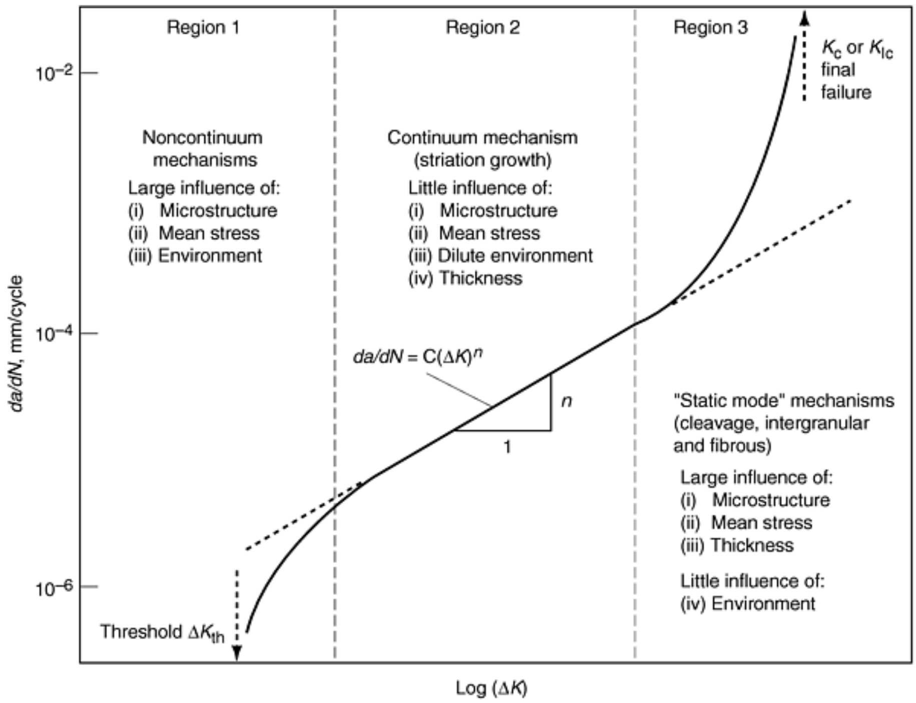

Figure 1.8: Schematic plot of fatigue crack propagation rate , on a log-log scale.

Fatigue crack propagation rate are typically plotted on a ΔK versus da/dN graphs in a log. scale, which allows to linearize the obtained results, Fig.1.8. With reference to this figure, fatigue crack growth behavior is characterized by three regimes:

- **Region I:** threshold and near threshold region, where da/dN decreases rapidly decreasing ΔK to a threshold value (ΔK_0 or ΔK_{TH});
- **Region II:** mid-region characterized by the Paris relation [16]:

$$\mathbf{\frac{da}{dN} = c \cdot (\Delta K)^n} \tag{1.4}$$

  where c, n are material constants.

- **Region III:** high rate region, where the maximum stress intensity factors value, K_{max}, approaches the critical stress intensity factors value for static failure, K_c. K_{max} is the maximum stress intensity factor produce during fatigue life.

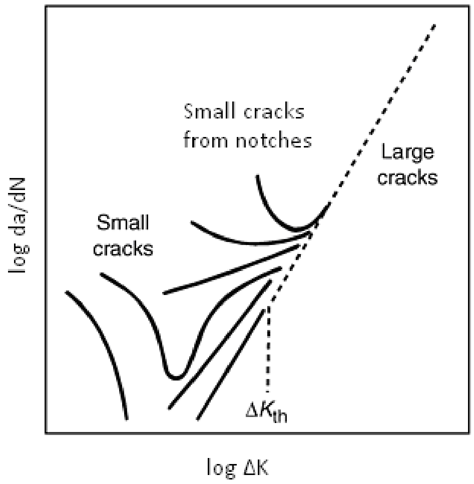

Figure 1.9: Schematic representation of the typical fatigue crack growth behavior of long and short cracks at constant values of imposed cyclic range and load ratio.

A fatigue life calculation could be obtained from the Paris law by integrating Eq.1.4 from an assumed initial size a_0, to a critical size a_f. From substitution of Eq.1.3 in Eq.1.4 we derive [17]:

$$\mathbf{N_f} = \frac{\mathbf{2}}{\mathbf{c \cdot (n-2) \cdot f(g)^n \Delta s^n} \cdot \pi^{\frac{\mathbf{n}}{\mathbf{2}}}} \cdot \left(\mathbf{a_0^{1-\frac{n}{2}} - a_f^{1-\frac{n}{2}}}\right) \tag{1.5}$$

The stress needed for fatigue crack growth will decrease during the cycle and the final consequence of a cyclic loading is the structural failure.

1.3 Small Fatigue Cracks

As previously discussed, small cracks domain develop until their dimensions are comparable with grain size, after that we enter in the large cracks domain. It has been shown that the growth rates of small crack can be significantly greater than the corresponding rates of long cracks with respect to the same applied nominal force (Fig.1.9). There are different size scales below which the growth rates of a fatigue crack may exhibit crack size dependence.
Suresh and Ritchie suggest this classification for small cracks [33]:

- Micro-structurally small cracks;

- Mechanically small cracks;
- Chemically small cracks.

The expression 'small cracks' and 'short cracks' are frequently used interchangeably, even if a distinction is made between the two cases in that the former definition (small cracks) is employed for flaws which are small in all three dimensions and the latter type (short cracks) are taken to denote through-thickness flaws which are small in one dimension [34].

1.3.1 Micro-Structurally Small Cracks

A crack is generally considered 'micro-structurally small', when all crack dimensions are small in comparison to characteristic micro-structural dimensions. The relevant micro-structural feature that defines this scaling change from material to material, but the most common accepted micro-structural scale is the grain size. Only if the small crack and its crack-tip plastic zone results completely embedded within a single grain or a few grain diameters it is possible to label it as a 'micro-structurally small' one [35]. As a small crack approaches a grain boundary, the fatigue crack growth may accelerate, decelerate, or even arrest, depending on slip propagation into the contiguous grain. The transmission of slip across a grain boundary depends on the grain orientation, the activities of secondary and cross slip, and the planarity of slip. The transition of the small crack from one grain to another may require a change in the crack path, which should also influence crack closure (1.4). The resulting crack growth behavior is therefore very sensitive to the crystallographic orientation and to the properties of individual grains located within the cyclic plastic zone. The branch of mechanics which studies micro-structurally small cracks is called 'Micro-structural Fracture Mechanics (MFM)' and would explain crack propagation at the micro-crack level [36]. The MFM approach was first introduced by Hobson et al. [37] and later by Navarro and de los Rios [38]. The micro-structurally small crack growth law is expressed by:

$$\frac{\mathbf{da}}{\mathbf{dN}} = \mathbf{c}\delta\gamma^{\beta}\left(\mathbf{d} - \mathbf{a}\right) \tag{1.6}$$

where d denotes a micro-structural dimension. It should be noted that (Eq.1.6) indicates a zero crack speed when the crack depth, a, is equal to d, and that prior to this state the crack will continuously decelerate until it either stops or continues to propagate according to an overlapping continuum mechanics description.

1.3.2 Mechanically Small Cracks

A crack is generally considered to be 'mechanically small' when all crack dimensions are small compared to characteristic mechanical dimensions. The relevant mechanical feature is typically a zone of plastic deformation, such as the crack-tip plastic zone or a region of plasticity at some mechanical discontinuity (e.g., a notch). In this family of cracks, the crack is fully embedded in the plastic zone, or the plastic zone is a large fraction of the crack size (Fig.1.10).

Many micro-structurally small cracks are also mechanically small

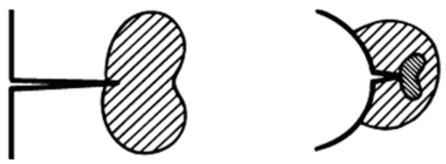

Figure 1.10: Schematic of relationship between mechanically small cracks and plastic zones.

and in this situation, mechanical behavior is the dominant. The crack front of a short crack involves many different grains and hence is not subject to strong micro-structural effects.

Typical crack growth data for mechanically small cracks in unnotched configurations are shown in Fig.1.11 for a high-strength, low-alloy (HSLA) steel [39]. The slope of the Paris equation often appears to be roughly the same for both small and large crack data, but the small-crack data sometimes fall above the large-crack trend line when expressed in terms of nominal ΔK. The primary motivation for mechanical small cracks behavior appears to be that local stresses are

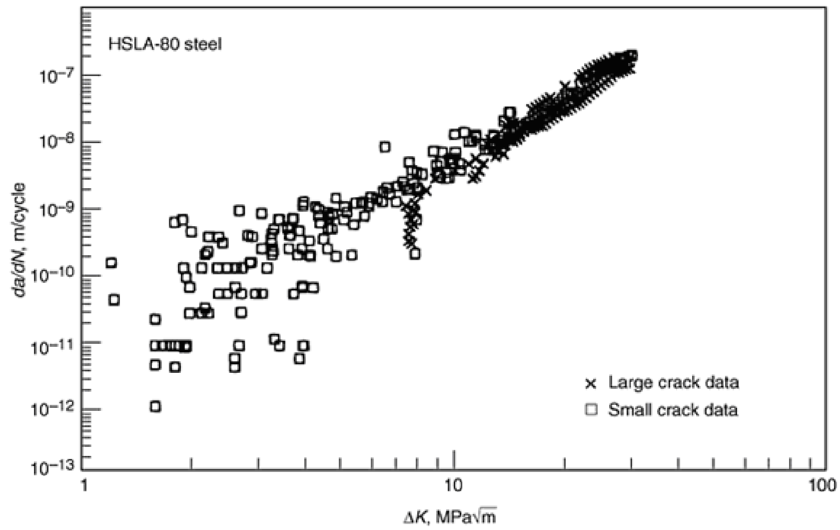

Figure 1.11: Typical fatigue crack growth data for mechanically small cracks and large cracks. ASM Metals Hand-Book Volume 19 - Fatigue And Fracture.

significantly larger than those encountered under typical small-scale yielding (SSY) conditions, especially at near-threshold values of ΔK. These local stresses may have been elevated by the presence of a stress concentration, or they may simply be large nominal stresses in uniform geometries. These large local stresses significantly enhance crack-tip plasticity, which in turn enhances the crack driving force, either directly through violations of K-dominance, or indirectly through changes in plasticity-induced crack closure, or both. The appropriate analytical approach of the mechanically small crack, then, primarily involves appropriate investigation of the elastic-plastic crack driving force and crack closure. The nominal elastic formulation of ΔK gradually becomes less accurate as a measure of the crack driving force as the applied stresses become a larger fraction of the yield stress. Under intermediate-scale yielding, (ISY), when S_{max}/S_{ys} exceeds about 0.7, a first-order plastic correction to ΔK may be useful [40]. This correction may be based on the complete Dugdale [41] formulation for the J-integral (presented in chapter 3), expressed in terms of K, or it may be based on an effective crack size, defined as the sum of the actual crack size and the plastic zone radius. However, in most cases this first-order correction will change the magnitude of ΔK by no more than 10 to 20 %. In the large-scale yielding (LSY) regime, when the nominal plastic strain range becomes non-negligible, it will generally be necessary to replace ΔK entirely with some alternative elastic-plastic fracture mechanics parameter [42], such as a complete ΔJ formulation.

1.3.3 Chemically Small Cracks

Experiments on a variety of ferritic and martensitic steels in aqueous chloride environments have shown that under corrosion-fatigue conditions, small cracks can grow significantly faster than large cracks at comparable ΔK values [43]. This phenomenon result from the influence of crack size on the occluded chemistry that develops at the tip of fatigue cracks. The specific mechanism responsible for this 'chemical crack size effect' is the enhanced production of embrittling hydrogen within small cracks, resulting from a crack size dependence of one or more factors that control the evolution of the crack-tip environment: convective mixing, ionic diffusion, or surface electrochemical reactions [44]. This mechanism is distinctly different from that responsible for the enhanced rate of crack growth in micro-structurally or mechanically small fatigue cracks. However, the enhanced crack-tip plasticity associated with micro-structurally or mechanically small cracks could further stimulate the electrochemical reactions through the creation of additional fresh and highly reactive surfaces at the crack tip. The chemical crack size effect is illustrated by the data of Gangloff [43] for 4130 steel in an aqueous environment (Fig.1.12). Note that corrosion-fatigue crack growth rates from small surface cracks, as well as short through-thickness edge cracks, are appreciably faster than corrosion-fatigue crack growth rates from large through-thickness cracks in standard compact tension specimens. It is also interesting to note that the corrosion-fatigue crack growth rates for small surface cracks decrease with increasing applied stress (at a given ΔK). This trend is opposite to the dependence of applied stress on crack

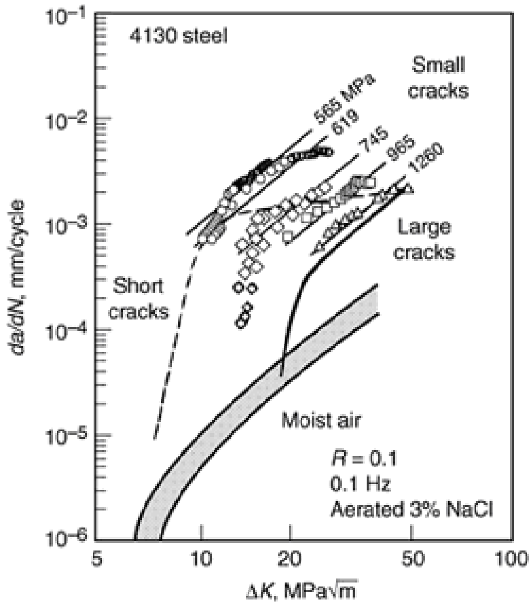

Figure 1.12: Typical corrosion-fatigue crack growth data for chemically small cracks and large cracks. Fracture and Fatigue; Anderson (2Nd Ed.).

growth rates in mechanically small fatigue cracks. Moreover, growth rate of CF crack are enhanced compared to those in a moist laboratory air environment, even though the latter were generated with both small and large cracks. Thus, in relation to the fatigue small-crack effect, the chemical small-crack effect is of potentially greater importance, because it can occur over a much larger range of crack sizes. Not all materials exhibit a chemically small crack effect, and the complexity of the important electrochemical mechanisms makes it difficult, if not impossible, to predict a priori the existence or quantitative extent of this effect in a given application. Changes in alloy and solution chemistry, electrode potential, oxygen concentration, applied stress and stress ratio, and the specific rate-controlling process in the electrochemical reaction, can all influence crack growth rates. In general, experimental data for specific material-geometry-load-chemistry combinations are needed to characterize chemically small crack effects.

1.4 Fatigue Cracks Closure

Crack closure is the premature closure of a crack induced by the presence of an obstacle within it such as plastic deformation, facets, oxide or metal particles (Fig.1.13) [45]. The most salient event in the last decade has been the questioning of the significance and even the existence of crack closure [46]. Crack closure phenomenon was

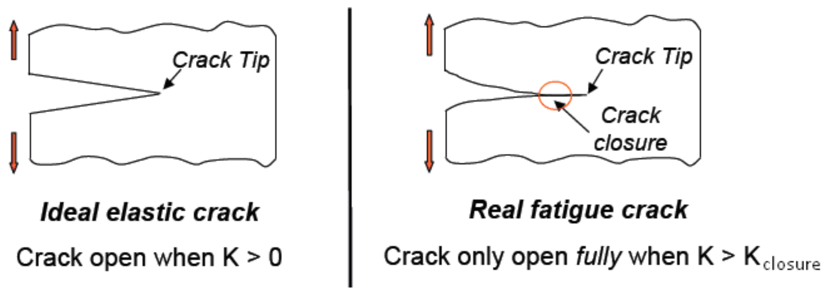

Figure 1.13: Mechanism of crack closure.

first studied by Christensen [47], who matched photo-elastic models to fatigue experiments in which fretting-generated accumulated debris, limit the opening displacement range of cracks. The propagation rates were strongly affected by whether or not the debris was free to get out of the crack. A decade later, crack closure was reintroduced and formalized by Elber [48] [49]. Elber shows that plastically-deformed cracks make contact with itself while some tensile loading was still applied. Some other causes of crack closure have been mentioned and several may be enumerated [50] [47] [51]:

- Plastic deformation of the wake;
- Roughness and disregistry;
- Oxidation or corrosion products;
- Viscous liquids;
- Martensitic transformations;
- Metal particles from fretting;

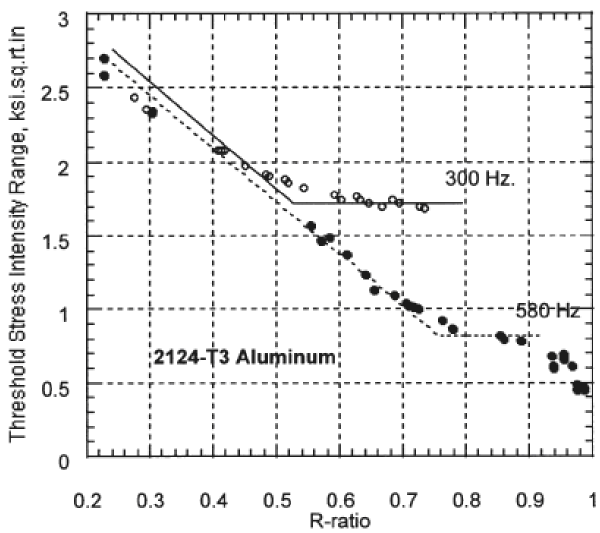

Figure 1.14: Threshold stress intensity versus stress ratio for 2124-Al at two different test frequencies adapted from Schmidt and Paris. Negative-slope lines represent constant peak stress intensity. Horizontal lines represent constant stress intensity range. The effect of frequency is probably due to heating of the crack tip. ASM Metals Hand-Book Volume 19 - Fatigue And Fracture.

- Hydrogen induced deformation.

Later, Schmidt and Paris [52] plotted the threshold stress intensity of $2124 - T3$ aluminum vs. R (Fig.1.14). By overprinting lines corresponding to a constant K_{max} and a constant ΔK on their diagram they were able to show that the sloping portion of the curve is related to a constant K_{max}, while the flat portion of the curve is related to a constant ΔK. It allows to argue that the part of the curve controlled by K_{max} was governed by the 'need to open the crack' while the constant ΔK portion represented the true threshold hidden under closure. This follows from the relation:

$$\mathbf{K_{max}} \geq \mathbf{\Delta K_{TH,int}} + \mathbf{K_{closure}} \tag{1.7}$$

where $\Delta K_{TH,int}$ is an intrinsic threshold stress intensity. This relation must be satisfied in order to allow the closure condition and the intrinsic threshold simultaneously. Application of this relation to explain Fig.1.14 carries the tacit assumption that $K_{closure}$, a suitably chosen effective stress intensity at which the crack opens, does not vary with

R. On the basis of several researches [53] [54] [55] the various forms of fatigue crack closure are categorized in consequence of mechanical, micro-structural and environmental factors:

- Plasticity-induced crack closure;
- Oxide-induced crack closure;
- Roughness-induced crack closure;
- Viscous-fluid induced crack closure;
- Phase-transformation induced crack closure.

Fatigue crack closure is a very complex phenomenon that has not yet found a complete description. For our purposes it will no more delved in this work.

1.5 'Safe-Life' and 'Fail-Life' Concept

Now that fatigue process has been presented, the main approaches for fatigue life design will be discussed. Fatigue design provides two different philosophies for fatigue life prediction [17] [67]:

- In the safe-life approach, the typical cyclic load spectra, which are imposed on a structural component in service, are first determined. On the basis of this information, the components are analyzed or tested in laboratory under load conditions which are typical of service spectra, and a useful fatigue life is estimated for the component. The estimated fatigue life is corrected by a factor of safety and become a prediction of 'safe life' for the component. After that life the component must be changed independently of his conditions.
- The fail-life concept is based on the argument that, even if an individual member of a large structure fails, there could be sufficiently structural integrity in the remaining parts to enable the

structure to operate safely until the crack is detected. This approach mandates periodic inspection along with the requirement that the crack detection techniques be capable of identifying flaws to enable specimen repairs or replacements.

1.6 Experimental Procedures

In the preceding section we described fatigue life evolution as a micro-mechanical process and consequently we would like to characterize total fatigue life as a function of variables such as the applied stress-range, strain-range, mean stress and environment by introducing the two different experimental procedures which are usually implemented to underline fatigue material behavior. It will be introduced the 'stress-life' and the 'strain-life' approaches. Both of these experimental methodologies embodies the phenomenon evolution as we previously described by defining the total life as the total number of cycles or time to induce fatigue damage and to initiate a dominant fatigue flaw which is propagated to final failure.

1.6.1 Stress-Life Approach

Stress-Life Approach is the first method used to characterize fatigue life. This approach was first introduced in the 1860s by Wohler who developed the concept of endurance limit defined as the applied stress amplitude below which a material is expected to have ideally an infinite fatigue life [18]. The experimental procedure provides to determinate that limit, S_e (the lowest value under which no fatigue failure is possible) and consists in a test where specimens are typically machined to obtain a cylindrical gage length section which is fatigue tested in plane bending, rotation banding, mono-axial compression-tension or mono-axial tension-tension cycling loading [19], in condition of zero mean stress, S_m. The stress amplitude, S_a, for fully reversed loading is plotted against the number of fatigue cycles to failure, N_f, (Fig.1.15). This approach is still widely used in application were low-amplitude cyclic stresses induce primarily elastic deformation in a component

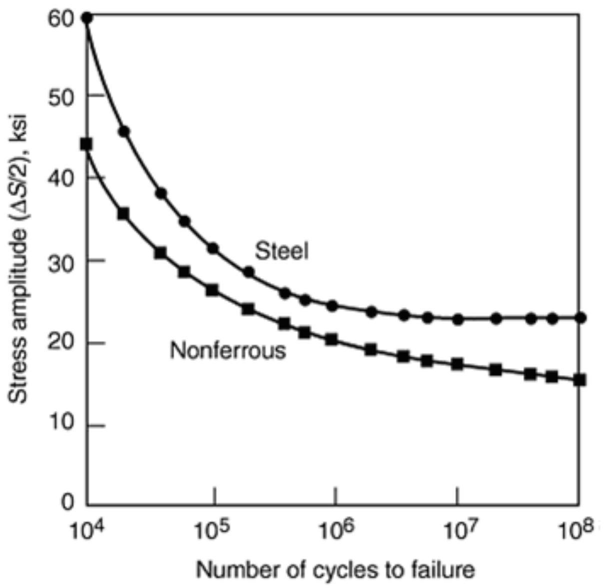

Figure 1.15: Schematic S-N representation of materials having fatigue limit behavior (asymptotically leveling off) and those displaying a fatigue strength response (continuously decreasing characteristics).

which is designed for long life (i.e. HCF applications). The intercept of the stress-life curve with the ordinate coincides to tensile strength, S_{TS}, at one quarter of the first fatigue cycle. The S_e value, is 35% to 50% of tensile strength, for most steels and alloys. Lot of high strength steel and alloys do not exhibit a fatigue limit and S_a continues to decrease with increasing number of cycles. If Fig.1.15 will be drown on a log-log scale, with the true stress amplitude plotted as a function of the number of cycles to failure, a linear relation is observed. The resulting expression relating the stress amplitude in a fully reversed, constant-amplitude fatigue test to the number of loads reversals to failure, $2N_f$, is the so called Basquin relation (Fig.1.16) [20]:

$$\frac{\mathbf{\Delta S}}{\mathbf{2}} = \mathbf{S_a} = \mathbf{S'_f} \cdot (\mathbf{2N_f})^{\mathbf{b}} \tag{1.8}$$

where S'_f is the fatigue strength coefficient (which is, to good approximation, equals the true fracture strength S_f and b is the fatigue strength exponent or Basquin exponent (for most metals is in the range of -0.05 to -0.12).

To perform a correct stress-life evaluation it must be introduced the

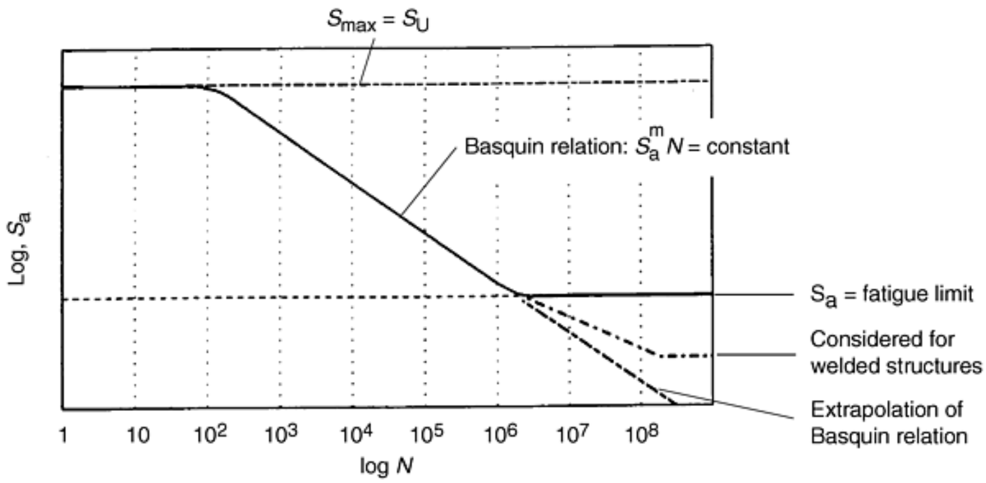

Figure 1.16: S-N curve on log-log scale with extrapolations below the fatigue limit. ASM Metals Hand-Book Volume 19 - Fatigue And Fracture.

mean-stress effect. As previously discussed, usually in fatigue test mean-stress is zero, but in the practice there are a few applications in that condition.
There are three models generally used to estimate mean-effect [21]:

- **Soderberg relation:**

$$\mathbf{S_a = S_a |_{S_m=0} \cdot \left(1 - \frac{S_m}{S'_f}\right) = 0} \tag{1.9}$$

- **Modified Goodman relation:**

$$\mathbf{S_a = S_a |_{S_m=0} \cdot \left(1 - \frac{S_m}{S_{TS}}\right) = 0} \tag{1.10}$$

- **Gerber relation:**

$$\mathbf{S_a = S_a |_{S_m=0} \cdot \left(1 - \left(\frac{S_m}{S_{TS}}\right)^2\right) = 0} \tag{1.11}$$

where S_Y and S_{TS} are respectively the yield strength and the tensile strength.
These relations could be represented in terms of constants-life diagrams Fig.1.17.
It is useful to underline that:

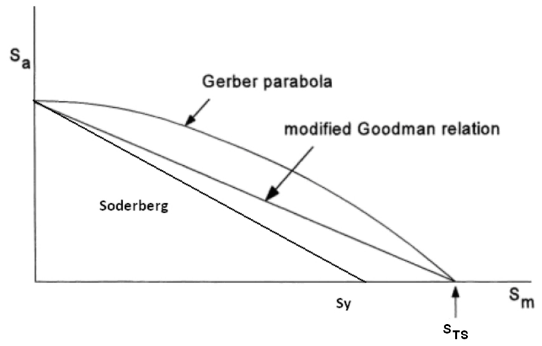

Figure 1.17: Approximation for constant-N lines in a fatigue diagram.

- Eq.1.9 provides a conservative estimate of fatigue life for most engineering alloys.
- Eq.1.10 matches experimental observations quite closely for brittle metals, but is conservative for ductile alloys. For compressive mean stress is usually non-conservative.
- Eq.1.11 is good for ductile alloys for tensile mean stresses.

The constant life diagram evaluated for different mean stress levels, is commonly named 'Haigh diagram' (Fig.1.18). In this figure, the maximum and the minimum stresses of fatigue cycle, both normalized by the tensile strength, are plotted. Moreover, while the Basquin relation (Eq.1.8) is valid only for zero mean stress conditions, Morrow [22](1968) has presented a modification of the mentioned relation which accounts for mean stress effect:

$$\mathbf{S_a} = \left(\mathbf{S_f'} - \mathbf{S_m}\right) \cdot (\mathbf{2N_f})^{\mathbf{b}} \tag{1.12}$$

Eq.1.12 allows us to evaluate the number of cycles to fatigue failure by the following relation:

$$\mathbf{N_f} = \left(\mathbf{1} - \frac{\mathbf{S_m}}{\mathbf{S_f'}}\right)^{\frac{1}{b}} \cdot \mathbf{N_f} \mid_{\mathbf{S_{m=0}}} = \mathbf{0} \tag{1.13}$$

where $N_f \mid_{S_{m=0}}$ is the number of cycles to failure for zero mean stress.

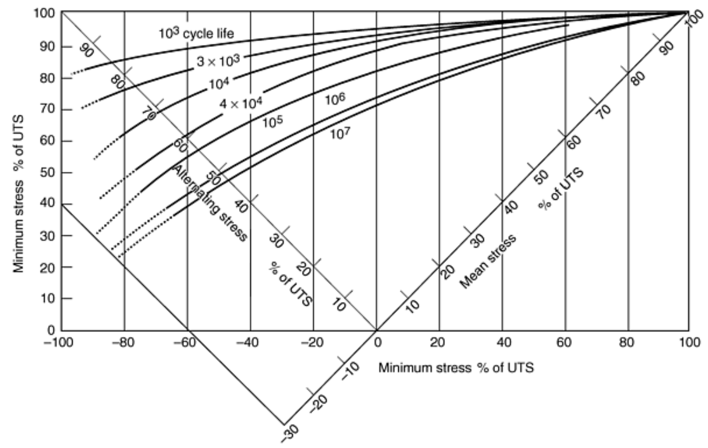

Figure 1.18: Schematic representation of the Haigh diagram showing constant life curves for different mean stress levels in terms of the maximum and the minimum stresses of the fatigue cycle. ASM Metals Hand-Book Volume 19 - Fatigue And Fracture.

1.6.2 Strain-Life Approach

Engineering components, in practical applications, generally undergo a certain degree of structural constraint and localized plastic flow, particularly at locations of stress concentration. In these situations, it is more appropriate to consider the strain life approach to fatigue. The first work proposed on the strain-life approach was developed independently by Coffin and Manson in 1954 as a result of a characterization of fatigue life based on the plastic strain amplitude. Strain-life approach is primarily intended to address the 'low-cycle fatigue' area (e.g., from approximately 10^2 to 10^6 cycles). The use of a consistent quantity like strain, gives considerable advantages both in 'high-cycle' and 'low-cycle' fatigue [23]. The representations of strain-life data are similar to those for stress-life data. Rather than $S-N$, there are in this approach $\varepsilon - N$ plots, where a log-log format is still most common. The curve represents a series of points, each associated with an individual test failure point. The principal value referred to vertical axis gives evidence of total strain amplitude, but it is also possible to find total strain range, plastic strain range, or other determined strain measures. In $\varepsilon - N$ tests the strain can be monitored either axially or diametrically [19]. For data generation to support the

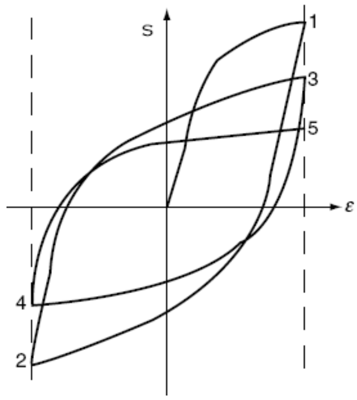

Figure 1.19: Stress-strain hysteresis in a constant-amplitude strain-controlled fatigue test.

$\varepsilon - N$ method, there are standards by which testing is conducted [24]. Strain-life test acquisition data is not as straightforward as the load-controlled S-N test. Monitoring and controlling strain data requires continuous extensometer capability. The combined output of the extensometer and load cell provides the displacement-load trace from which is formed the so called 'hysteresis loop' (Fig.1.19). A stabilized loop of this type is formed during every constant-amplitude test and should be recorded as part of test procedures. Modeling of the $\varepsilon - N$ curve currently employs the separated elastic and plastic strain contributions and the total strain amplitude, $\frac{\Delta\varepsilon}{2}$, extrapolated from experimental data, is considered as follows:

$$\frac{\boldsymbol{\Delta}\varepsilon}{\mathbf{2}} = \frac{\boldsymbol{\Delta}\varepsilon_{\mathbf{E}}}{\mathbf{2}} + \frac{\boldsymbol{\Delta}\varepsilon_{\mathbf{P}}}{\mathbf{2}} = \left(\frac{\mathbf{S}'_{\mathbf{F}}}{\mathbf{E}}\right) \cdot (\mathbf{2N_f})^{\mathbf{b}} + \varepsilon'_{\mathbf{f}} \cdot (\mathbf{2N_f})^{\mathbf{c}} \tag{1.14}$$

where:

- $\frac{\Delta\varepsilon}{2}$: total strain amplitude;
- $\frac{\Delta\varepsilon_E}{2}$: elastic strain amplitude;
- $\frac{\Delta\varepsilon_P}{2}$: plastic strain amplitude;
- S'_f: fatigue strength coefficient;
- b: fatigue strength exponent;

- ε'_f: fatigue ductility coefficient;
- c: fatigue ductility exponent;
- $2N_f$: number of reversals to failure (2 reversals = 1 cycle).

As $S - N$ methods, also for strain-life approach there must be a correction for treating mean stresses [25]. This correction has been introduced by Morrow in term of (Eq.1.14):

$$\frac{\mathbf{\Delta}\varepsilon}{\mathbf{2}} = \frac{\mathbf{\Delta}\varepsilon_{\mathbf{E}}}{\mathbf{2}} + \frac{\mathbf{\Delta}\varepsilon_{\mathbf{P}}}{\mathbf{2}} = \left(\frac{\mathbf{S'_F} - \mathbf{S_0}}{\mathbf{E}}\right) \cdot (\mathbf{2N_f})^{\mathbf{b}} + \varepsilon'_{\mathbf{f}} \cdot (\mathbf{2N_f})^{\mathbf{c}} \tag{1.15}$$

where, S_0 is the mean stress as determined from the hysteresis loop developed at the detail, not the mean elastic stress. In practice, the application would require the estimation of the strain amplitude and resulting mean stress, then an iterative solution for the number of reversals to failure, $2Nf$.

1.7 References

ASM Metals Hand-Book Volume 19 - Fatigue And Fracture.

Fracture and Fatigue; Fracture Mechanics; Anderson (2Nd Ed).

Fatigue of Structures and Materials; Jaap Schijve.

Fatigue of Materials; S. Suresh.

Fracture and Fatigue Control in Structures (2Nd Ed); John M. Barsom, Stanlet T. Rolfe.

Fatigue Testing And Analysis - Theory And Practice; Yung-Li Lee, Jwo Pan, Richard B. Hathaway, Mark E. Barkey; Elsevier.

Chapter 2

Continuum Damage Mechanics

Fatigue has been described mainly from a qualitative point of view in the first chapter. The goal of this chapter is to investigate crack initiation dynamics presenting a mathematical model in order to determinate the number of cycles for mesocrack initiation, its initial size and its initial orientation. As previously introduced (Chapter 1), fatigue evolution embodies different specific branches of mechanics of material, to ensure coherence with the physics of the phenomenon. To obtain a specific fatigue crack initiation analysis, the most effective procedure is presented by 'Continuum Damage Mechanics'(CDM), allowing to evaluate the number of cycle for mesocrack initiation, also referred as nucleation, the macroscopic initial size and the crack orientation. For the purpose of this work, the so called 'Theory of Damage' will be presented in its simplest formulation.

2.1 Introduction to CDM

The term Continuum Damage Mechanics was first introduced by J.Hult in 1972 and this branch of Mechanics is based on the concept of 'damage' like a scalar variable as stated by L.M Kachanov in 1958. In this contest, damage is the creation and growth of microvoids or

microcracks which are discontinuities in a medium considered as continuous at a larger scale. Continuum media mechanics is based on the 'Representative Volume Element' concept, (RVE) supposing that all properties could be represented by homogenized variables. The damage discontinuities should be considered small if compared with the size of the RVE but they are effectively big with respect to atomic spacing in material matrix.
Damage is an irreversible phenomenon, and from a physical point of view it is related to irreversible plastic strains and more generally to a strain dissipation either on the so called 'mesoscale' (i.e. the scale of the RVE) or on the microscale (i.e. the scale of the discontinuities). This distinction embodies the adherence with the previously introduced LCF and HCF, and consequently:

- **LCF:** the strain fields are near yielding value, the damage introduced by cyclic loadings may act on the mesoscopic level by inducing mesoplasticity.

- **HCF:** the strain are in the elastic field, the damage may give rise to localized microplasticity and a several number of cycles is required to introduce micro-decohesion.

As a consequence of this qualitative interpretation of the physics of phenomenon, it is possible to formalize the definition of damage assuming that microcavities and microcracks may exist, the damage variable is physically defined by the surface density of microcracks and intersections of microvoids lying on a plane with normal $\vec{n}$ cutting the RVE of cross section δS (Fig.2.1). For the plane with normal $\vec{n}$ where this density is maximum, one has:

$$\mathbf{D_{\tilde{n}}} = \frac{\delta \mathbf{S_D}}{\delta \mathbf{S}} \tag{2.1}$$

Then a first approximation can be considering the damage as an 'isotropic phenomenon', so that it does not depend on the normal $\vec{n}$. This approximation is helpful in one-dimensional problems or in three-dimensional problems subjected to proportional loadings.

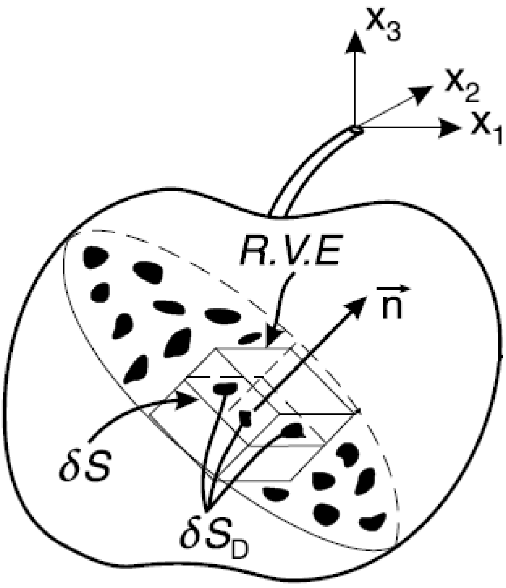

Figure 2.1: Damage on the R.V.E. plane.

The idea of damage directly introduces the 'Effective Stress Concept' which is the basis of the damage law formulation. While the damage grows up, the resisting area subjected to initial loading condition reduces, and the related stress will locally increase. The effective resisting area, $\delta\tilde{S}$ is given by:

$$\delta\tilde{\mathbf{S}} = \delta\mathbf{S} - \delta\mathbf{S_D} \tag{2.2}$$

where S is the damage-free area and S_D the damaged area. If no load variation is assumed, the following relation, for uniaxial case, could be written as (Y.N. Rabotnov 1968):

$$\tilde{\sigma}\delta\tilde{\mathbf{S}} = \sigma\delta\mathbf{S} \tag{2.3}$$

$$\mathbf{D} = \frac{\delta\mathbf{S_D}}{\delta\mathbf{S}} = \frac{\delta\mathbf{S} - \delta\tilde{\mathbf{S}}}{\delta\mathbf{S}} \tag{2.4}$$

which allows to evaluate the effective stress by:

$$\tilde{\sigma} = \frac{\sigma}{\mathbf{1} - \mathbf{D}} \tag{2.5}$$

If multiaxial case of isotropic damage is considered, the effective stress needs tensorial representation:

$$\tilde{\sigma}_{\mathbf{ij}} = \frac{\sigma_{\mathbf{ij}}}{\mathbf{1} - \mathbf{D}} \tag{2.6}$$

Finally, before introducing the analytical formulation of damage, it is useful to highlight the material properties which will be modified by damage and which can be used to evaluate the damage evolution itself.

- Elasticity Modulus ;
- Yield Stress ;
- Hardness ;
- Ultrasonic Waves Velocity ;
- Density .

In the following, the evolution laws governing damage rate, based on the studies of J. Lemaitre, will be presented.

2.2 Thermodynamics of Damage

A standard procedure to define material model is given by thermodynamics of irreversible processes which develops in three main steps:

- Identify the state variables representing of the process;
- Identify a state potential, as a function of all the state variables, in order to deduce the state laws of the process;
- Identify a dissipation potential, from which the laws of evolution of the state variables associated with the dissipative mechanisms derive.

The equations obtained by this procedure should agree with the second principle of thermodynamics to ensure a physical congruence.

2.2.1 Identification of State Variables

The simplifications introduced by 'small deformation hypothesis', allows to represent total strain by superimposition of elastic (ε^e_{ij}) and

Mechanisms	Type	Observable Variables	Internal Variables	Associated Variables
Thermoelasticity	Tensor	ε_{ij}		σ_{ij}
Entropy	Scalar	T		s
Plasticity	Tensor		ε^p_{ij}	$-\sigma_{ij}$
Isotropic Hardening	Scalar		r	R
Kinematic Hardening	Tensor		α_{ij}	X_{ij}
Damage	Scalar(isotropic)		D	-Y

Table 2.1: State and associated variables. (J.Lemaitre 1978)

plastic (ε^p_{ij}) contribution:

$$\varepsilon_{\mathbf{ij}} = \varepsilon^{\mathbf{e}}_{\mathbf{ij}} + \varepsilon^{\mathbf{p}}_{\mathbf{ij}} \tag{2.7}$$

So, the observable and internal variables are chosen to identify the damage process in order to describe the consequence of physical mechanism of deformation and degradation (Tab. 2.1).

2.2.2 State Potential Definition

The state potential is a time dependent function which give a representation of the actual energetic configuration of any system as a function of all the state variables. The Helmholtz specific free energy (ψ) is a function of all the state variables, and is commonly used in thermodynamics:

$$\psi\left(\varepsilon^{\mathbf{e}}_{\mathbf{ij}}, \mathbf{D}, \mathbf{r}, \alpha_{\mathbf{ij}}, \mathbf{T}\right) \tag{2.8}$$

The state potential could be separate in the thermo-elastic contribution ψ_e, the plastic contribution ψ_p and the thermal contribution ψ_T. For mechanical applications, it is more convenient to consider the Gibbs specific free enthalpy ψ^*, deduced from the Helmholtz free energy by a Legendre transformation on the strain, allowing to express the potential state as a function of the stress variable and to take in account of damage evolution (i.e. effective stress concept).

The Legendre transformation gives the punctual relation between an observable variable, the strain, and its associated one, the stress as follows:

$$\psi^* = \sup_{\varepsilon} \left[\frac{\mathbf{1}}{\rho} \sigma_{\mathbf{ij}} \varepsilon_{\mathbf{ij}} - \psi \right] \tag{2.9}$$

The formal definition could be split by superimposition of the elastic, the plastic and the thermal contributes:

$$\psi^* = \sup_{\varepsilon^{\mathbf{e}}} \left[\frac{\mathbf{1}}{\rho} \sigma_{\mathbf{ij}} \varepsilon^{\mathbf{e}}_{\mathbf{ij}} - \psi^{\mathbf{e}} \right] + \frac{\mathbf{1}}{\rho} \sigma_{\mathbf{ij}} \varepsilon^{\mathbf{p}}_{\mathbf{ij}} - \psi_{\mathbf{p}} - \psi_{\mathbf{T}} \tag{2.10}$$

where:

- ρ: density;
- ψ_p and ψ_T: do not depend on the total strain.

Consequently the state potential could be finally expressed as follows:

$$\psi^* = \psi^*_{\mathbf{e}} + \frac{\mathbf{1}}{\rho} \sigma_{\mathbf{ij}} \varepsilon^{\mathbf{p}}_{\mathbf{ij}} - \psi_{\mathbf{p}} - \psi_{\mathbf{T}} \tag{2.11}$$

The main properties of state potential ψ^* are:

- ψ^*_e : elastic contribution, which is affected by damage to model the experimentally-observed coupling between elasticity and damage through the effective stress concept;
- $\psi_p = \frac{1}{\rho} \left(\int_o^r R dr + \frac{1}{3} C \alpha_{ij} \alpha_{ij} \right)$: contribution due to the plastic hardening. If multiplied by ρ it gives the so called stored energy (ω_s) in the RVE. C is a material parameter that take into account the linear kinematic hardening;
- ψ_T : thermal contribution, defined only as a function of the temperature expressing the heat capacity of the material.

It is now possible to obtain the state laws as follows:

- the first two equations are the laws of thermoelasticity:

$$\begin{aligned} \varepsilon_{ij} &= \rho \frac{\delta \psi^*}{\delta \sigma_{ij}} = \rho \frac{\delta \psi^*_e}{\delta \sigma_{ij}} + \varepsilon^p_{ij} \longrightarrow \varepsilon^e_{ij} = \rho \frac{\delta \psi^*}{\delta \sigma_{ij}} \\ s &= \frac{\delta \psi^*}{\delta T} \end{aligned} \tag{2.12}$$

- the following equations define the associated variables:

$$
\begin{aligned}
R &= -\rho \frac{\delta \psi^*}{\delta r} \\
X_{ij} &= -\rho \frac{\delta \psi^*}{\delta \alpha_{ij}} \\
-Y &= -\rho \frac{\delta \psi^*}{\delta D}
\end{aligned}
\tag{2.13}
$$

The state laws must check the second principle of thermodynamics written as Clausius-Duhem inequity.
Consequently the damage rate should be positive, which is congruent with irreversibility of damage:

$$\sigma_{\mathbf{ij}} \dot{\varepsilon}^{\mathbf{p}}_{\mathbf{ij}} - \dot{\omega}_{\mathbf{s}} + \mathbf{Y_{ij}} \dot{\mathbf{D}}_{\mathbf{ij}} - \frac{\mathbf{q_i T_{,i}}}{\mathbf{T}} \geq \mathbf{0} \tag{2.14}$$

where:

- $\sigma_{ij} \dot{\varepsilon}^{p}_{ij}$: dissipation due to plastic power;
- $\dot{\omega}_s = R\dot{r} + X_{ij} \dot{\alpha}_{ij}$: stored energy density rate;
- $Y_{ij} \dot{D}_{ij}$: dissipation due to the damage;
- $\frac{q_i T_{,i}}{T}$: thermal energy.

The energy coming up from the balance of different dissipations is transformed into heat.

2.2.3 Dissipation Potential

The state laws are now defined and they are function of the state variables.
Following the same adopted procedure to identify the state laws, we have to formalize the kinematic laws modeling damage evolution. This kinematic laws are derived by a dissipation potential F which is a convex function of state variables in order to ensure the fulfillment with the second principle of thermodynamics:

$$\mathbf{F} = \mathbf{F} \left(\sigma, \mathbf{R}, \mathbf{X_{ij}}, \mathbf{Y_{ij}}, \mathbf{D_{ij}}, \mathbf{T} \right) \tag{2.15}$$

The dissipation potential represents the contribution of different phenomena; the principal contributes acting in any material subjected to fatigue condition are represented by:

- f: plastic criterion function;
- F_X: nonlinear kinematic hardening;
- F_D: damage potential.

So F could be decomposed as:

$$\mathbf{F} = \mathbf{f} + \mathbf{F_X} + \mathbf{F_D} \tag{2.16}$$

The evolution laws are formally written as follow:

$$\begin{aligned}
\dot{\varepsilon}^p_{ij} &= -\dot{\lambda}\frac{\delta F}{\delta\left(-\sigma_{ij}\right)} = \dot{\lambda}\frac{\delta F}{\delta\sigma_{ij}} \\
\dot{r} &= -\dot{\lambda}\frac{\delta F}{\delta R} \\
\dot{\alpha_{ij}} &= -\dot{\lambda}\frac{\delta F}{\delta X_{ij}} \\
\dot{D} &= -\dot{\lambda}\frac{\delta F}{\delta\left(-Y\right)} = \dot{\lambda}\frac{\delta F}{\delta Y}
\end{aligned} \tag{2.17}$$

It is useful to underline that plasticity is time-independent phenomenon. Thus, the potential F is not time-differentiable and $\dot{\lambda}$ is the so called plastic multiplier, calculated from the consistency condition, $f = 0$, $\dot{f} = 0$. The first condition, $f = 0$, means that the state of stress is on the actual yield condition; the second, $\dot{f} = 0$, means that stress state increase induces the yield stress to growth up. Elastic unloading occurs when $f \leq 0$ or $\dot{f} \leq 0$ (consequently the internal variables get a constant value) and this situation is commonly described by Kuhn−Tucker conditions:

$$\dot{\lambda} \geq \mathbf{0},\ \ \mathbf{f} \leq \mathbf{0},\ \ \dot{\lambda}\mathbf{f} = \mathbf{0} \tag{2.18}$$

The plastic multiplier λ here introduced, is a constant of proportionality which could be a scalar or a tensorial quantity coming from theory of plasticity.

To complete the formal description of elasto-plasticity coupled with damage, the accumulated plastic strain rate, $\dot{p}$, is defined in accordance with the yield criterion considered. In case of von Mises criterion, λ become:

$$\dot{\mathbf{p}} = \sqrt{\frac{\mathbf{2}}{\mathbf{3}}\dot{\varepsilon}^{\mathbf{p}}_{\mathbf{ij}}\dot{\varepsilon}^{\mathbf{p}}_{\mathbf{ij}}} \tag{2.19}$$

The remarks here introduced have a wide validity and they depend on which form is given to potential expression.

2.3 State Potential for Isotropic Damage

In this section, a specific state potential is presented for isotropic thermo-elasticity considering damage as an isotropic phenomenon. Following this approximations, the state potential is given by:

$$\rho\psi^{\star} = \frac{\mathbf{1}+\nu}{\mathbf{2E}}\frac{\sigma_{\mathbf{ij}}\sigma_{\mathbf{ij}}}{\mathbf{1}-\mathbf{D}} - \frac{\nu}{\mathbf{2E}}\frac{\sigma^{\mathbf{2}}_{\mathbf{kk}}}{\mathbf{1}-\mathbf{D}} + \alpha\left(\mathbf{T}-\mathbf{T_{ref}}\right)\delta_{\mathbf{ij}} \tag{2.20}$$

where:

- E: Young's modulus;
- ν: Poisson's ratio;
- α: thermal expansion coefficient;
- T_{ref}: reference temperature.

Following the standard procedure previously discussed it is possible to identify the state laws introducing the effective stress concept:

- the thermo-elasticity law is derived from this potential:

$$\varepsilon^{\mathbf{e}}_{\mathbf{ij}} = \rho\frac{\delta\psi^{\star}_{\mathbf{e}}}{\delta\sigma_{\mathbf{ij}}} = \frac{\mathbf{1}+\nu}{\mathbf{E}}\tilde{\sigma}_{\mathbf{ij}} - \frac{\nu}{\mathbf{E}}\tilde{\sigma}_{\mathbf{kk}}\delta_{\mathbf{ij}} + \alpha\left(\mathbf{T}-\mathbf{T_{ref}}\right)\delta_{\mathbf{ij}} \tag{2.21}$$

- the energy density release rate (Y) is written as (J.L. Chaboche):

$$\mathbf{Y} = \rho\frac{\delta\phi^{\star}}{\delta\mathbf{D}} = \frac{\tilde{\sigma}^{\mathbf{2}}_{\mathbf{eq}}\mathbf{R_v}}{\mathbf{2E}} \tag{2.22}$$

R_v is the so called triaxiality function:

$$\mathbf{R_v} = \frac{\mathbf{2}}{\mathbf{3}}\left(\mathbf{1}+\nu\right) + \mathbf{3}\left(\mathbf{1}-\mathbf{2}\nu\right)\left(\frac{\sigma_{\mathbf{H}}}{\sigma_{\mathbf{eq}}}\right)^{\mathbf{2}} \tag{2.23}$$

where

- $\sigma_H = \frac{\sigma_{kk}}{3}$: hydrostatic stress;
- $\sigma_{eq} = \sqrt{\frac{3}{2}\sigma ij^D \sigma ij^D}$: von Mises equivalent stress;
- $\sigma_{ij}^D = \sigma_{ij} - \sigma_H \delta_{ij}$: stress deviator;
- $\frac{\sigma_H}{\sigma_{eq}} = T_X$: stress triaxiality.

2.4 Isotropic Unified Damage Law

The adopted thermodynamic approach gives evidence that damage evolution depends on the released energy density rate (Y). For a complete damage evolution law formulation one needs a dissipation potential from which derive the kinematic laws. As previously discussed, the dissipation potential takes in account the plastic dissipation (f), the kinematic hardening (F_X) and the damage dissipation (F_D). F_D gives the main contribution and the other two quantities may be neglected. So J.Lemaitre suggest for the damage dissipation function the following expression:

$$\mathbf{F_D} = \frac{\mathbf{S}}{(\mathbf{s+1})\,(\mathbf{1-D})\left(\frac{\mathbf{Y}}{\mathbf{S}}\right)^{\mathbf{s+1}}} \tag{2.24}$$

From the state laws the damage rate is given by:

$$\dot{\mathbf{D}} = \dot{\lambda}\frac{\delta \mathbf{F_D}}{\delta \mathbf{Y}} \tag{2.25}$$

Finally, for substitution of eq.2.24 in eq.2.25 damage evolution law is derived:

$$\dot{\mathbf{D}} = \left(\frac{\mathbf{Y}}{\mathbf{S}}\right)^{\mathbf{s}} \dot{\mathbf{p}} \tag{2.26}$$

where S and s are two material parameters which are function of the temperature. The full damage constitutive equations take into account an energetic threshold below which no damage is expected.

$$\begin{aligned} \dot{D} &= \left(\frac{Y}{S}\right)^{s} \dot{p} \text{ if } \max \omega_s > \omega_D \text{ or } p > p_D \ , \\ \dot{D} &= 0 \text{ if not,} \\ D &= D_c \rightarrow \text{ mesocrack initiation.} \end{aligned} \tag{2.27}$$

where ω_D and D_c are material parameters related to damage initiation threshold. In the following section ω_D and D_c will be formalized.

2.4.1 Damage Threshold for Mesocrack Initiation

In accordance to the damage formulation, it is possible to individuate the amount of energy necessary for damage initiation and the relative condition for mesocrack initiation. This threshold corresponds to a certain accumulated plastic strain rate p_D which is a consequence of a specific stored energy threshold (ω_D) of the material.
As previously introduced, the stored energy is:

$$\omega_{\mathbf{s}} = \int_{\mathbf{0}}^{\mathbf{t}} (\mathbf{R}\dot{\mathbf{r}} + \mathbf{X_{ij}}\dot{\alpha}_{\mathbf{ij}}) \tag{2.28}$$

Experimental tests have shown that isotropic hardening saturates at a constant value $R = R_\infty$ for considerable p and recall that $p = r$ as long as there is no damage. Pointing out that $X_{ij} = \frac{2}{3}C\alpha_{ij}$, the following relation is obtained:

$$\omega_{\mathbf{s}} = \rho\psi_{\mathbf{p}} \approx \mathbf{R}_\infty \mathbf{p} + \frac{\mathbf{3}}{\mathbf{4C}}\mathbf{X_{ij}}\mathbf{X_{ij}} \rightarrow \text{ as long as } \mathbf{D} = \mathbf{0} \tag{2.29}$$

This last expression shows a linear dependency in p for large values of the accumulated plastic strain. Considering the tendency to reach a constant value asymptotically, the corresponding value of ω_s gets too higher values and is not possible to measure it. In order to perform a finite evaluation, the classical framework has to be corrected as introduced by A. Chrysochoos by rewriting the previous equation in terms of a new set of thermodynamics variables, (Q, q).
The correction function is represented by:

$$\mathbf{Z}(\mathbf{r}) = \frac{\mathbf{A}}{\mathbf{m}}\mathbf{r}^{\mathbf{1-m/m}} \tag{2.30}$$

where A and m are two material parameters. That leads to a new expression for ω_s:

$$\omega_{\mathbf{s}} = \int_{\mathbf{0}}^{\mathbf{t}} (\mathbf{Q}\dot{\mathbf{q}} + \mathbf{X_{ij}}\dot{\alpha}_{\mathbf{ij}})\,\mathbf{dt} = \int_{\mathbf{0}}^{\mathbf{t}} (\mathbf{R}(\mathbf{r})\mathbf{z}(\mathbf{r})\dot{\mathbf{r}} + \mathbf{X_{ij}}\dot{\alpha}_{\mathbf{ij}})\,\mathbf{dt} \tag{2.31}$$

The change of variables is written as:

$$\mathbf{Q}(\mathbf{q}) = \mathbf{R}(\mathbf{r}) \text{ and } \mathbf{dq} = \mathbf{z}(\mathbf{r})\mathbf{dr} \tag{2.32}$$

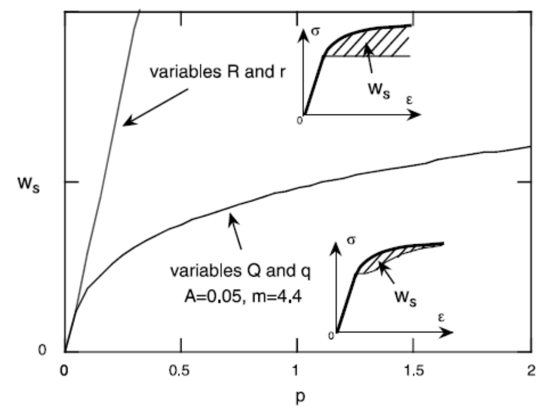

Figure 2.2: Impact of change of variables in damage threshold energy measurement.

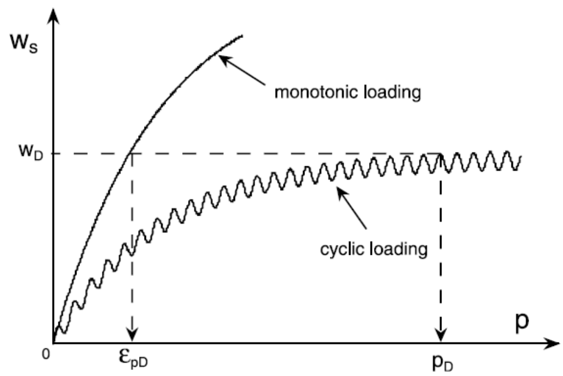

Figure 2.3: Loading dependency of the damage in terms of accumulated plastic strain.

The evolution of ω_s is expressed in the new set of variables by:

$$\omega_{\mathbf{s}} \approx \mathbf{AR_\infty p^{1/m}} + \frac{\mathbf{3}}{\mathbf{4C}}\mathbf{X_{ij}X_{ij}} \rightarrow \text{ as long as } \mathbf{D} = \mathbf{0} \tag{2.33}$$

The validity of this change of variables could be appreciated looking at fig.2.2.

Nothing else in the constitutive equations is modified.

Damage will not initiate until the corrected stored energy reaches a threshold value and the so derived threshold stored energy (ω_D) may be considered as a material parameter. The loading dependency of the damage in terms of accumulated plastic strain could be represented as a consequence of the above consideration as illustrated in fig.2.3.

For practical applications, the threshold value has been derived by reference to the true limit of irreversibility taken as the asymptotic fatigue limit σ_f^∞:

$$\omega_{\mathbf{D}} = \int_{\mathbf{0}}^{\varepsilon_{\mathbf{pD}}} \left(\sigma_{\mathbf{u}} - \sigma_{\mathbf{f}}^{\infty}\right) \frac{\mathbf{A}}{\mathbf{m}} \varepsilon_{\mathbf{p}}^{(\mathbf{1}-\mathbf{m})/\mathbf{m}} \mathbf{d}\varepsilon_{\mathbf{p}} \tag{2.34}$$

or

$$\omega_{\mathbf{D}} = \mathbf{A}\left(\sigma_{\mathbf{u}} - \sigma_{\mathbf{f}}^{\infty}\right) \varepsilon_{\mathbf{pD}}^{\mathbf{1}/\mathbf{m}} \tag{2.35}$$

where:

- σ_u : ultimate stress in pure tension;
- ε_{pD} : damage threshold in pure tension;

If monotonic loadings are taken in account:

$$\mathbf{p_D} = \varepsilon_{\mathbf{pD}} \tag{2.36}$$

If cyclic loadings are taken in account some further consideration have to be introduced.

If $\sigma_{min} \leq 0$ and $\sigma_{max} > 0$, the contribution in the stored energy due to kinematic hardening is small and may be neglected. Moreover, perfect plasticity has to be taken in account in relation to maximum and minimum stress. This considerations allow to write:

$$\begin{aligned} \omega_D &= \frac{1}{2}\int_o^{pD} \left(\sigma_{max} - \sigma_f^\infty\right) \frac{A}{m} p^{1-m/m} dp + \\ &+ \frac{1}{2}\int_o^{pD} \left(\mid \sigma_{min} \mid - \sigma_f^\infty\right) \frac{A}{m} p^{1-m/m} dp \\ &= A\left(\frac{\sigma_{max} + \mid \sigma_{min} \mid}{2} - \sigma_f^\infty\right) p_D^{1/m} \end{aligned} \tag{2.37}$$

Defining $\Delta\sigma = \sigma_{max} - \sigma_{min}$ the stress range at which correspond a plastic strain range $\Delta\varepsilon_p$, (equation 2.37) gives the threshold p_D as a loading-dependent function of the threshold in pure tension (1-D approximation) (ε_{pD}):

$$\mathbf{p_D} = \varepsilon_{\mathbf{pD}} \left(\frac{\sigma_{\mathbf{u}} - \sigma_{\mathbf{f}}^{\infty}}{\frac{\sigma_{\mathbf{max}} - |\sigma_{\mathbf{min}}|}{\mathbf{2}} - \sigma_{\mathbf{f}}^{\infty}}\right)^{\mathbf{m}} = \varepsilon_{\mathbf{pD}} \left(\frac{\sigma_{\mathbf{u}} - \sigma_{\mathbf{f}}^{\infty}}{\frac{\boldsymbol{\Delta}\sigma}{\mathbf{2}} - \sigma_{\mathbf{f}}^{\infty}}\right)^{\mathbf{m}} \tag{2.38}$$

For 3-D cyclic loadings such as $(\Delta\sigma)_{eq} = \sigma_{eq.max} - \sigma_{eq.min}$, it can be written as:

$$\mathbf{p_D} = \varepsilon_{\mathbf{pD}} \left(\frac{\sigma_{\mathbf{u}} - \sigma_{\mathbf{f}}^{\infty}}{\frac{(\boldsymbol{\Delta}\sigma)_{\mathbf{eq}}}{\mathbf{2}} - \sigma_{\mathbf{f}}^{\infty}}\right)^{\mathbf{m}} \tag{2.39}$$

It is useful to remember that this closed forms are approximations introduced for practical applications, but for a rigorous threshold evaluation the relationship which has to be followed is:

$$\mathbf{max}\ \omega_{\mathbf{s}} = \omega_{\mathbf{D}} \rightarrow \text{ for damage initiation} \tag{2.40}$$

2.5 Parameters Identification

The purpose of this section is to give standard procedures which lead to identify all introduced material parameters. This identification may be possible extracting parameters from material handbooks, but it is often difficult particularly for specific materials. With just a few material tests it is possible to achieve all material parameters. So, in this section this experimental procedures are presented, while in chapter 4 the design of a simple fatigue tensile machine is presented.

2.5.1 Correction Parameters Identification (A, m)

To identify the stored energy threshold ω_D for damage initiation, two parameters have been introduced (A, m). Two experiments with damage measurements give the threshold of monotonic tension (ε_p^D) and in fatigue (p_D) for a known plastic strain range $(\Delta\varepsilon_p)$.
The stored energy in monotonic tension is given by:

$$\omega_{\mathbf{s}} = \frac{\mathbf{A}}{\mathbf{m}} \int_{\mathbf{0}}^{\varepsilon_{\mathbf{pD}}} \mathbf{R}\left(\mathbf{p}\right) \mathbf{p}^{(\mathbf{1}-\mathbf{m})/\mathbf{m}} \mathbf{dp} + \frac{\mathbf{X}^{\mathbf{2}}\left(\varepsilon_{\mathbf{p}}^{\mathbf{D}}\right)}{\mathbf{2C}} = \omega_{\mathbf{D}} \tag{2.41}$$

The stored energy in cyclic loading is given by:

$$\omega_{\mathbf{s}} = \frac{\mathbf{A}}{\mathbf{m}} \int_{\mathbf{0}}^{\mathbf{p_D}} \mathbf{R}\left(\mathbf{p}\right) \mathbf{p}^{(\mathbf{1}-\mathbf{m})/\mathbf{m}} \mathbf{dp} + \frac{\mathbf{X}_{\mathbf{max}}^{\mathbf{2}}}{\mathbf{2C}} = \omega_{\mathbf{D}} \tag{2.42}$$

where:

- $R(p) = R_\infty \left[1 - \ \exp\ (-bp)\right]$: for exponential isotropic hardening;
- $X(\varepsilon_{pD}) = C\varepsilon_{pD}$: for linear kinematic hardening in monotonic loading;

- $X_{max} = C\varepsilon_{pmax} = C\Delta\varepsilon_p/2$: for linear kinematic hardening in fatigue loading at zero mean stress;

- R_∞, b, C, γ and $X_\infty = C/\gamma$ are hardening parameters.

From equation 2.39 m could be directly derived:

$$\mathbf{m} = \frac{\ln \frac{\mathbf{p_D}}{\varepsilon \mathbf{pD}}}{\ln\left(\frac{\sigma_\mathbf{u} - \sigma_\mathbf{f}^\infty}{\boldsymbol{\Delta}\sigma/\mathbf{2} - \sigma_\mathbf{f}^\infty}\right)} \tag{2.43}$$

The other parameter A is obtained by comparison between eq.2.41 and eq.2.42 with the hypothesis of saturated hardening at damage initiation:

$$\mathbf{A} \approx \frac{\mathbf{X}_\infty}{\mathbf{2}\gamma\mathbf{R}_\infty} \frac{\mathbf{1} - \mathbf{tanh^2} \frac{\gamma \boldsymbol{\Delta}\varepsilon_\mathbf{p}}{\mathbf{2}}}{\mathbf{p_d^{1/m}} - \varepsilon_\mathbf{pD}^\mathbf{1/m}} \tag{2.44}$$

Finally, one needs to determinate ω_D, which as previously mentioned could be considered as a material parameter:

$$\begin{aligned} \omega_D \quad &= \quad \frac{AR_\infty}{m} \int_0^{\varepsilon_p^D} \left[1 - \exp\left(-bp\right)\right] p^{1-m/m} dp \\ &\quad + \frac{X_\infty^2 \left[1 - \exp\left(-\gamma\varepsilon_{pD}\right)\right]^2}{2C} \end{aligned} \tag{2.45}$$

As a consequence of the physical behavior of damage evolution phenomenon, it is possible to state that a mesocrack initiate when the density of defects reaches the value at which the localization and instability process develops, formally representable by $D = D_c$, with D_c is a threshold material parameter. A way to evaluate D_c is to apply the concept of effective stress at fracture, introducing a fundamental idea:

In a pure tensile test when damage develops at saturated hardening, the stress decreases from the ultimate stress σ_u to the rupture stress σ_R. This decrease is congruent with damage initiation, which may reduce material constitutive properties.

Following the description of isotropic damage:

$$\tilde{\sigma}_\mathbf{R} = \sigma_\mathbf{u} \text{ or } \frac{\sigma_\mathbf{R}}{\mathbf{1} - \mathbf{D_c}} = \sigma_\mathbf{u} \tag{2.46}$$

from which a direct evaluation of D_c as a material parameter is possible:

$$\mathbf{D_c = 1 - \frac{\sigma_R}{\sigma_u}} \tag{2.47}$$

2.5.2 Material Parameters Identification

If no material data are available, or if their sources are not completely reliable, the parameters identification is allowed by few material tests. The main parameters that are needed for damage evaluation are represented by:

- E, ν, S, s : damage law parameters;
- $\varepsilon_{pD}, \sigma_f^\infty, \sigma_u, m$: damage threshold parameters;
- D_c : condition for mesocrack initiation.

For a complete parameters identifications both tensile and low cycle fatigue test are required.

Identification from a Tensile Test

As illustrated in fig.5.7 a uniaxial tensile test could give:

- E, ν : respectively the Young modulus and the Poisson ratio;
- σ_y : the yield stress (the conventional yield stress is $\sigma_{y02} = \sigma_{\varepsilon_p = 0.2 \cdot 10^{-2}}$);
- σ_u : the ultimate stress;
- σ_R : the rupture stress (with the associated plastic strain ε_{pR});
- $Z = \frac{S_0 - S_R}{S_0}$: necking parameter (with S_0 the initial specimen section and S_R its final one).

The hardening may saturated at σ_u in uniaxial, isotropic damage law in monotonic loading leading to:

$$\mathbf{\dot{D}} = \left(\frac{\boldsymbol{\sigma}_\mathbf{u}^\mathbf{2}}{\mathbf{2ES}}\right)^\mathbf{s} \dot{\boldsymbol{\varepsilon}}_\mathbf{p} \tag{2.48}$$

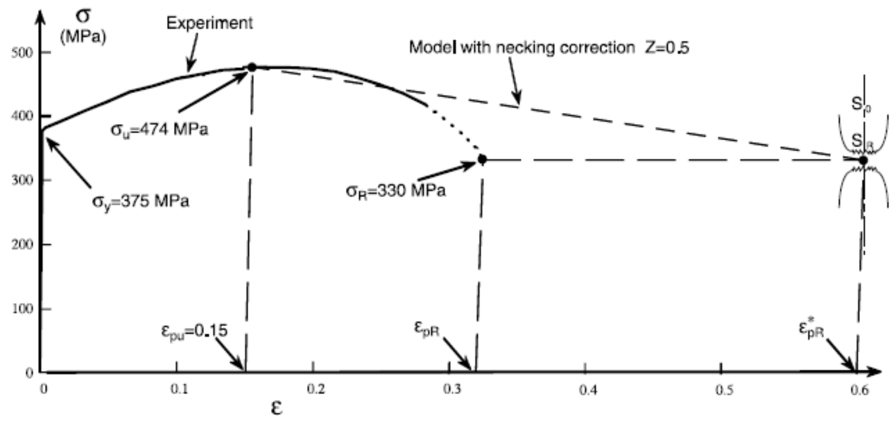

Figure 2.4: Material parameters from a tension test on ferritic steel at room temperature. Engineering Damage Mechanics: Ductile, Creep, Fatigue and Brittle Failures; Springer.

Pointing that $D = 0$ if $\varepsilon_p \leq \varepsilon_{pD}$, by integration of damage law:

$$\mathbf{D} = \left(\frac{\sigma_{\mathbf{u}}^{\mathbf{2}}}{\mathbf{2ES}}\right)^{\mathbf{s}} (\varepsilon_{\mathbf{p}} - \varepsilon_{\mathbf{pD}}) \tag{2.49}$$

where:

- $\varepsilon_{pD} \approx \varepsilon_p (\sigma = \sigma_u)$: damage will not grow up until the plastic strain reaches the ultimate stress value.

If damage is initiated, the local rupture strain in the necking region $(\varepsilon^\star_{pR})$ should be estimated from the necking parameter Z, under the hypothesis of plastic incompressibility $\left(\varepsilon^p_{kk} = 0\right)$:

$$\varepsilon^\star_{\mathbf{pR}} = \mathbf{2}\left(\mathbf{1} - \sqrt{\mathbf{1} - \mathbf{Z}}\right) \tag{2.50}$$

Finally:

$$\mathbf{D_c} = \left(\frac{\sigma_{\mathbf{u}}^{\mathbf{2}}}{\mathbf{2ES}}\right)^{\mathbf{s}} \left(\varepsilon^\star_{\mathbf{pR}} - \varepsilon_{\mathbf{pD}}\right) \tag{2.51}$$

To go further with the identification of S, s and m three fatigue tests are required.

Identification from Fatigue Tests

The first fatigue test is to investigate the value of the engineering fatigue limit (σ_f), which correspond to a number of cycle to failure of

10^6 or 10^7. It should be used instead of the asymptotique fatigue limit (σ_f^∞) which is a result of statistical analysis. The damage evolution law could be applied (especially for LCF) assuming that the material is perfectly plastic for each level of stress:

$$\mathbf{\dot{D}} = \left[\frac{\sigma^{\mathbf{2}}_{\mathbf{max}}}{\mathbf{2ES\,(1-D)^2}}\right]^{\mathbf{s}} \mathbf{\dot{p}} \tag{2.52}$$

Assuming $\dot{p} = \mid \dot{\varepsilon}_p \mid$ and neglecting the variation of D during one load cycle, the integration of damage law over this cycle gives:

$$\frac{\delta\mathbf{D}}{\delta\mathbf{N}} = \int_{\mathbf{1cycle}} \mathbf{\dot{D}dt} = \left(\frac{\sigma^{\mathbf{2}}_{\mathbf{max}}}{\mathbf{2ES\,(1-D)^2}}\right)^{\mathbf{s}} \mathbf{2\Delta}\varepsilon_{\mathbf{p}} \tag{2.53}$$

where:

- $\Delta\varepsilon_p$: plastic strain range corresponding to applied σ_{max}.

Let's introduce:

- N_D : number of cycles corresponding to damage threshold;
- N_R : number of cycles corresponding to mesocrack initiation for $D = D_c$.

with a second integration over the whole initiation process:

$$\int_{\mathbf{0}}^{\mathbf{D_c}} \mathbf{(1-D)^{2s}}\,\delta\mathbf{D} = \left(\frac{\sigma^{\mathbf{2}}_{\mathbf{max}}}{\mathbf{2ES}}\right)^{\mathbf{s}} \mathbf{2\Delta}\varepsilon_{\mathbf{p}} \int_{\mathbf{N_D}}^{\mathbf{N_R}} \delta\mathbf{N} \tag{2.54}$$

that leads to:

$$\frac{\mathbf{1}}{\mathbf{2s+1}}\left[\mathbf{1-(1-D_c)\,2s+1}\right] = \left(\frac{\sigma^{\mathbf{2}}_{\mathbf{max}}}{\mathbf{2ES}}\right)^{\mathbf{s}} \mathbf{2\Delta}\varepsilon_{\mathbf{p}}\left(\mathbf{N_R-N_D}\right) \tag{2.55}$$

with N_D given by:

$$\mathbf{p_D} = \mathbf{2\Delta}\varepsilon_{\mathbf{p}}\mathbf{N_D} = \varepsilon_{\mathbf{pD}}\left(\frac{\sigma_{\mathbf{u}}-\sigma^{\infty}_{\mathbf{f}}}{\sigma_{\mathbf{max}}-\sigma^{\infty}_{\mathbf{f}}}\right)^{\mathbf{m}} \tag{2.56}$$

The number of cycles needed to initiate a mesocrack is finally expressed by:

$$\mathbf{N_R} = \frac{\varepsilon_{\mathbf{pD}}}{\mathbf{2\Delta}\varepsilon_{\mathbf{p}}}\left(\frac{\sigma_{\mathbf{u}}-\sigma^{\infty}_{\mathbf{f}}}{\sigma_{\mathbf{m}}\mathbf{ax}-\sigma^{\infty}_{\mathbf{f}}}\right)^{\mathbf{m}} + \frac{\mathbf{1-(1-D_c)^{2s+1}}}{\mathbf{2\,(2s+1)\,\Delta}\varepsilon_{\mathbf{p}}}\left(\frac{\sigma_{\mathbf{u}}}{\sigma_{\mathbf{m}}\mathbf{ax}}\right)^{\mathbf{s}} \tag{2.57}$$

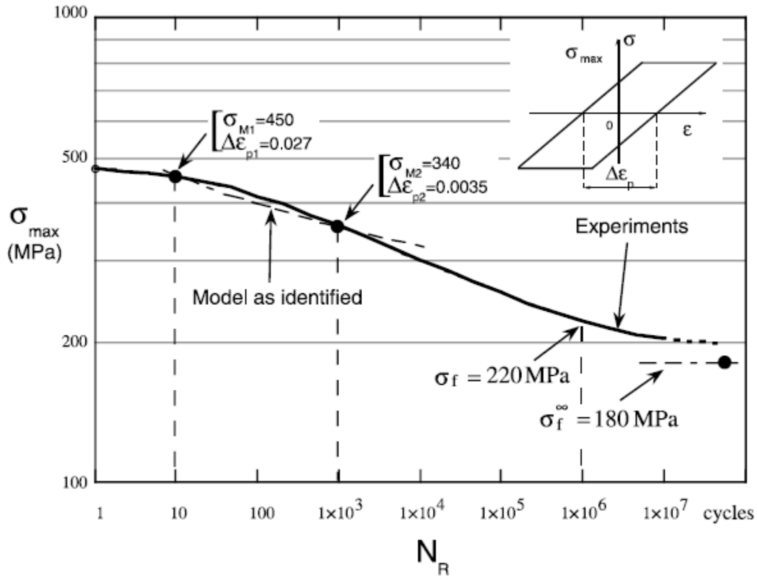

Figure 2.5: Material parameters from a Wohler curve of ferritic steel at room temperature. Engineering Damage Mechanics: Ductile, Creep, Fatigue and Brittle Failures; Springer.

From equation 2.51 comes that:

$$(\mathbf{2ES})^{\mathbf{s}} = \sigma_{\mathbf{u}}^{\mathbf{2s}} \left(\frac{\varepsilon^{\star}_{\mathbf{pR}} - \varepsilon_{\mathbf{pD}}}{\mathbf{D_c}} \right) \tag{2.58}$$

This allow to reformulate N_R as:

$$\begin{aligned} N_R \;\; &= \;\; \frac{\varepsilon_{pD}}{2\Delta\varepsilon_p} \left(\frac{\sigma_u - \sigma_f^{\infty}}{\sigma_m ax - \sigma_f^{\infty}} \right)^m + \\ &+ \;\; \frac{1-(1-D_c)^{2s+1}}{2\,(2s+1)\,D_c\Delta\varepsilon_p} \left(\frac{\sigma_u}{\sigma_m ax} \right)^{2s} \left(\varepsilon^{\star}_{pR} - \varepsilon_{pD} \right) \end{aligned} \tag{2.59}$$

Solving this equation for two differents low cycles fatigue tests, as illustrated in Fig. 5.8, a precise identification of s, m is achieved. The identification of the last parameter (S) is a consequence of equation 2.51:

$$\mathbf{S} = \frac{\sigma_{\mathbf{u}}^{\mathbf{2}}}{\mathbf{2E}} \left(\frac{\varepsilon^{\star}_{\mathbf{pR}} - \varepsilon_{\mathbf{pD}}}{\mathbf{D_c}} \right) \tag{2.60}$$

2.6 Localization of Mesocrack Initiation

In the previous section, a standard procedure to determine the number of cycles for mesocrack initiation has been presented. The aim of this section is to establish where cracks will initiate in a structure subjected to a cyclic load condition. There are two main approaches to investigate this problem, based on the instability coming from mesocrack initiation:

- Bifurcation approach of localization: it is proper of such problems which are time-independent;

- Perturbation approach of localization: it is proper of both time-independent and time-dependent problems.

For the purposes of this work the previous approaches will no more treated here and the study of mesocrack localization will be faced from a practical point of view. Remembering that mesocrack initiation is considered like the ultimate state of plastic strain accumulation, the answer at localization question is given. To perform a reliable mesocrack localization, a structural analysis calculation with Finite Element Method is required. By investigating the strain resulting from a monotonic load application, one has as a result of finite element analysis (FEA) the localization of such points that are subjected to maximum strain. So in this points damage may rise up and mesocrack is expected.
The most precise approach to investigate maximum plastic strain localization is to perform an elasto-plastic structure evaluation to take into account the physical behaviour of metal deformations. Elasto-plastic analysis will be very expensive (from a computational point of view) and quite difficult to perform if the structure subjected to FEA has a complex geometry. In first approximation a simple elastic computation could be appreciable enough to obtain mesocrack localization.
There are also analytical procedures to correct elastic computation, represented by:

- Neuber Method: gives a local plastic correction of an elastic computation resulting from a monotonic applied loading;

- Strain Energy Density Method (SED): gives a local plastic correction of an elastic computation resulting from cyclic applied loading.

As for localization approaches, they will no further delved in the present work, and they will be object of further studies.
It is now possible to establish where a mesocrack will initiate and the number of cycles for mesocrack initiation, consequently in the next section a procedure to establish macrocrack initial size will be presented.

2.7 Size and Orientation of Macrocrack Initiated

The constitutive equations of damage model are efficient until crack remain in the RVE domain. Then Fracture Mechanics (FM)(see Chapter 3) concepts are more appropriate to investigate macrocrack growth. If damage analysis has to be followed by a fracture mechanics analysis the macrocrack initial size and its orientation are required. The initial size of a macrocrack is the result of the following idea:

- The mesocrack initiation investigated by Continuum Damage Mechanics reaches its maximum extension, corresponding to minimum extension at which a Fracture Mechanics crack is available. This point of intersection between this two disciplines could be represented by two distinct processes which involve the same amount of energy.

This idea has been formalized by J.Mazars who defined:

- ϕ_{Dp} : dissipated energy resulting from CDM evaluation;
- ϕ_F : dissipated energy resulting from FM evaluation.

With isotropic damage restriction, the energy dissipated in damage process is given by:

$$\phi_{\mathbf{D}} = \delta_{\mathbf{0}}^{\mathbf{3}} \int_{\mathbf{0}}^{\mathbf{D_c}} \mathbf{YdD} \tag{2.61}$$

Assuming saturated hardening and a triaxiality function of $R_V = 1$ as the crack is expected to initiate at the surface where the stress state is often uniaxial, the following relation is obtained:

$$\phi_{\mathbf{D}} \approx \delta_{\mathbf{0}}^{\mathbf{3}} \frac{\sigma_{\mathbf{u}}^{\mathbf{2}}}{\mathbf{2E}} \mathbf{D_c} \tag{2.62}$$

At the same time, the dissipated energy related to plasticity process is:

$$\phi_{\mathbf{p}} = \int_{\mathbf{0}}^{\mathbf{fracture}} \sigma_{\mathbf{ij}} \mathbf{d} \varepsilon_{\mathbf{ij}}^{\mathbf{p}} \tag{2.63}$$

If proportional or uniaxial loading are taken in account:

$$\phi_{\mathbf{p}} = \delta_{\mathbf{0}}^{\mathbf{3}} \int_{\mathbf{0}}^{\mathbf{p_R}} \sigma_{\mathbf{eq}}(\mathbf{p}) \mathbf{dp} \tag{2.64}$$

where p_R is the accumulated plastic strain at rupture (for which $\sigma_{eq} \approx \sigma_u$ and $p_R = \varepsilon_{p_R}$ in pure tension).Then:

$$\phi_{\mathbf{D_p}} = \phi_{\mathbf{D}} + \phi_{\mathbf{p}} \approx \delta_{\mathbf{0}}^{\mathbf{3}} \left(\frac{\sigma_{\mathbf{u}}^{\mathbf{2}}}{\mathbf{2E}} \mathbf{D_c} + \sigma_{\mathbf{u}} \varepsilon_{\mathbf{pR}} \right) \tag{2.65}$$

The same amount of energy is evaluated trough FM concepts, dealing with a crack area $A = \delta_0^2$ and a strain energy release rate G:

$$\phi_{\mathbf{F}} = \int_{\mathbf{0}}^{\mathbf{A_0}} \mathbf{GdA} \tag{2.66}$$

For simplicity, the upper bound on ϕ_F is given by the maximum value G_c of G, the material toughness. This leads to:

$$\phi_{\mathbf{F}} = \mathbf{G_c} \delta_{\mathbf{0}}^{\mathbf{2}} \tag{2.67}$$

Requiring an energy balance between ϕDp and ϕ_F, δ_0 is given:

$$\delta_{\mathbf{0}} \approx \frac{\mathbf{G_c}}{\frac{\sigma_{\mathbf{u}}^{\mathbf{2}}}{\mathbf{2E}} \mathbf{D_c} + \sigma_{\mathbf{u}} \varepsilon_{\mathbf{pR}}} \tag{2.68}$$

Finally, using isotropic damage approximation, the macrocrack orientation is given by the maximum principal stress:

$$\vec{n} = \vec{n}\ \mathbf{max}\left(\sigma_{\mathbf{I}}\right) \tag{2.69}$$

In the next chapter Fracture Mechanics theory will be presented to give a complete description of the nature of G (and also G_c). Moreover Fracture Mechanics theory gives the instrument to perform a complete macrocrack growth evaluation.

2.8 References

Engineering Damage Mechanics: Ductile, Creep, Fatigue and Brittle Failures; J.Lemaitre, R. Desmorat; Springer.

Mechanics of Solid Material; J. Lemaitre, J.L. Chaboche.

Chapter 3

Fracture Mechanics

Following the approaches described in Chapter 1 and in Chapter 2, we are now able to evaluate:

- Where a crack may initiate;
- Its initial macroscopic dimension;
- The macrocrack initial orientation.

To obtain a complete description of macrocrack initial size, it is necessary to define a criterion allowing to evaluate the previously introduced critical amount of energy, G_c. Moreover, to correctly investigate crack propagation, the so called stress intensity factor K is required.
Consequently, in this chapter the 'Griffith Fracture Theory', which allows to calculate G_c will firstly described. Secondly, 'Linear Elastic Fracture Mechanics (LEFM)' , which is a theory to calculate the stress intensity factor, will be introduced. Considering also that the $S-N$ and $\varepsilon-N$ techniques, which are usually appropriate for situations where a component or structure can be considered a continuum (i.e., with 'no cracks' assumption), offer no support in the event of a discontinuity like a crack, the Fracture Mechanics approach, which is based on the relationship between ΔS and ΔK, results the most appropriate method to investigate macrocrack propagation.
This approach usually is based on three different theories:

- Griffith Fracture Theory;
- Linear Elastic Fracture Mechanics (LEFM);
- Elastic-Plastic Fracture Mechanics (EPFM).

3.1 Griffith Fracture Theory

Griffith Fracture Theory [26] [27] establishes a criterion based on rate of energy release especially for brittle materials, but its validity offers appreciable result also for ductile ones.
The 'theory of elasticity' evidences that the strain energy per unit volume, contained in a linear-elastic body, is the area under the stress-strain curve:

$$\mathbf{U_0} = \frac{\mathbf{S^2}}{\mathbf{2E}} \tag{3.1}$$

where:

- S: applied stress;
- E: Young's modulus.

In consequence of the rising of a crack in material surfaces, there is a release of energy in an elastic body. This energy release is determined by the inability of the crack surface to support a load. It is possible to round up the volume of material whose energy is released with the area of an elliptical region around the crack, times the plate thickness, B (Fig.3.1); the volume is given by:

$$\mathbf{V} = \pi(\mathbf{2a}) \cdot (\mathbf{aB}) \tag{3.2}$$

This, considering that the area of an ellipse is $\pi \cdot r_a \cdot r_b$, where r_a and r_b are respectively the major and minor radius of the ellipse.
The total energy released from the body, due to the crack extension, is the energy per unit volume times the volume, which is:

$$\mathbf{U} = \pi(\mathbf{2a}) \cdot (\mathbf{aB}) \cdot \left(\frac{\mathbf{S^2}}{\mathbf{2E}}\right) = \pi \cdot \frac{\mathbf{S^2a^2B}}{\mathbf{E}} \tag{3.3}$$

In ideal brittle solids, the released energy could be bridged only by

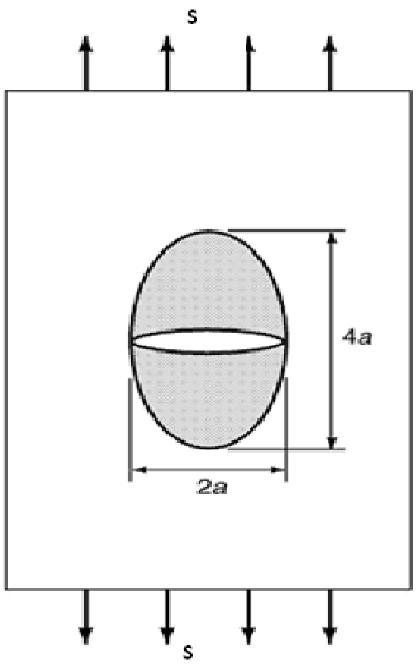

Figure 3.1: Schematic illustration of the concept of energy release around a centre crack in a loaded plate.

the surface energy absorbed, which is:

$$\mathbf{W} = (\mathbf{2aB})(\mathbf{2}\gamma_\mathbf{s}) = \mathbf{4aB}\gamma_\mathbf{s} \cdot (\mathbf{aB}) \tag{3.4}$$

where

- $2aB$: crack area ;
- $2\gamma_s$ twice the surface area (there are two crack surfaces).

Griffith's energy-balance criterion establish that crack growth will occur when the amount of energy released due to an increment of crack advance is larger than the amount of energy absorbed:

$$\frac{\mathbf{dU}}{\mathbf{da}} \geq \frac{\mathbf{dW}}{\mathbf{da}} \tag{3.5}$$

Performing the derivatives indicated in eq.3.5, Griffith criterion for crack growth is:

$$\sqrt{\mathbf{S}(\pi\mathbf{a})} = \sqrt{\mathbf{2}\gamma_\mathbf{s}\mathbf{E}(\pi\mathbf{a})} \tag{3.6}$$

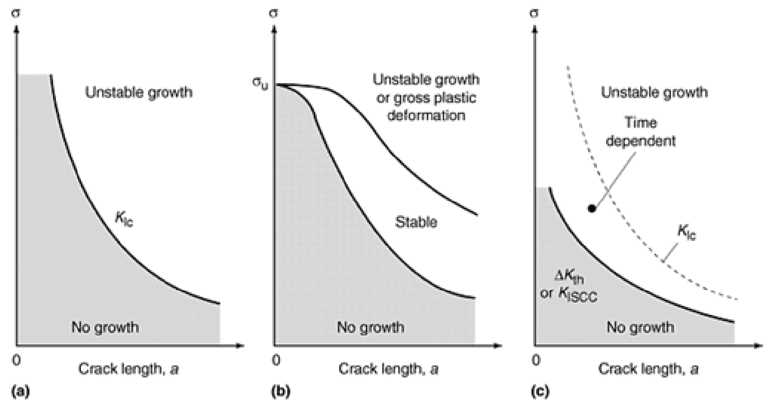

Figure 3.2: Relationships between stress and crack length, showing regions and types of crack growth. (a) Linear-elastic; (b) Elastic-plastic; (c) Subcritical. ASM Metals Hand-Book Volume 19 - Fatigue And Fracture.

Fracture theory was built upon this criterion in the early 1940s by considering that the critical strain energy release rate, G_c, required for crack growth was equal to twice an effective surface energy, γ_{eff}:

$$\mathbf{G_c = 2\gamma_{eff}} \tag{3.7}$$

Anyway, γ_{eff} is basically the plastic energy absorption around the crack tip, with only a small part due to the surface energy of the crack surfaces. Subsequently, with numerical techniques development, to define the stress fields near cracks, this energy relationship was supplemented by stress concepts (i.e., the stress-intensity factor, K, and a critical value of K for crack growth, K_c). Replacing γ_s with γ_{eff} in eq.3.6 and noting that the energy and stress concepts are essentially identical, gives:

$$\mathbf{K_c = \sqrt{EG_c} = S\sqrt{\pi a}} \tag{3.8}$$

which is the crack-growth-criterion equivalent of (Eq.3.1).
K_c is the critical value of K that, when it is exceeded by a combination of applied stress and crack length, involve to crack growth. For thick-plate in plane-strain conditions, this critical value is named 'plane-strain fracture toughness', K_{I_c}, and any combination of applied stress and crack length that exceeds this value produce unstable crack growth (Fig.3.2). This forms the basis for understanding the rela-

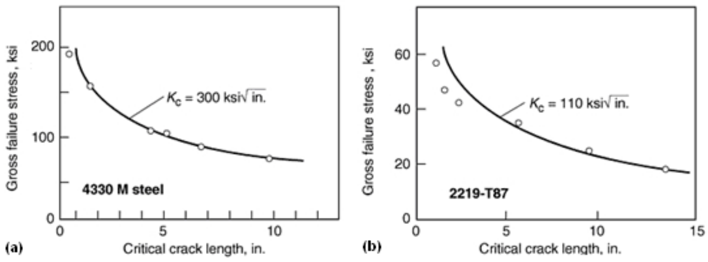

Figure 3.3: Influence of crack length on gross failure stress for centre-cracked plate. (a) Steel plate, 36 in. wide, 0.14 in. thick, room temperature, 4330 M steel, longitudinal direction. (b) Aluminum plate, 24 in. wide, 0.1 in. thick, room temperature, $2219 - T87$ aluminum alloy, longitudinal direction. ASM Metals Hand-Book Volume 19 - Fatigue And Fracture.

tion between flaw size and fracture stress, which can be significantly lower than yield strengths, depending on crack length and geometry (Fig.3.3). However, stable slow crack growth could occur even though accompanied by considerable plastic deformation. This phenomenon is the nonlinear J-integral concepts foundation, which can be used to predict the onset of stable slow crack growth and final instability under elastic-plastic conditions, as noted in Fig.3.2b. (See Appendix A for details).

3.2 Linear Elastic Fracture Mechanics(LEFM)

Linear Elastic Fracture Mechanics analysis [28] [29] [30] allows to establish the critical condition for the growth of flaws.
First of all it is necessary to examine the different modes of fracture: the crack surface displacements could happen in three different ways (Fig.3.4). Mode I is the 'tensile opening' mode, in which the crack faces separate in a direction normal to the plane of the crack and the corresponding displacements of the crack walls are symmetric with respect to the $x - z$ and the $x - y$ planes.
Mode II is the 'in-plane sliding' mode, in which the crack faces are mutually sheared in a direction normal to the plane of the crack and the corresponding displacements of the crack walls are symmetric with respect to the $x - z$ planes.

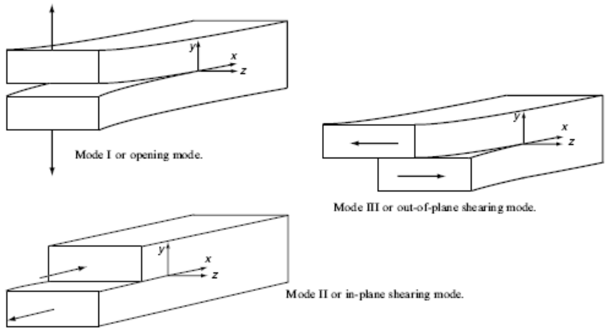

Figure 3.4: Basic modes of fracture.

Mode III is the 'tearing or anti-plane shear' mode, in which the crack faces are sheared parallel to the crack front and the displacements of the crack walls, in this case, are anti-symmetric with respect to the $x - y$ and $x - z$ planes. Irwin (1957), using the analytical methods of Westegaard (1939), quantified the near tip fields, for a linear elastic crack, in function of the stress intensity factor previously introduced. In this section, Irwin's work results are presented (Tab. 3.1- 3.2- 3.3) (see Appendix B for detailed mathematical derivation). The following equations are referred to Fig.3.5 and they are a simplification of more general relationship in elasticity and are subjected to the following restriction:

- Two dimensional stress state: plane stress or plane strain;
- Isotropic material;
- Quasi-static, isothermal deformation;
- Body forces are absent from the problem.

Mode I and Mode II are plane problem.
Mode I, Mode II and Mode III stress intensity factors are respectively defined by the following relationships:

$$
\begin{aligned}
K_I &= \lim_{r\to 0}\left\{\sqrt{32\pi r}\sigma_{yy}\ |_{\theta}= 0\right\}\\
K_{II} &= \lim_{r\to 0}\left\{\sqrt{32\pi r}\sigma_{xy}\ |_{\theta}= 0\right\}\\
K_{III} &= \lim_{r\to 0}\left\{\sqrt{32\pi r}\sigma_{yz}\ |_{\theta}= 0\right\}
\end{aligned}
\tag{3.9}
$$

	ModeI	ModeII
σ_{xx}	$\frac{K_I}{\sqrt{2\pi r}}\cos\left(\frac{\theta}{2}\right)$ $\left[1-\sin\left(\frac{\theta}{2}\right)\sin\left(\frac{3\theta}{2}\right)\right]$	$-\frac{K_{II}}{\sqrt{2\pi r}}\sin\left(\frac{\theta}{2}\right)$ $\left[2+\cos\left(\frac{\theta}{2}\right)\cos\left(\frac{3\theta}{2}\right)\right]$
σ_{yy}	$\frac{K_I}{\sqrt{2\pi r}}\cos\left(\frac{\theta}{2}\right)$ $\left[1+\sin\left(\frac{\theta}{2}\right)\sin\left(\frac{3\theta}{2}\right)\right]$	$\frac{K_{II}}{\sqrt{2\pi r}}\sin\left(\frac{\theta}{2}\right)$ $\cos\left(\frac{\theta}{2}\right)\cos\left(\frac{3\theta}{2}\right)$
τ_{xy}	$\frac{K_I}{\sqrt{2\pi r}}\cos\left(\frac{\theta}{2}\right)$ $\sin\left(\frac{\theta}{2}\right)\cos\left(\frac{3\theta}{2}\right)$	$\frac{K_{II}}{\sqrt{2\pi r}}\cos\left(\frac{\theta}{2}\right)$ $\left[1-\sin\left(\frac{\theta}{2}\right)\sin\left(\frac{3\theta}{2}\right)\right]$
σ_{zz}	0 (plane stress) $\nu(\sigma_{xx}+\sigma_{yy})$ (plane strain)	0 (plane stress) $\nu(\sigma_{xx}+\sigma_{yy})$ (plane strain)
τ_{xz},τ_{yz}	0	0

Table 3.1: Stress fields ahead a crack tip for ModeI and ModeII in linear, elastic, isotropic material; ν : Poisson's ratio.

	ModeI	ModeII
u_x	$\frac{K_I}{2\mu}\sqrt{\frac{r}{2\pi}}\cos\left(\frac{\theta}{2}\right)$ $\left[K-1+2\sin^2\left(\frac{\theta}{2}\right)\right]$	$\frac{K_{II}}{2\mu}\sqrt{\frac{r}{2\pi}}\sin\left(\frac{\theta}{2}\right)$ $\left[k+1+2\cos^2\left(\frac{\theta}{2}\right)\right]$
u_y	$\frac{K_I}{2\mu}\sqrt{\frac{r}{2\pi}}\sin\left(\frac{\theta}{2}\right)$ $\left[K+1-2\cos^2\left(\frac{\theta}{2}\right)\right]$	$-\frac{K_{II}}{2\mu}\sqrt{\frac{r}{2\pi}}\cos\left(\frac{\theta}{2}\right)$ $\left[k-1+2\sin^2\left(\frac{\theta}{2}\right)\right]$

Table 3.2: Displacements ahead a crack tip for ModeI and ModeII in linear, elastic, isotropic material. $k = 3-4\nu$ in plain strain conditions, $k = (3-\nu)(1+\nu)$ in plane stress conditions.

	ModeIII
τ_{xz}	- $\frac{K_{III}}{\sqrt{\frac{r}{2\pi}}}\sin\left(\frac{\theta}{2}\right)$
τ_{yz}	$\frac{K_{III}}{\sqrt{\frac{r}{2\pi}}}\cos\left(\frac{\theta}{2}\right)$
u_z	$\frac{K_{III}}{\mu}\sqrt{\frac{r}{2\pi}}\sin\left(\frac{\theta}{2}\right)$

Table 3.3: Non-zero stress and displacement components for Mode III in linear, elastic, isotropic material.

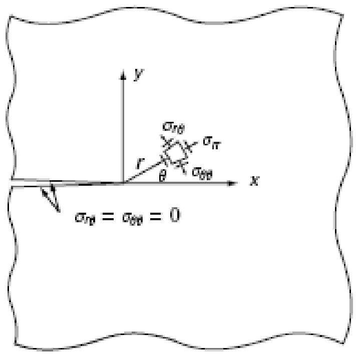

Figure 3.5: Definition of variables and coordinates.

It is useful to remember that in the practice, Mode I dominating in respect with other two modes and it has been experimentally determined for most common test specimen [31]. The stress intensity factor expresses near tip fields intensity under linear elastic conditions. The radial component and the angular component depend only on the spatial coordinates. These terms determine the distribution of the near tip fields. In LEFM, crack growth under monotonic, quasi-static loading conditions come true for values above a specific threshold represented by the critical value of the stress intensity factors, K_c. The value of K_c is a function of loading, chemical environment, material microstructure, temperature, strain-rate and stress state and is experimentally determined [30]. The critical value of stress intensity factor for Mode I, measured under plane strain conditions, is commonly referred as the 'fracture toughness', K_{Ic}, of the material at the particular test temperature. The corresponding fracture toughness values in the sliding and tearing modes are respectively designated as K_{IIc} and K_{IIIc}. Under cyclic loading conditions, the rising of crack growth from a preexisting flaw or defect may occur at stress intensity values highly below the quasi-static fracture toughness, and the crack growth is determined by the Paris law previously presented. The stress intensity factor approach to investigate fracture has a direct equivalence to the energy approach. For the general three-dimensional case, plane stress condition the relationship is expressed by:

$$\mathbf{G} = \frac{\mathbf{K_I^2}}{\mathbf{E'}} + \frac{\mathbf{K_{II}^2}}{\mathbf{E'}} + \frac{\mathbf{K_{III}^2}}{\mathbf{2\mu}} \tag{3.10}$$

where

- $E' = E$ for plane stress conditions;
- $E' = \frac{E}{1-\nu^2}$ for plain stress conditions;
- μ: shear modulus.

3.3 Elasto-Plastic Fracture Mechanics(EPFM)

While LEFM describes such materials that present non-linear deformation confined to a small region surrounding the crack tip, in many materials this condition is not obtainable, so an alternative fracture mechanics model is required. EPFM applies to material that show time-independent non-linear behavior (i.e., plastic deformation) the 'J-integral' approach, proposed by Rice in 1968 [31].
Let's start considering a cracked body subjected to a monotonic load, and assuming with reference to Fig.3.6 that:

- traction, T, is independent of crack size;
- the crack faces are traction-free.

So, the line integral J along any contour Γ which encircles the crack tip is given by:

$$\mathbf{J} = \int_{\mathbf{\Gamma}} \left(\mathbf{wdy} - \frac{\mathbf{T\delta u}}{\delta \mathbf{x}} \mathbf{ds} \right) \tag{3.11}$$

where u is the displacement vector, y is the distance along the direction normal to the plane of the crack, s is the arc of length along the contour, T is the traction vector and w is the strain energy density of the material. The stresses S_{ij} are related to w by the following relation:

$$\mathbf{S_{ij}} = \frac{\delta \mathbf{w}}{\delta \varepsilon_{\mathbf{ij}}} \tag{3.12}$$

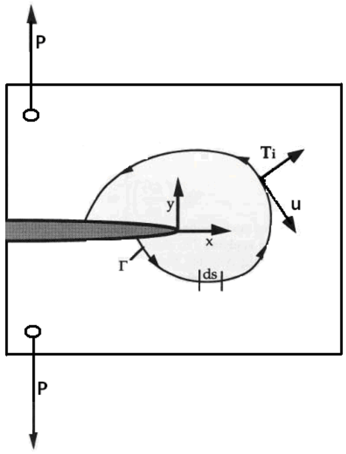

Figure 3.6: 'a' contour around a crack tip and the nomenclature used in the definition of the J-integral.

Rice also showed that (for non linear elastic solid) J give evidence of potential energy rate of change, with respect to crack growth, and that J is comparable to the energy release rate G (for a linear elastic material) by means of the following relation:

$$\mathbf{J} = \mathbf{G} \approx -\frac{\delta(\mathbf{PE})}{\delta \mathbf{a}} \tag{3.13}$$

where P is the applied load, and E is the Young's modulus. The J-integral provides a measure of the strength of singular fields in non-linear fracture. However, Hutchinson (1983) formalized a list of requirements for the use of J-integral [32]:

- The deformation theory of plasticity must be an adequate model of the small-strain behavior of real elastic-plastic materials under the monotonic loads being considered.
- The region in which finite strain effects dominate and the region in which microscopic failure processes occur must each be contained well within the region of the small-strain solution dominated by the singular fields.(See Appendix C for details)

3.4 References

ASM Metals Hand-Book Volume 19 - Fatigue And Fracture.

Fracture and Fatigue; Fracture Mechanics; Anderson (2Nd Ed).

Fatigue of Structures and Materials; Jaap Schijve.

Fatigue of Materials; S. Suresh.

Fracture and Fatigue Control in Structures (2Nd Ed); John M. Barsom, Stanlet T. Rolfe.

Chapter 4

Fatigue Tensile Machine Design

In Chapter 1, the 'Stress Life Test' and the 'Strain Life Test' have been introduced to show how to characterize material fatigue behavior. In Chapter 2 and 3, the instruments to perform an analytical evaluation of material fatigue behavior has been introduced, giving evidence that also the analytical approach requires material parameters inputs obtainable from both tensile and fatigue tests.
Consequently, in this chapter, the design of a customized fatigue test machine will be described and its realization will allow us to perform both experimental and analytical fatigue life evaluation.
The goal of this design is to obtain:

- A fatigue test machine that result cost effective;
- A fatigue test machine having also small dimensions.

For this reasons we chose an electro-mechanical solution instead of a servo-hydraulic one.
For biomedical applications, a good choice is to test specimen which dimension are comparable with endosurgical devices: so the first step is to design a fatigue tensile machine specific for wire specimens with a prototypization of a customized solution for radial stents test which will be further realized.

Fatigue test is composed by two phases:

- Phase I: specimen pretensioning;
- Phase II: application of alternate cyclic strain.

Following the described concepts, the machine has been designed in two distinct 'Parts' which allow to fit the two experimental Phases:

- Part I: implementing the initial strain conditions;
- Part II: implementing the cyclic variation of initial conditions.

4.1 Part I: Applying Initial Strain Conditions

Part I will impose the initial applied strain conditions on specimen by implementing the mechanical morse principle.
With respect to fig. 4.1 Part I acts as follow: an electric actuator (1) moves a pinion (5) which is coupled with a customized crown (6). The crown (6) is fixed to a workbench (3), maintaining rotational degrees of freedom resulting from customized design of supports (4) − (7).
The crown (6) is characterized at its distal extremity by a screw which is coupled with a nut (8) which moves horizontally by dragging in a empty support (10).
The nut support (10) is directly fixed to the workbench (3).
A bush (9) is interposed between the nut (8) and its support (10) to reduce disruptive phenomena.
A load cell (11) is the link between the nut (8) and a customized grasping system (12) which ensure the specimen stability.
The specimen is fixed at its end with an identical grasping system which is mounted on a constrained support as shown in next section.
The solution presented allow to imposes the initial condition controlling both stress and strain.
To ensure a specific control on initial condition implementation a stepper actuator has been chosen.

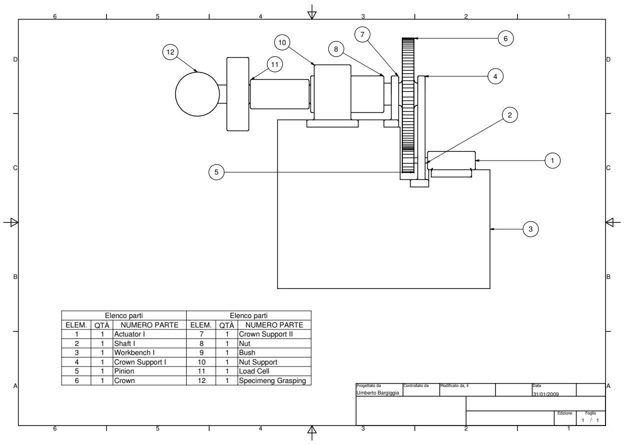

Figure 4.1: Part I: solution to implement the initial strain conditions.

4.2 Part II: Applying the Cyclic Variation of Initial Conditions

Part II will be presented with reference to figure 4.2.
Fatigue test is performed by the action of a cam (6) on a shifting piston (10).
To avoid displacement of the shifting piston (10), during Phase I load, a final constrain (11) has been realized.
The cam (6) rotes for the action of a second electrical actuator (8).
With this solution, the maximum specimen deformation is equal to cam maximum eccentricity (6).
Different cams are required to perform different fatigue tests.
The instantaneous stress evaluation (static and dynamic) will be the result of the load cell output. The shifting piston (10) moves on two guides (12). On the guides bottom two springs (4) are fixed by a dedicated support (5) to ensure shifting piston elastic return, inducing no effects on specimen.
To face the high number of cycles usually required for a fatigue test, a DC brushless actuator has been chosen.
In figure 4.3 , the fatigue machine assembly is shown.

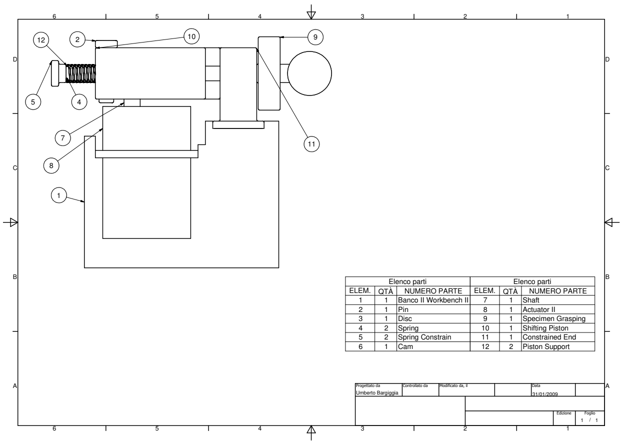

Figure 4.2: Part II: solution to implement the cyclic variation of initial conditions.

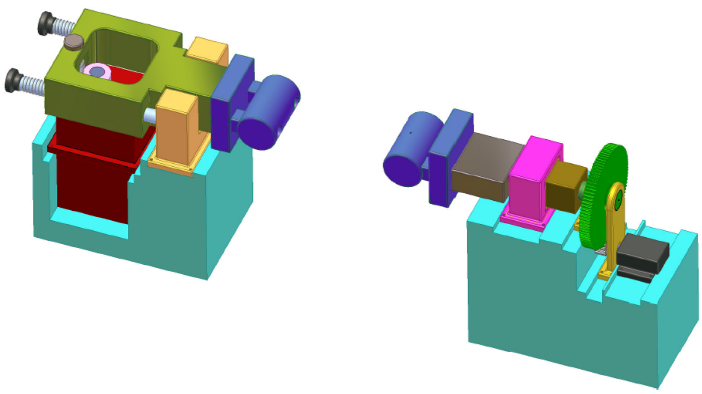

Figure 4.3: Fatigue machine final assembly.

4.3 Fatigue Machine Components Design

In the following section the design of each component described in 'Part I' and 'Part II' will be presented, and their realization may ensure the fulfillment with the specific requirements of a fatigue test. Our goal is to investigate Nitinol (the most common shape memory alloy used for stents realization) fatigue behavior, so the analytical calculation of structural components starts from Nitinol mechanical properties.

4.3.1 Nitinol Specimen Properties

Ideally a Nitinol specimen wire may have the following dimensions:

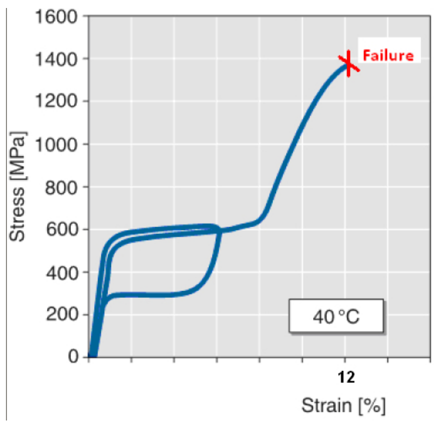

Figure 4.4: Nitinol properies for a $1,5\ mm$ specimen diameter.

- Length: $l = 100\ mm$;
- Diameter: $D = 0.25$ to $1.5\ mm$;

Nitinol mechanical behavior is the consequence of its chemical composition which could be in both austenitic or martensitic phase:

- Austenitic Young's Modulus : $E_{aust} = 45 - 85\ GPa$;
- Martensitic Young's Modulus: $E_{mart} = 24 - 45\ GPa$.

The Young's Modulus range is a consequence of Nitinol percentile composition. An investigation conducted by A. Pelton [77] show the following Nitinol properties as shown in figure 4.4:

- Nitinol could be subjected to $0 - 12$ percent of uniaxial deformation;
- Between 0° to 60° Nitinol stress-strain curve shows approximatively a linear relation in each step of the hysteresis loop;
- Between 0° to 100° no appreciable plastic strain accumulation is observed at the end of the first stress-strain cycle ($\varepsilon_{res} = 1\%$).

In figure 4.4 it is possible to note that 12% in strain corresponde to the static failure stress σ_f of about 1400 MPa at 40° (data are referred

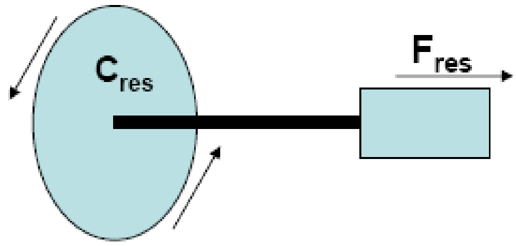

Figure 4.5: Static load evaluation.

to 50.8% Ni-Ti specimen with 1.5 mm diameter).
So the applied load, F is:

$$\mathbf{F} = \sigma \cdot \mathbf{A} \approx \mathbf{2473}\ N \tag{4.1}$$

where A is the specimen section area considering an 1.5 mm diameter. This value is the resisting load that the electrical actuators must face to allows specimen deformation.

4.3.2 Electric Actuator I

To implement 'Part I', a stepper actuator has been chosen because it allows to closely control the angular rotation.
As previously mentioned, we know that the resisting load ,F_{res}, is 2473 N. To design a machine which allows to test different materials and which ensures a safety margin, we consider $F_{res} = 5\ \ kN$.
To establish actuator power, two distinct analysis has to be implemented:

- Static loads evaluation;
- Dynamic loads evaluation.

Static Loads Evaluation

The static load evaluation allow to investigate the minimum torque wrench that the stepper actuator must check for specimen deformation.
The force balance is represented schematically in figure 4.5. A com-

plete evaluation of all forces (i.e. frictions) and the inevitable load loss for gear wheel is embodied in the approximation of 5 kN for the resisting force.
So, the static evaluation comes from a work balance during one cycle:

$$\mathbf{C_{res}} \cdot \mathbf{2}\pi = \mathbf{F_{res}} \cdot \text{screw step} \tag{4.2}$$

where:

- C_{res}: static torque needed to maintain the imposed deformation;
- F_{res}: load for specimen deformation (5 kN);
- screw step $= 1\ mm/pr$ (design parameter).

This balance allows us to evaluate the static torque as follow:

$$\mathbf{C_{res}} = \frac{\mathbf{F_{res}} \cdot \text{ screw step}}{\mathbf{2}\pi} = \mathbf{0.8}\ Nm \tag{4.3}$$

It's usual in the practice to consider a 30% of increment in the torque evaluation as a safety factor, so:

$$\mathbf{C_{res}} = \mathbf{1.04}\ Nm \tag{4.4}$$

Dynamic loads evaluation

A dynamic investigation of actuator power is a function of load and time.
To implement 'Phase I', there is no need to be fast and a reasonable cycle time could be fixed in 1 minute.
We will define this period t_a :

$$\mathbf{t_a} = \mathbf{60}\ s \tag{4.5}$$

If trapezoidal speed profile (a ramp input) is considered, the speed-time (qualitative) plot result as shown in figure 4.6. So, the space-time and the acceleration-time plots (qualitative) are given as shown in figure 4.7:
The medium value of linear speed, v_m could be calculated as:

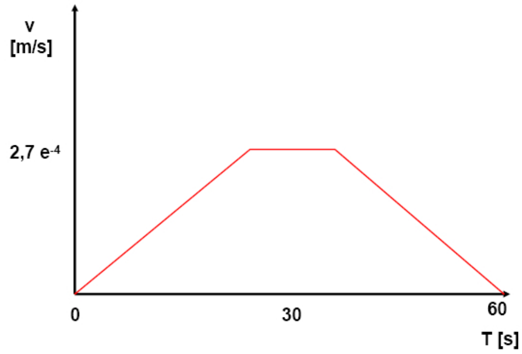

Figure 4.6: Speed-Time plot for trapezoidal speed profile.

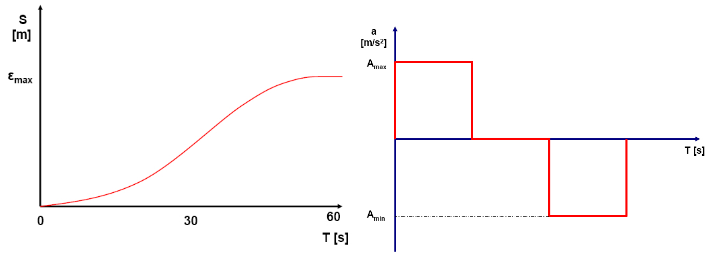

Figure 4.7: Space-Time and Acceleration-Time plot caming from trapezoidal speed profile.

$$\mathbf{v_m} = \frac{\varepsilon_{\mathbf{max}}}{\mathbf{t_a}} = \frac{\mathbf{0.012}\ m}{\mathbf{60}\ s} = \mathbf{2.0 \cdot 10^{-4}}\ m/s \tag{4.6}$$

So the maximum speed value, v_{max} could be found:

$$\begin{aligned} v_m &= \frac{1}{t_a}\int_0^{t_a} v(t)dt = \frac{5}{8}v_{max} \\ v_{max} &= 3.2 \cdot 10^{-4}\ m/s \end{aligned} \tag{4.7}$$

This value of v_{max} represents the minimum speed value to obtain the presupposed work cycle.

If we fix the ratio between the crown and the pinion radii as a specific design parameter, the angular actuator speed could be deduced:

$$\frac{\mathbf{R_c}}{\mathbf{R_p}} = \mathbf{5} \tag{4.8}$$

where:

- R_c : crown radius;
- R_p : pinion radius.

Remembering that screw step = 1 mm/pr , it has approximately to complete ten round to obtain the required deformation. The motion transmission is directly transmissed by the crown and the pinion, so the pinion has to do 50 round. By consequence, the angular speed (ω_{min}), which is the minimum for work cycle fulfillment, is given:

$$\omega_{\mathbf{min}} = \frac{\mathbf{50}\text{ round}}{\mathbf{60s}} = \mathbf{5.23}\ rad/s \tag{4.9}$$

For dynamic evaluation, the actuator power comes from a power balance:

$$\begin{aligned} P &= F_{res}v_{max} = C_{res_D}\omega_{min} \\ C_{res_D} &= \frac{F_{res}v_{max}}{\omega_{min}} = 0.3\ Nm \end{aligned} \tag{4.10}$$

The value of reference is the static one.
There is a large choice of stepper actuators with the described characteristic, the one we chose and its relative cost is presented in section 4.6.

4.3.3 Crown and Pinion

In the following section, a standard procedure to design coupled gear wheels is presented.

Gear Wheel Parameters Identification

The following consideration allow to evaluate the crown and the pinion geometrical parameters.
As shown in figure 4.8 , the main parameters are introduced:

- Head Circle: upper pawl limit;
- Primitive Circle: contact circle between pinion and crown;
- Bottom circle: bottom pawl limit;
- Step (s): primitive circle arch length between two consecutive pawl axes;

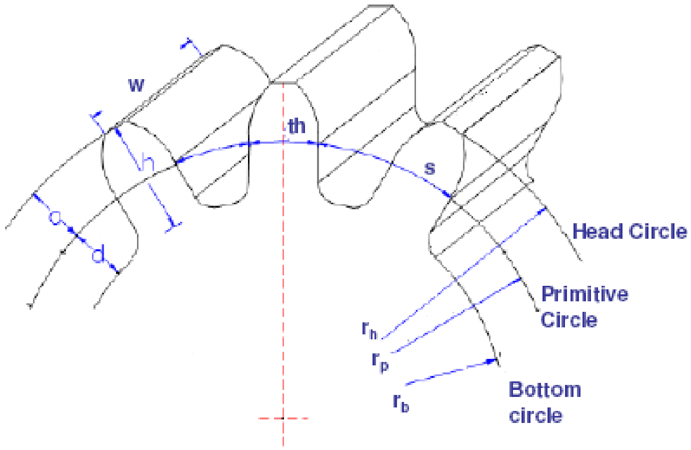

Figure 4.8: Gear wheel parameters identification.

- thickness (th): primitive circle arch length defined by a single pawl;
- width (w): gear wheel width;
- Height (h): difference between head circle radius and bottom circle radius;
- Addendum (a): head pawl height;
- Dedendum (d): pawl base height.

The following relation is suitable for every gear wheel:

$$\mathbf{s} = \frac{\pi \mathbf{d_p}}{\mathbf{z}} \tag{4.11}$$

where:

- d_p: primitive circle diameter;
- z: number of pawls.

The step indicator is an irrational number, so it's usual for a gear wheel to calculate the so called 'modulus number (m)', defined as:

$$\mathbf{m} = \frac{\mathbf{d_p}}{\mathbf{z}} \; [mm] \tag{4.12}$$

Two coupled gear wheels must check the same modulus value.
Finally, the transmission rate parameter i, which is the amplifier or reduction angular speed coefficient of two coupled gear wheels, is presented:

$$\mathbf{i} = \frac{\omega_\mathbf{c}}{\omega_\mathbf{p}} = \frac{\mathbf{d_c}}{\mathbf{d_p}} \tag{4.13}$$

where:

- ω_c: angular crown speed;
- ω_p: angular pinion speed;
- d_c: crown diameter;
- d_p: pinion diameter.

The gear wheel pawls have specific profiles which allow to maintain the contact during all the motion. The pawls of the motive gear wheel induce a force S on the second gear wheel having an angular direction α. In the practice α is assumed as a constant of 20°.
The minimum pawls number is a function of α and transmission rate as shown in the following table:

Transmission Rate	1	1,5	2	2,5	3	3,5	4	6	8 to 12
Minimum Number of Pawls z_m for $\alpha = 20°$	13	14	15	15	16	16	16	16	17

Table 4.1: Minimum pawls number as function of α and transmission rate.

Remembering that $d_c/d_p = 5$ we obtain:

$$\mathbf{z_m = 16} \tag{4.14}$$

In the practice, the pinion pawls number (z_p) and the crown ones (z_c) are chosen as a couple of prime number for the following reasons:

- It ensure that two any pawls will contact each self every $Z_c \cdot Z_p$ round, ensuring the relative contact between every gear wheel pawl;

- It ensure a uniform wear of pawls.

Considering an hypothetical pinion radius of 15 mm we chose $Z_p = 19$ and $z_m = 95$ which give $m = 1.579\ mm$. The modulus values have unified values to ensure components adaptability:

- From $0.3 < m \geq 1\ mm$ of modulus values the increment is $0.1\ mm$;

- From $1 < m \geq 4\ mm$ of modulus values the increment is $0.25\ mm$;

- From $4 < m \geq 7\ mm$ of modulus values the increment is $0.5\ mm$;

- From $7 < m \geq 16\ mm$ of modulus values the increment is $1\ mm$;

- From $16 < m \geq 24\ mm$ of modulus values the increment is $2\ mm$;

- From $24 < m \geq 45\ mm$ of modulus values the increment is $3\ mm$;

- From $45 < m \geq 75\ mm$ of modulus values the increment is $5\ mm$.

In the practice the m value is the unified value which is immediately major then the one calculated, so $m = 1.75\ mm$.
The gear wheels profile has standard shapes, the most common is the circle involute arc profile.

Parameters Calculation

Now that all parameters are defined, their calculation is presented in this section. Once the modulus m is known, all the other parameters could be formalized staring from it as shown:

$$
\begin{aligned}
s &= \pi m = 5.5\ mm \\
a &= m = 1.75\ mm \\
d &= 1.25m = 2,2\ mm \\
h &= a + d = 2.25 \cdot m = 4\ mm \\
r_{head} &= r_p + a = r_p + m = 16.75\ mm \ \text{ pinion ; } 76.75\ mm \ \text{ crown} \\
th &= s/2 = 2.75\ mm
\end{aligned}
\tag{4.15}
$$

In the practice gear wheel width is usually fixed at $10 \cdot m$, so $w =$ 17.5 mm .
Now that gear wheels design is done, one has to verify both static and dynamic components endurance as a consequence of the chosen material for realization (steel).

Static Gear Wheels Endurance Calculation

The main static strain is a result of bending which reaches its maximum value in correspondence of the head circle.
Bending endurance is calculated from Lewis formula, which is based on the following hypothesis:

- Applied load concentrated on the pawl summit;
- Only one couple of pawls in traction;
- No radial forces acting;
- No friction.

Pawl profile is usually as shown in figure 4.9 in which we could define:

- t: thickness;
- h: height;
- w: width (orthogonally with respect to the figure);

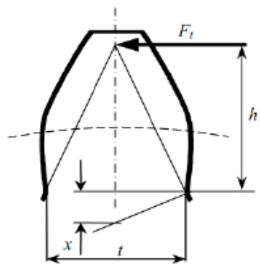

Figure 4.9: Pawl profile.

- F_t: concentrated applied load.

Maximum stress is reached on the pawl bottom and is given by:

$$\sigma = \frac{\mathbf{F_t ht}}{\mathbf{2wt^3/12}} = \frac{\mathbf{F_t 6h}}{\mathbf{wt^2}} \tag{4.16}$$

Height and thickness are modulus depending, so the preceding equation becomes:

$$\sigma = \frac{\mathbf{F_t}}{\mathbf{wmY}} \tag{4.17}$$

where Y is Lewis shape factor (dimensionless) depending on pawl shape.
Y values are tabulated for unified gear wheels as a function of number of pawls, and for our design $Y = 1.314$ (pinion) and $Y = 0.435$ (crown). In section 4.3.2 $C_{res} = 1.04Nm$ has been calculated and so F_t is:

$$\begin{aligned} F_t\text{pinion} &= \frac{C_{res}}{r_{head}\text{ (pinion)}} = 62.1\ N \\ F_t\text{crown} &= \frac{C_{res}}{r_{head}\text{ (crown)}} = 13.5\ N \end{aligned} \tag{4.18}$$

A safety value for F_t is assumed as 80 N . So the stress produced will be:

$$\begin{aligned} \sigma_{pinion} &= 2\ MPa \\ \sigma_{crown} &= 6.2\ MPa \end{aligned} \tag{4.19}$$

These values are abundantly below steel yield stress.

Dynamic Gear Wheels Endurance Calculation

Pawls surfaces are the gear wheel parts which are most affected by fatigue deterioration caused by stresses mutually induced by pawl surfaces contact.
Deterioration could be the result of essentially three aspects:

- Abrasion : caused by material particles interposed between pawls surfaces;
- Surfaces rifling : induced by a non sufficient lubrication;
- Pitting : due to high local stresses.

Mutual stresses could be calculated with Hertz theory, which allows to establish the contact pressure (p_{max}) between two constrained cylinder, and they are given by the following relation:

$$\mathbf{p_{max}} = \sqrt{\frac{\mathbf{\Delta q}}{\pi\rho}} = \sqrt{\frac{\mathbf{q\,(1/R_1 + 1/R_2)}}{\pi\left(\frac{\mathbf{1-\nu_1^2}}{\mathbf{E_1}} + \frac{\mathbf{1-\nu_2^2}}{\mathbf{E_2}}\right)}} \tag{4.20}$$

where:

- q : load for unit length which is applied on pawl surfaces;
- ν_1, ν_2 and E_1, E_2 : material elastic constants (steel);
- R_1, R_2 : cylinder diameters.

With reference to gear wheels, the following parameters must be introduced:

- b : pawl surface width;
- q : $F/b = F_t/(b \cdot cos\alpha)$;
- $R_{1,2} = r_{1,2}$: instantaneous values of pinion and crown pawls profile at the contact point.
- d_{pp} : pinion primitive diameter;
- d_{pc} : crown primitive diameter.

So the following relation could be written:

$$\mathbf{r_1} = \frac{\mathbf{d_{pp}} \sin\alpha}{\mathbf{2}} \; ; \; \mathbf{r_2} = \frac{\mathbf{d_{pc}} \sin\alpha}{\mathbf{2}} \tag{4.21}$$

Defining the elastic coefficient C as follow:

$$\mathbf{c} = \sqrt{\frac{\frac{\mathbf{1}}{\pi}}{\left(\frac{\mathbf{1}-\nu_\mathbf{1}^\mathbf{2}}{\mathbf{E_1}} + \frac{\mathbf{1}-\nu_\mathbf{2}^\mathbf{2}}{\mathbf{E_2}}\right)}} \tag{4.22}$$

by substitution in equation 4.20 and considering steel as building material, one has:

$$\mathbf{p_{max}} = \mathbf{c}\sqrt{\frac{\mathbf{F_t}}{\mathbf{bd_{pc}I}}} = \mathbf{3.4}\ MPa \tag{4.23}$$

The given values have to be corrected in the practice by differents safety factors:

- K_v : it depends by linear speed, v, measured on primitive circles. It could be approximated with the following relation $\rightarrow K_v = 6.1/(6.1+v)$;
- K_0 : it depends on irregularity during actuator performances ($K_0 = 1.00$ to 2.25);
- K_m it depends by components realization and precision during components coupling ($K_m = 1.00$ to 2.25).

We chose the worst case giving rise at:

$$\begin{aligned} v &= \omega r = 0.08\ m/s \text{ approximatively} \\ \sigma &= \frac{F_t K_0 K_m}{bmYK_v} = 31.6\ MPa \\ p_{max} &= c\sqrt{\frac{F_t K_0 K_m}{bd_{pc} I K_v}} \approx 7.15\ MPa \end{aligned} \tag{4.24}$$

As a result of the preceding evaluation the dimensions chosen for gear wheels ensure a safety test implementation.
In the following figures, the pinion and crown drowings are presented:

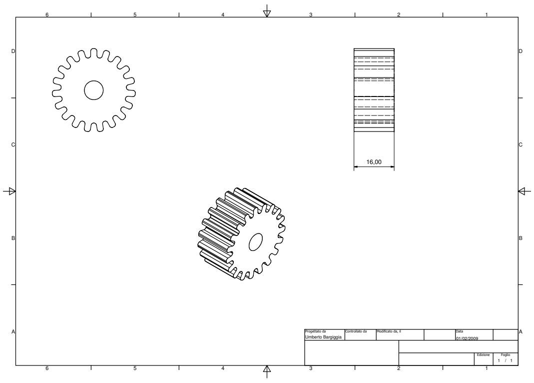

Figure 4.10: Pinion design.

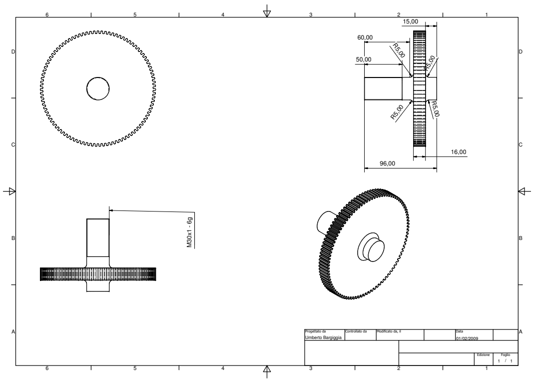

Figure 4.11: Crown design.

Efficiency Evaluation

As a consequence of friction due to pawl contact there is a lost in actuator produced power. For a couple of gear wheels it is given by:

$$\nu = \mathbf{1} - \mathbf{f}\pi \left(\frac{\mathbf{1}}{\mathbf{z_p}} + \frac{\mathbf{1}}{\mathbf{z_c}} \right) \tag{4.25}$$

For gear wheel with parallel axis usually $\nu = 0.95$; 0.98.
This power loss will widely overcame by the chosen actuator.

4.3.4 Actuator I Shaft Verify

In this section, a force analysis acting on actuator I shaft will be presented to be sure that its dimension allows to tolerate the resulting forces coming from both tensile and fatigue test.

In design approach, the shaft will be considered as a cantilever beam with a constant section. The main forces acting on the shaft are torsional and flexional. Power transmission is governed by torque moment developed by the stepper actuator ($C_{res} = 1.04\ Nm$), but the shaft will be subjected to bending given by pinion mass as shown by the following equations:

$$\begin{aligned} V_{pinion} &= \pi r^2 \cdot width_{pinion} = 1.2 \cdot 10^{-5}\ m^3 \\ m_{pinion} &= V_{pinion} \cdot \rho_{pinion} \approx 0.1\ kg \end{aligned} \tag{4.26}$$

where:

- V_{pinion}: pinion volume assuming that the pinion has a circle base with radius equal to head radius;
- m_{pinion}: pinion mass for a gear wheel realized with steel;
- ρ_{pinion}: steel density (7850 kg/m^3).

Considering the other components designed, the maximum length required for the shaft (outside the actuator) is $l_{shaft} = 0.04\ m$, so bending (B_{pinion} could be determined assuming pinion mass applied on distal pinion end:

$$\mathbf{B_{pinion}} = \mathbf{m_{pinion}} \cdot \mathbf{g} \cdot \mathbf{l_{shaft}} = \mathbf{0.0392}\ Nm\ ;\ \ g = 9.8\ m/s^2 \tag{4.27}$$

This bending value is below steel tolerance.

As shown in figure 4.12 , the stresses acting in any point of shaft lateral surface will be calculated assuming no axial forces acting:

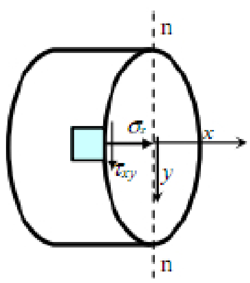

Figure 4.12: Stresses acting in any point of shaft lateral surface.

$$\begin{aligned} \sigma_x &= 32B_{pinion}/\pi d^3 \\ \tau_{xy} &= 16T/\pi d^3 \end{aligned} \tag{4.28}$$

For ductile materials there is a relationship between the calculated stresses and the equivalent stress as calculated respectively by Tresca and Von Mises:

$$\begin{aligned} \sigma_e &= \sigma_1 - \sigma_2 = \sqrt{\sigma_x^2 + 4\tau_{xy}^2} \\ \sigma_e &= \sqrt{\sigma_1^2 - \sigma_1^2 - \sigma_1\sigma_2 + \sigma_2^2} \end{aligned} \tag{4.29}$$

where the principal stresses (σ_1, σ_2) are given by:

$$\boldsymbol{\sigma_1, \sigma_2 = \frac{\sigma_x}{2} \pm \sqrt{\left(\frac{\sigma_x}{2}\right)^2 + \tau_{xy}^2}} \tag{4.30}$$

If Tresca and Von Mises equations are rewritten as a function of geometrical shaft parameters, it allows us to evaluate shaft minimum diameter to ensure both static and dynamic endurance:

$$\begin{aligned} \sigma_e &= \frac{4}{\pi d^3}\sqrt{(8B_{pinion})^2 + (8C_{res})^2} \\ \sigma_e &= \frac{4}{\pi d^3}\sqrt{(8B_{pinion})^2 + (48C_{res})^2} \end{aligned} \tag{4.31}$$

By substitution of equivalent stress (σ_e) with steel yield stress ($\sigma_y = 200\ MPa$), shaft diameter is given:

$$\begin{aligned} d_{Tresca} &= \sqrt[3]{\frac{32}{\pi\sigma_y}\sqrt{B_{pinion}^2 + C_{res}^2}} \approx 0.004\ m \\ d_{vonMises} &= \sqrt[3]{\frac{16}{\pi\sigma_y}\sqrt{4B_{pinion}^2 + 3C_{res}^2}} \approx 0.004\ m \end{aligned} \tag{4.32}$$

In the practice the yield stress are multiplied for a safety factor $n = 0.25$ giving a final shaft diameter value of $d \approx 6\ mm$.
The chosen actuator which has 7.5 mm diameter widely check the calculated value.

4.3.5 Screw-Nut Motion Solution

In this section the screw-nut threading will be dimensioned to ensure fulfillment with acting forces to perform a fatigue test.
As shown in figure 4.13, the following parameters could be defined:

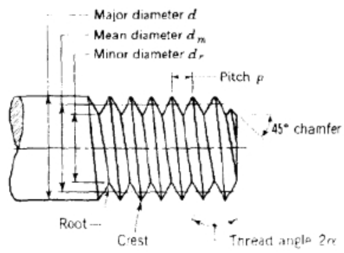

Figure 4.13: Screw-Nut parameters.

- p: defined as step it is the distance between two consecutive threads;
- d: major screw diameter;
- d_r: minor screw diameter;
- d_m: medium screw diameter.

The following data are design fixed parameters:

- $d = 0.03\ m$;
- $d_r = 0.029\ m$;
- material: steel ($E = 210\ GPa$; $\sigma_y = 200\ MPa$).

In the practice, the resisting screw section in traction condition is approximated with the section of a cylinder operating in the same section, which diameter (d_t) is so determined:

$$\mathbf{d_t = \frac{d + d_r}{2}} \tag{4.33}$$

More easily a 0.9 factor could be introduced for the hypothetical cylinder diameter.
Threading must ensure that both yielding and tear will not happen. As shown in figure 4.14 the parameter which ensure the safety condition is the screw threated length ($h = pn$ with n number of threats). The h value ensuring that no tear will occur is given by imposing that

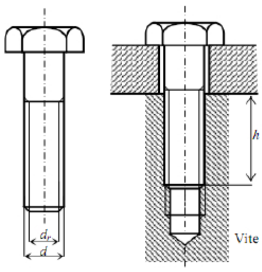

Figure 4.14: h: the screw threated length.

it may happen for the same amount of stress which cause screw yielding in pure tension (in longitudinal direction) condition.
The resisting section (S) is so determined:

$$\mathbf{S = 0.75\pi d_r h}\ [m^2] \tag{4.34}$$

Assuming the following load condition:

- Applied load, F, uniformly distributed on h;
- Threats may fail only in correspondence of d_r.

The shear stress could be approximated as follow:

$$\tau = \frac{\mathbf{F}}{\mathbf{0.75\pi d_r h}} = \frac{\mathbf{0.424F}}{\mathbf{d_r h}} \tag{4.35}$$

The h value could be calculated assuming that the force needed to tear the threats (F_t) is equal to the forces which causes a cylinder with $0.9d$ ($A_t istherelativearea$) yielding (F_s) as previously discussed, so:

$$\mathbf{F_s} = \sigma_\mathbf{y}\mathbf{A_t} \approx \sigma_\mathbf{y}\frac{\pi\,(\mathbf{0.9}\ \mathrm{d}\ )^\mathbf{2}}{\mathbf{4}} \approx \mathbf{114,5}\ kN \tag{4.36}$$

For practical application the yielding shear stress (τ_s) could be calculated as:

$$\tau_\mathbf{s} \approx \mathbf{0.577}\sigma_\mathbf{s} \tag{4.37}$$

So F_t could be calculated from equation 4.35, where F is substituted with F_t and τ with τ_s, so one has:

$$\mathbf{F_t} = \mathbf{0.577}\sigma_\mathbf{y}\pi\mathbf{d}\cdot\mathbf{0.75h} \tag{4.38}$$

Comparing equations 4.36 and 4.38, h is given:

$$\mathbf{h = 0.47d} \tag{4.39}$$

Usually a safety factor is introduced, and for practical applications it is common to consider the following relation:

$$\mathbf{h = 0.875d = 0.002625}\ m \tag{4.40}$$

Finally, the tear force F_t could be calculated and compared with the forces acting during machine life:

$$\mathbf{F_t = 0.577\sigma_y\pi d0.75h \approx 214}\ kN \tag{4.41}$$

The given F_t is widely above the forces acting during fatigue life investigation.

4.3.6 Load Cell

There are many differents load cell on the market; a 'DsEurope Load Cell, S series, model 560 QT' has been chosen for both the technical characteristic and comfortable price.
The load cell shape and the fixing behaviour are shown in figure 4.15.

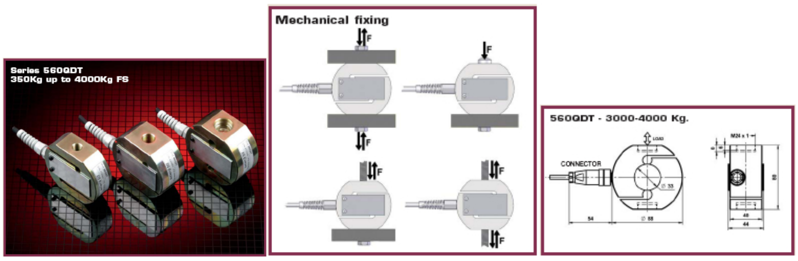

Figure 4.15: Load cell shape and fixing mechanism.

The load cell main properties are presented in figure 4.16 taken from load cell user handbook.
For the aquisition and elaboration of load cell output data a dedicated program (TestWorks v4.11) will be used.

DESCRIPTION:
Series 560QDT load cells are shear type load cells made with high strength steel for measuring ranges from 350 Kg up to 4000 Kg.
Series 560QDT has a full Wheatstone bridge with strain gauges that grants high thermal stability and reliability.
It is possible to purchase series 560QDT with mV/V not amplified output and with built-in analog output that allow high resolution and high protection against electrical noise (electronics is mechanically and electrically shielded by load cell metal frame and it is CE/EMC certified).

APPLICATIONS:
Series 560QDT is fit for many industrial and research applications because of its low profile, ruggedness and good price such as: automation, industrial weighing, test machines, textile machines, tanks, cranes, winches, lifts, vehicle test machines, machine tools, marble machines, ceramic machines, vehicles, medical scales, packaging machines, converting machines, presses etc.

TECHNICAL SPECIFICATIONS:

Measuring ranges (tension and compression):	0 to 350 - 400 - 500 - 1000 - 2000 - 3000 - 4000Kg FS.
Sensitivity:	2mV/V typical.
Non linearity:	± ≤ 0,1%FS.
Repeatability error:	± ≤ 0,03%FS.
Return to zero error::	± ≤ 0,03%FS.
Zero thermal drift error:	± ≤ 0,03%FS/°C.
Zero unbalance:	2%FS max.
Wheatstone bridge impedance:	350 Ohm.
Power supply:	10Vdc/ac, maximum 20Vdc/ac (2mV/V typ. output)
Maximum overload:	150%FS, Breackage 300%FS (load aligned on measuring axis).
Working temperature range:	-15°C up to +75°C.
Environmental protection:	IP65.
Electrical connection:	2m long shielded cable or connector.

Figure 4.16: Load cell specifications.

4.3.7 Specimen Grasping

In wire test the principal problem could be specimen failure induced not by load action but as a consequence of grasping constrain, so specimen grasping has been one of the hardest aspect encountered in fatigue machine design.
A customized solution will be presented in the following section to ensure firstly the specimen axiality to be maintained and secondly an efficient grasping during fatigue test (Figure 4.17).
This solution will allow to wrap the the specimen around the cylindric grasping part, reducing the probability of wire sliding.

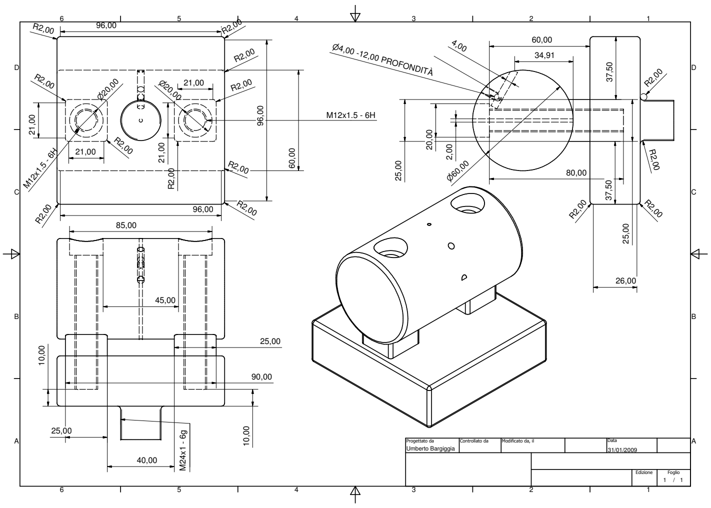

Figure 4.17: Specimen grasping mechanism.

4.3.8 Actuator II

Actuator II is the one which allows to conduce fatigue test and to implement our purposes a DC brushless actuator has been chosen.
As for actuator I we need to evaluate the applied torque to ensure specimen deformation. In section 4.3.2, the static torque value has been calculated (C_{res} = 1.04 Nm). This value is valid also for actuator II and it ensure the DC brushless ability to induce specimen maximum deformation.
We would like to be able to perform both Low Cycle and High Cycle fatigue test, so we assume a number of cycle to failure of about 10^6 cycles. We chose a DC brushless actuator which could work between 80 to 4000 round per minute (considering the maximum speed, the test must continue for ≈ 42 hours), so the power require is given by:

$$\mathbf{P_{II}} = \mathbf{C_{res}} \cdot \omega_{\mathbf{max}} \approx \mathbf{450}\ W \tag{4.42}$$

In the practice a safety factor of 40% is considered compared to theoretical calculation for actuator which has to work for long time, so the effective power required is:

$$\mathbf{P_{IIeff}} \approx \mathbf{630}\ W \tag{4.43}$$

The chosen DC brushless will be presented in section 4.6

4.3.9 Cam Design

The DC brushless actuator chosen actuator II has also a transmission reduction $1:5$.
The slow shaft angular speed could vary between 16 to 800 round per minute. Considering the maximum angular speed as the regime angular speed ($\omega_r eg$), one has:

$$\omega_{\mathbf{reg}} = \mathbf{800}\ rpm\ \approx \mathbf{14}\ rps\ \approx \mathbf{88}\ rad/s \tag{4.44}$$

A cam is usually composed by:

- 'Primitive Circle': with radius R and which rotation do not induce any piston translation (and so any specimen deformation);
- 'Eccentric Part': with variable radius and which rotation induce piston translation.

It is possible to make a correspondence between the previous description and the angular rotation described for each part, so we define:

- 'Primitive Circle' $\rightarrow \alpha_0 = 170°$ with α_0 'rest angle';
- 'Eccentric Part':
    1. $\alpha_s = 90°$ with α_s 'slope angle;
    2. $\alpha_k = 10°$ with α_k 'kept angle';
    3. $\alpha_r = 90°$ with α_r 'return angle'.

The angular value are design parameters.
Considering that regime angular speed previously calculated has a constant value, one could obtain the time interval associated with described angles as follow:

- $t_r = 0.033\ s$;
- $t_s = 0.018\ s$;
- $t_k = 0.002\ s$;
- $t_r = 0.018\ s$.

Assuming that the starting point of fatigue test correspond to starting point of 'rest angle',the first requisite which has to be satisfied is that $t_r >$ actuator II transitory , to ensure that when the DC brushless start the traction, it is in the regime power. For the DC brushless chosen, the transitory is in the order of $10^{-3}s$, and so the first requisite is ensured.

The second step is to determinate the angular function $y(\alpha)$ which describes cam geometrical shape. To identify this function the boundary conditions are imposed as follow:

$$\begin{aligned} y(0) &= 0 \\ y(\alpha_s) &= \varepsilon_{max} \\ y'(\alpha_s) &= 0 \end{aligned} \tag{4.45}$$

To ensure that no detaching happen at any point of cam trajectory, the third derivative (jerk) of angular function has to be zero at any point. So assuming a constant acceleration function we ensure this requisite, as shown in th following figure:

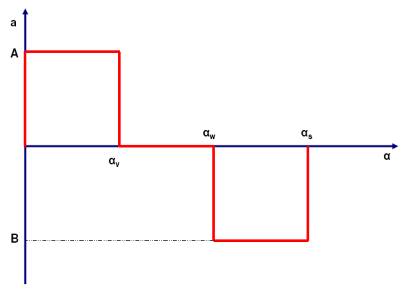

Figure 4.18: Shifting piston induced accaleration.

In figure 4.18 we identify the acceleration profile where:

- $0 \geq \alpha \leq \alpha_v$: $a = A$;
- $\alpha_v < \alpha \leq \alpha_W$: $a = 0$;
- $\alpha_w < \alpha \leq \alpha_s$: $a = B$.

To transmit the most regular motion to the piston we assume that:

- $\alpha_v = 30°$;

- $\alpha_w = 60°$;
- $A = B$.

The described profile ensure that the mean value of acceleration plot is zero which is a design requirement. The angular function is obtained by two integration of acceleration profile, as shown:

- For $0 \geq \alpha \leq \alpha_v$:

$$\begin{aligned} y''(\alpha) &= A \\ y'(\alpha) &= \int_0^\alpha A d\alpha = a\alpha \rightarrow y'(\alpha_v) = A\alpha_v \\ y(\alpha) &= \int_0^\alpha y'(\alpha) d\alpha = \frac{1}{2}A\alpha^2 \\ \rightarrow y(\alpha_v) &= \frac{1}{2}A\alpha_v^2 \end{aligned} \tag{4.46}$$

- For $\alpha_v \geq \alpha \leq \alpha_w$:

$$\begin{aligned} y''(\alpha) &= 0 \\ y'(\alpha) &= A\alpha_v = const. \rightarrow y'(\alpha_w) = A\alpha_v \\ y(\alpha) &= y(\alpha_v) + \int_{\alpha_v}^\alpha y'(\alpha) d\alpha = A\alpha_v \left(\alpha - \frac{\alpha_v}{2}\right) \\ \rightarrow y(\alpha_w) &= A\alpha_v \left(\alpha_w - \frac{\alpha_v}{2}\right) \end{aligned} \tag{4.47}$$

- For $\alpha_w \geq \alpha \leq \alpha_s$:

$$\begin{aligned} y''(\alpha) &= -A \\ y'(\alpha) &= y'(\alpha_w) + \int_{\alpha_w}^\alpha -A d\alpha = \\ &= A\alpha_v - A(\alpha - \alpha_w) \\ \rightarrow y'(\alpha_s) &= A\alpha_v - A(\alpha_s - \alpha_w) \\ y(\alpha) &= y(\alpha_w) + \int_{\alpha_w}^\alpha y'(\alpha) d\alpha = \\ &= A\alpha_v \left(\alpha - \frac{\alpha_v}{2}\right) - \frac{A}{2}(\alpha - \alpha_w)^2 \\ \rightarrow y(\alpha_s) &= A\alpha_v \left(\alpha_s - \frac{\alpha_v}{2}\right) - \frac{A}{2}(\alpha_s - \alpha_w)^2 \end{aligned} \tag{4.48}$$

The cam profile is given by the shape function $R(\alpha)$, which has the following general structure:

$$\mathbf{R}(\alpha) = \mathbf{R} + \mathbf{y}(\alpha) \tag{4.49}$$

where R is the primitive circle radius and $y(\alpha)$ is the angular function above described. In figure 4.19 a cam profile is shown for $\varepsilon_{max} = 10\ mm$, in appendix D a simple Matlab routine is presented which allow to evaluate the cam profile for any ε required. The cam width

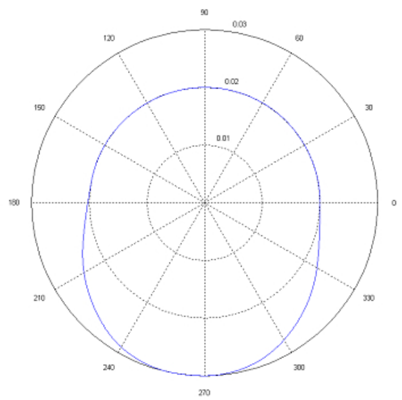

Figure 4.19: Cam profile for the imposed deformation.

is fixed at 20 mm .

4.3.10 Actuator II Shaft Verify

In this case , actuator II shaft is strongly subjected to fatigue, so the approach followed for shaft I may not ensure a safety evaluation. For our purposes the Gough-Pollard criterion, which is common for fatigue application, is more appropriated. We do not present the criterion demonstration, which result allows to evaluate shaft diameter as follow:

$$\mathbf{d_{II}} = \sqrt[3]{n\frac{32}{\pi}\sqrt{\left(\frac{M_a}{\sigma_r}\right)^2 + \left(\frac{T_m}{\sigma_y}\right)^2}} \approx \mathbf{0.012}\ m \qquad (4.50)$$

where:

- $M_a = \frac{M_{max}-M_{min}}{2}$ (where M is bending induced by F_{res});
- T_m = actuator applied torque (2 Nm) for the chosen DC brushless;
- $\sigma_y = 200\ MPa$, if steel is considered;
- $\sigma_r = 0.4\sigma_f$, (failure stress);
- $\sigma_f = 500\ MPa$, if steel is considered.

A good M_a value could be calculated assuming as a design parameter that the length of the shaft between the actuator II and the cam ($l_{shaftII}$) is 0.01 m :

$$\mathbf{M_a} = \frac{\mathbf{F_{res}} \cdot \mathbf{l_{shaftII}}}{\mathbf{2}} = \mathbf{35}\ Nm \qquad (4.51)$$

where F_{res} is considered 7 kN for a safety evaluation.
The first d_{II} value is given for $n = 1$ where n is an additional safety design factor.
In the practice it is usually fixed as $n = 2.5$ which allow to obtain $d_{II} \approx 0.0165\ m$. The DC brushless actuator chosen, has a shaft with $d = 0.018\ m$

4.3.11 Cam-Piston Contact

To ensure the minimum friction effect, a customized solution is presented to improve contact problem approach. We modified shifting piston by introducing elements in figure 4.20.

The pin and the disc ensure that the contact will be between two

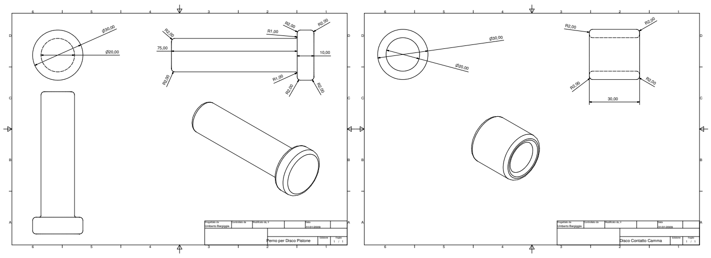

Figure 4.20: Pin and Disc components.

rounding components, by increasing the surface contact area and by reducing the friction effect.

The final shifting mechanism is shown in figure 4.3.

Moreover the presented solution allows that when wear will cause components failure only the elements in figure 4.3 may have to change, instead of all piston.

A Teflon cover for the disc has been considered to reduce material heatment induced by friction.

4.3.12 Spring Calibration

In this section the spring calibration will be described, to ensure shifting piston elastic return with no stresses induced on specimen.

The steps for springs calculation are the following:

- Identification of shifting piston and its relative components mass as a consequence of their volume and the chosen material (steel) density;

- Identification of required load to ensure shifting piston return by calculating the required acceleration to ensure agreement with cam induced displacement;

- Elasticity springs constant (K_{spring}) calculation by Hook's law.

Components Mass Calculation

The program used for mechanical drawings allows to evaluate designed component volumes and they result:

- Shifting Piston: $V_{sp} = 1.234 \cdot 10^{-3}\ m^3$;
- Pin: $V_P = 3.044 \cdot 10^{-5}\ m^3$;
- Disc: $V_D = 1.151 \cdot 10^{-5}\ m^3$;

Considering that they are steel maiden ($\rho = 7850\ kg/m^3$), the mass, $mass_{tot}$ is given:

$$\begin{aligned} mass_{tot} &= (V_{sp} + V_P + V_D) \cdot \rho = (1.3 \cdot 10^{-3}\ m^3\ ) \cdot 7850\ kg/m^3 \\ &= 10.02\ kg \end{aligned} \tag{4.52}$$

Identification of Requird Load

Shifting piston displacement is determined by cam profile. So shifting piston must return in the same time required for cam return ($t_r = 0.018\ s$). So, if a maximum deformation $\varepsilon_{max} = 0.012\ m$ is considered, the medium speed, v_m, could be calculated:

$$\mathbf{v_m} = \frac{\varepsilon_{\mathbf{max}}}{\mathbf{t_s}} = \frac{\mathbf{0.012}\ m}{\mathbf{0.018}\ s} = \mathbf{0.67}\ m/s \tag{4.53}$$

Cam induced acceleration has a known profile given in section 4.3.9, which ensure that the speed profile is trapezoidal. So the maximum speed value is given by the following relationship:

$$\begin{aligned} \mathbf{v_m} = \frac{\mathbf{1}}{\mathbf{t_r}} \int_0^{\mathbf{t_r}} \mathbf{v(t)dt} = \frac{\mathbf{5}}{\mathbf{8}} \mathbf{v_{max}}\ [m/s] \\ \mathbf{v_{max}} = \mathbf{1.07}\ m/s \end{aligned} \tag{4.54}$$

With analogous considerations, also the maximum acceleration could be calculated, as shown:

$$\mathbf{a_{max}} = \frac{\mathbf{v_{max}}}{\frac{\mathbf{3}}{\mathbf{8}}\mathbf{t_r}} \approx \mathbf{87}\ m/s^2 \tag{4.55}$$

Now we could calculate springs required load to ensure that shifting piston do not burden on specimen:

$$\mathbf{F} = \frac{\mathbf{mass_{tot} \cdot a_{max}}}{\mathbf{2}} \approx \mathbf{436}\ N \tag{4.56}$$

K_{spring} Calculation

For compression springs, the elastic constant value is given by the Hook's Law:

$$\mathbf{K_{spring}} = -\frac{\mathbf{F}}{\varepsilon_{\mathbf{max}}} = \frac{\mathbf{mass_{tot} \cdot a_{max}}}{\mathbf{2}\varepsilon_{\mathbf{max}}} \approx \mathbf{37000}\ N/m \tag{4.57}$$

4.4 Tolerances and Couplings

The aim of this section is to identify the most adequate tolerances and couplings for designed component. Every designed component has its relative quotations which coming from analytical calculation or from design requirements.
The theoretical measures may not be exactly realized when the components are built, even if numerical control machines are used. So every component needs a design 'tolerance'to be specified to take in account induced realization errors.
Another problem is the coupling between each components. In fact, a gap between two coupled components must be required to ensure components ability to take its designed collocation and its required function.

4.4.1 Tolerance

As previously introduced a measure could never be exactly realized, so a maximum and a minimum admitted value must be detailed as a result of the precision required for design specification. So the calculated ideal dimension is commonly define as 'nominal dimension' which identify the so called 'zero line' from which the maximum and the minimum removal are measured as follow:

$$\begin{aligned} e_s &= d_s - D \\ e_i &= d_i - D \\ IT &= e_s - e_i = d_s - d_i \end{aligned} \tag{4.58}$$

where:

- D : 'nominal dimension';
- d_s, d_i : maximum and minimum admitted dimensions;
- e_s, e_i : superior and inferior removal;
- IT : tolerance.

The small letters are used for male components and the capital letter for female ones.
Tolerance values are tabulated and are standardized to ensure correspondence between different realized components. Its value is a consequence of component dimension and required realization precision, so:

- $1 \geq D \leq 500\ mm\ \rightarrow IT = 01, 0$ to 17
- $500 < D \leq 3150\ mm\ \rightarrow IT = 6$ to 16

The tolerance values are shown in figure 4.21:
The tolerance field disposition is defined by the 'fundamental removal' which is the absolute minimum distance between 'tolerance zone' and 'zero line'. Fundamental removal positions are defined by a letter, capital for female and small for male components.
For male components:

Dimensione nominale		Gradi di tolleranze normalizzate	
mm		IT01	IT0
oltre	fino a	tolleranza µm	
–	3	0,3	0,5
3	6	0,4	0,6
6	10	0,4	0,6
10	18	0,5	0,8
18	30	0,6	1
30	50	0,6	1
50	80	0,8	1,2
80	120	1	1,5
120	180	1,2	2
180	250	2	3
250	315	2,5	4
315	400	3	5
400	500	4	6

Dimensione nominale mm		GRADI DI TOLLERANZA NORMALIZZATI																	
		IT1	IT2	IT3	IT4	IT5	IT6	IT7	IT8	IT9	IT10	IT11	IT12	IT13	IT14	IT15	IT16	IT17	IT18
oltre	fino a	Tolleranze																	
		µm											mm						
–	3	0,8	1,2	2	3	4	6	10	14	25	40	60	0,1	0,14	0,25	0,4	0,60	1	1,4
3	6	1	1,5	2,5	4	5	8	12	18	30	48	75	0,12	0,18	0,3	0,48	0,75	1,2	1,8
6	10	1	1,5	2,5	4	6	9	15	22	36	58	90	0,15	0,22	0,36	0,58	0,9	1,5	2,2
10	18	1,2	2	3	5	8	11	18	27	43	70	110	0,18	0,27	0,43	0,7	1,1	1,8	2,7
18	30	1,5	2,5	4	6	9	13	21	33	52	84	130	0,21	0,33	0,52	0,84	1,3	2,1	3,3
30	50	1,5	2,5	4	7	11	16	25	39	62	100	160	0,25	0,39	0,62	1	1,6	2,5	3,9
50	80	2	3	5	8	13	19	30	46	74	120	190	0,3	0,46	0,74	1,2	1,9	3	4,6
80	120	2,5	4	6	10	15	22	35	54	87	140	220	0,35	0,54	0,87	1,4	2,2	3,5	5,4
120	180	3,5	5	8	12	18	25	40	63	100	160	250	0,4	0,63	1	1,6	2,5	4	6,3
180	250	4,5	7	10	14	20	29	46	72	115	185	290	0,46	0,72	1,15	1,85	2,9	4,6	7,2
250	315	6	8	12	16	23	32	52	81	130	210	320	0,52	0,81	1,3	2,1	3,2	5,2	8,1
315	400	7	9	13	18	25	36	57	89	140	230	360	0,57	0,89	1,4	2,3	3,6	5,7	8,9
400	500	8	10	15	20	27	40	63	97	155	250	400	0,63	0,97	1,55	2,5	4	6,3	9,7
500	630	9	11	16	22	32	44	70	110	175	280	440	0,7	1,1	1,75	2,8	4,4	7	11
630	800	10	13	18	25	36	50	80	125	200	320	500	0,8	1,25	2	3,2	5	8	12,5
800	1.000	11	15	21	28	40	56	90	140	230	360	560	0,9	1,4	2,3	3,6	5,6	9	14
1.000	1.250	13	18	24	33	47	66	105	165	260	420	660	1,05	1,65	2,6	4,2	6,6	10,5	16,5
1.250	1.600	15	21	29	39	55	78	125	195	310	500	780	1,25	1,95	3,1	5	7,8	12,5	19,5
1.600	2.000	18	25	35	46	65	92	150	230	370	600	920	1,5	2,3	3,7	6	9,2	15	23
2.000	2.500	22	30	41	55	78	110	175	280	440	700	1100	1,75	2,8	4,4	7	11	17,5	28
2.500	3.150	26	36	50	68	96	135	210	330	540	860	1350	2,1	3,3	5,4	8,6	13,5	21	33

Figure 4.21: Tolerance values.

- $e_i = e_s - IT$: from a to h;
- $e_s = e_i + IT$: from j to zc;
- Symmetric with respect to zero line : js.

For female components:

- $E_s = E_i + IT$: from A to H;
- $E_i = E_s - IT$: from J to ZC;
- Symmetric with respect to zero line : JS.

Qualitative disposition are shown in figure 4.22.

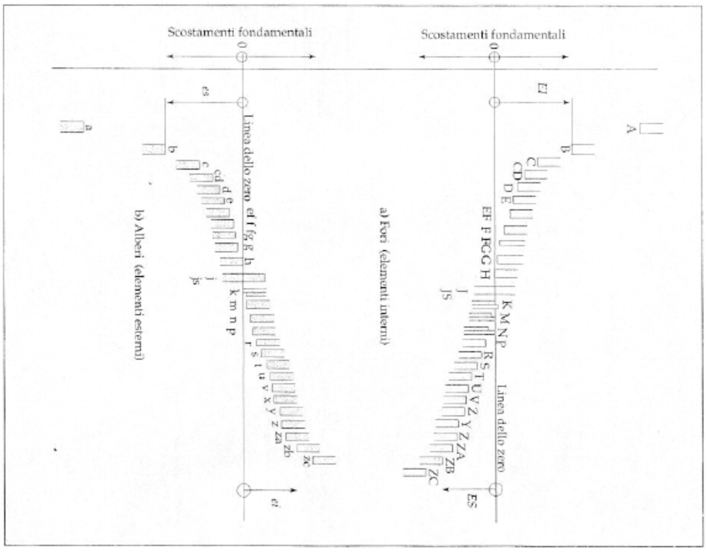

Figure 4.22: Tolerance field displacement.

4.4.2 Couplings

Tolerances are referred to each separated component, while between two components it is better to define coupling. The quantity that identify coupling between male and female components is defined by:

$$\begin{aligned} D_s - d_i &: \text{ maximum value} \\ D_i - d_s &: \text{ minimum value} \end{aligned} \tag{4.59}$$

Three differents type of couplings could be obtained as a consequence of chosen tolerance values:

- Mobile: $D_s - d_i > 0$ and $D_i - d_s > 0$;
- Stable: $D_s - d_i < 0$ and $D_i - d_s < 0$;
- Variable: $D_s - D_i > 0$ and $D_i - d_s < 0$.

In mobile condition, the preceding differences are defined gap, while in stable conditions they are defined as interference.

4.4.3 Couplings for Fatigue Machine Components

As a consequence of the preceding section, we could establish the couplings between each machine component.
The coupling are divided in two main families:

- Coupling between component and workbench;
- Coupling between moving components.

Component and Workbench

The coupling between components and workbench require an elevated precision to allow the minimum gap during fatigue test implementation and to guaranty the maximum stiffness of machine assembly.
So we decided for $H7 - h6$ coupling (See figure 4.23).

Moving Components

The coupling between moving components has to be very precise to ensure axiality maintenance, but at the same time, it has to ensure a minimum gap to reduce components friction.
We decided for $F8 - h6$ coupling (See figure 4.23)
All the contact areas between moving components may have to be lubricated, that's another reason for gap between coupled components.

DIMENSIONE NOMINALE mm		SCOSTAMENTO SUPERIORE es												VALORI DEGLI SCOSTAMENTI FONDAMENTALI				
		GRADI DI TOLLERANZA												IT5 e IT6	IT7	IT7	IT4 a IT7	fino a IT3 e sopra a IT7
oltre	fino a	a [1]	b [1]	c	cd	d	e	ef	f	fg	g	h	js [2]	j			k	
–	3 [1]	– 270	– 140	– 60	– 34	– 20	– 14	– 10	– 6	– 4	– 2	0	Scostamenti = $\pm \frac{ITn}{2}$, dove n è il valore del grado di tolleranza IT	– 2	– 4	– 6	0	0
3	6	– 270	– 140	– 70	– 46	– 30	– 20	– 14	– 10	– 6	– 4	0		– 2	– 4		+ 1	0
6	10	– 280	– 150	– 80	– 56	– 40	– 25	– 18	– 13	– 8	– 5	0		– 2	– 5		+ 1	0
10	14	– 290	– 150	– 95		– 50	– 32		– 16		– 6	0		– 3	– 6		+ 1	0
14	18																	
18	24	– 300	– 160	– 110		– 65	– 40		– 20		– 7	0		– 4	– 8		+ 2	0
24	30																	
30	40	– 310	– 170	– 120		– 80	– 50		– 25		– 9	0		– 5	– 10		+ 2	0
40	50	– 320	– 180	– 130														
50	65	– 340	– 190	– 140		– 100	– 60		– 30		– 10	0		– 7	– 12		+ 2	0
65	80	– 360	– 200	– 150														
80	100	– 380	– 220	– 170		– 120	– 72		– 36		– 12	0		– 9	– 15		+ 3	0
100	120	– 410	– 240	– 180														
120	140	– 460	– 260	– 200		– 145	– 85		– 43		– 14	0		– 11	– 18		+ 3	0
140	160	– 520	– 280	– 210														
160	180	– 580	– 310	– 230														
180	200	– 660	– 340	– 240		– 170	– 100		– 50		– 15	0		– 13	– 21		+ 4	0
200	225	– 740	– 380	– 260														
225	250	– 820	– 420	– 280														
250	280	– 920	– 480	– 300		– 190	– 110		– 56		– 17	0		– 16	– 26		+ 4	0
280	315	– 1050	– 540	– 330														
315	355	– 1200	– 600	– 360		– 210	– 125		– 62		– 18	0		– 18	– 29		+ 4	0
355	400	– 1350	– 680	– 400														
400	450	– 1500	– 760	– 440		– 230	– 135		– 68		– 20	0		– 20	– 32		+ 5	0
450	500	– 1650	– 840	– 480														
500	560					– 260	– 145		– 76		– 22	0					0	0
560	630																	
630	710					– 290	– 160		– 80		– 24	0					0	0
710	800																	
800	900					– 320	– 170		– 86		– 26	0					0	0
900	1000																	
1000	1120					– 350	– 195		– 98		– 28	0					0	0
1120	1250																	
1250	1400					– 390	– 220		– 110		– 30	0					0	0
1400	1600																	
1600	1800					– 430	– 240		– 120		– 32	0					0	0
1800	2000																	
2000	2240					– 480	– 260		– 130		– 34	0					0	0
2240	2500																	
2500	2800					– 520	– 290		– 145		– 38	0					0	0
2800	3150																	

DIMENSIONE NOMINALE mm		SCOSTAMENTI INFERIORI ei													
		GRADI DI TOLLERANZA													
oltre	fino a	m	n	p	r	s	t	u	v	x	y	z	za	zb	zc
–	3 [1]	+ 2	+ 4	+ 6	+ 10	+ 14		+ 18		+ 20		+ 26	+ 32	+ 40	+ 60
3	6	+ 4	+ 8	+ 12	+ 15	+ 19		+ 23		+ 28		+ 35	+ 42	+ 50	+ 80
6	10	+ 6	+ 10	+ 15	+ 19	+ 23		+ 28		+ 34		+ 42	+ 52	+ 67	+ 97
10	14	+ 7	+ 12	+ 18	+ 23	+ 28		+ 33		+ 40		+ 50	+ 64	+ 90	+ 130
14	18								+ 39	+ 45		+ 60	+ 77	+ 108	+ 150
18	24	+ 8	+ 15	+ 22	+ 28	+ 35		+ 41	+ 47	+ 54	+ 63	+ 73	+ 98	+ 136	+ 188
24	30						+ 41	+ 48	+ 55	+ 64	+ 75	+ 88	+ 118	+ 160	+ 218
30	40	+ 9	+ 17	+ 26	+ 34	+ 43	+ 48	+ 60	+ 68	+ 80	+ 94	+ 112	+ 148	+ 200	+ 274
40	50						+ 54	+ 70	+ 81	+ 97	+ 114	+ 136	+ 180	+ 242	+ 325
50	65	+ 11	+ 20	+ 32	+ 41	+ 53	+ 66	+ 87	+ 102	+ 122	+ 144	+ 172	+ 226	+ 300	+ 405
65	80				+ 43	+ 59	+ 75	+ 102	+ 120	+ 146	+ 174	+ 210	+ 274	+ 360	+ 480
80	100	+ 13	+ 23	+ 37	+ 51	+ 71	+ 91	+ 124	+ 146	+ 178	+ 214	+ 258	+ 335	+ 445	+ 585
100	120				+ 54	+ 79	+ 104	+ 144	+ 172	+ 210	+ 254	+ 310	+ 400	+ 525	+ 690
120	140	+ 15	+ 27	+ 43	+ 63	+ 92	+ 122	+ 170	+ 202	+ 248	+ 300	+ 365	+ 470	+ 620	+ 800
140	160				+ 65	+ 100	+ 134	+ 190	+ 228	+ 280	+ 340	+ 415	+ 535	+ 700	+ 900
160	180				+ 68	+ 108	+ 146	+ 210	+ 252	+ 310	+ 380	+ 465	+ 600	+ 780	+ 1000
180	200	+ 17	+ 31	+ 50	+ 77	+ 122	+ 166	+ 236	+ 284	+ 350	+ 425	+ 520	+ 670	+ 880	+ 1150
200	225				+ 80	+ 130	+ 180	+ 258	+ 310	+ 385	+ 470	+ 575	+ 740	+ 960	+ 1250
225	250				+ 84	+ 140	+ 196	+ 284	+ 340	+ 425	+ 520	+ 640	+ 820	+ 1050	+ 1350
250	280	+ 20	+ 34	+ 56	+ 94	+ 158	+ 218	+ 315	+ 385	+ 475	+ 580	+ 710	+ 920	+ 1200	+ 1150
280	315				+ 98	+ 170	+ 240	+ 350	+ 425	+ 525	+ 650	+ 790	+ 1000	+ 1300	+ 1700
315	355	+ 21	+ 37	+ 62	+ 108	+ 190	+ 268	+ 390	+ 475	+ 590	+ 730	+ 900	+ 1150	+ 1500	+ 1900
355	400				+ 114	+ 208	+ 294	+ 435	+ 530	+ 660	+ 820	+ 1000	+ 1300	+ 1650	+ 2100
400	450	+ 23	+ 40	+ 68	+ 126	+ 232	+ 330	+ 490	+ 595	+ 740	+ 920	+ 1100	+ 1450	+ 1850	+ 2400
450	500				+ 132	+ 252	+ 360	+ 540	+ 660	+ 820	+ 1000	+ 1250	+ 1600	+ 2100	+ 2600
500	560	+ 26	+ 44	+ 78	+ 150	+ 280	+ 400	+ 600							
560	630				+ 155	+ 310	+ 450	+ 660							
630	710	+ 30	+ 50	+ 88	+ 175	+ 340	+ 500	+ 740							
710	800				+ 185	+ 380	+ 560	+ 840							
800	900	+ 34	+ 56	+ 100	+ 210	+ 430	+ 620	+ 940							
900	1000				+ 220	+ 470	+ 680	+ 1050							
1000	1120	+ 40	+ 66	+ 120	+ 250	+ 520	+ 780	+ 1150							
1120	1250				+ 260	+ 580	+ 840	+ 1300							
1250	1400	+ 48	+ 78	+ 140	+ 300	+ 640	+ 960	+ 1450							
1400	1600				+ 330	+ 720	+ 1050	+ 1600							
1600	1800	+ 58	+ 92	+ 170	+ 370	+ 820	+ 1200	+ 1850							
1800	2000				+ 400	+ 920	+ 1350	+ 2000							
2000	2240	+ 68	+ 110	+ 195	+ 440	+ 1000	+ 1500	+ 2300							
2240	2500				+ 460	+ 1100	+ 1650	+ 2500							
2500	2800	+ 76	+ 135	+ 240	+ 550	+ 1250	+ 1900	+ 2900							
2800	3150				+ 580	+ 1400	+ 2100	+ 3200							

Figure 4.23: Gap values.

4.5 Prototype for Radial Expansion

In this section of fatigue machine design a customized mechanism to investigate stent behaviour if subjected to radial stress state is presented. We give only a qualitative drawing to show the idea, but we do not finish yet to establish the right dimension of each component part.
The idea is to use the translation that fatigue machine is able to perform to induce a radial stent displacement. So the solution is given by a pumping-grasp system and its components are shown in figure 4.24.

The assembly of this two components coupled with a customized

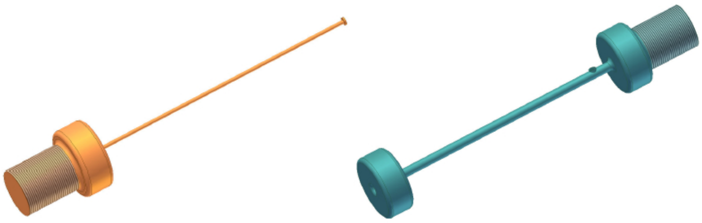

Figure 4.24: Pumping grasp elements.

balloon on which the stent will be located will allow a fatigue stent test (Figure 4.25).

Moreover, the development of this customized grasp will allow to

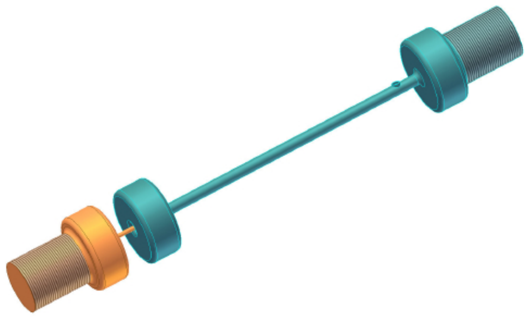

Figure 4.25: Pumping grasp system.

implement a validation of expansion simulation performed with FEA. The calculation of component quotation is more complex because this mechanism has viscous properties, so its responds is rate dependent.

4.6 Cost Evaluation

The last section of fatigue machine design chapter is reserved to cost evaluation. Costs are a consequence of:

- Material and Realization: Officina 'Micron 77' ≈ 3000.00 Euro (30% material, 70% high-precision manufacturing);

- Electric Actuators:

  1. Actuator I: OrientalMotor S.r.l. stepper actuator kit CRK569BP, Five steps technology.
     High motion resolution: 0.72° each step.
     Feeding: DC.
     Ultra compact dimensions: 65 x 45 x 25 mm .
     Mechanical resolution: 200 steps per round.
     Static C_{res}: 1.66 Nm .
     Shaft diameter: 7.5 mm .
     SubTotal..314.00 Euro + iva.
  2. Actuator II: OrientalMotor S.r.l. DC brushless actuator kit BLF6200C−5.
     Feeding: 230 V ,50 Hz .
     Closed actuator speed loop control.
     Control Range: 80 to 4000 rpm .
     8 speed profile programmable memory.
     Digital display with angular speed, linear speed and used power.
     Dynamic C_{res}: 2 Nm . SubTotal...632.40 Euro + iva.

- Load Cell: DS Europe S.R.L. load cell, Mod.546QDT−A1−3000 Kg, high endurance steel made.
  Measure field: 0 to 3000 Kg in both traction and compression direction.
  Output: 0 to 10 V .

Feeding: 18 V to 28 V .

SubTotal..827.00 Euro + iva.

Total fatigue machine realization.............................$\approx$ 5200 euro.

4.7 References

A.R Pelton et Al.; Optimization of processing and properties of medical grade Nitinol wire.

A.Agosti; Manuale di Meccanica; Lattes -1981.

G.Petrucci; Lezioni di Costruzioni di Macchine.

R. Giovannozzi; Costruzione di Macchine vol.2; Patron Editrice; Bologna 1980.

P.L. Magnani, G. Ruggieri; Meccanismi per Macchine Automatiche.

Nuovo Colombo; Manuale dell'Ingegnere; Hoepli.

Chapter 5

Practical Application

In this chapter, a practical application of stent fatigue life prediction will be presented. Performing this example the steps described in the preceding chapters will be followed.
The fatigue life evaluation presented in the following doesn't want to be a real stent fatigue life prediction, because some of the material parameters used for the analytical calculation are obtained from ASTM Material Handbook instead of directly evaluated from experimental procedures. So, the value of these parameters gives a qualitative representation of stent material behaviour and they are not specific for the analyzed stent.
We are going to indicate such variables which values have been taken from ASTM Handbook, to make the reader able to understand which results are specific for the analyzed stent and which of these just show the analytical procedure application.
This application will also allow us to evaluate both designed machine ability to correctly characterize material properties and analytical model efficacy. In fact, if fatigue test machine calibration will give positive answer, the results of analytical approach that we presented could be verified.
So in this chapter the following argument will be presented:

- Cypher $SS316L$ steel stent elasto$-$plastic calculation.
  The calculation with FEM take firstly into account stent de-

ployment and the relative elastic recoil to localize where the plastic deformations will be dominant and by consequence where the macrocracks may initiate. Secondly, both diastolic and systolic stresses evaluation has been performed to quantify the stresses acting on stent surfaces. The analysis have been performed with Abaqus v. 6.8, which is the most used FEM commercial solution;

- Material (steel $SS316L$) and damage parameters evaluation from both literature values and practical application of Chapter 2 contents;

- Analytical fatigue life evaluation by coupling Chapter 1, 2 and 3 concepts.

5.1 Cypher Stent Elasto−Plastic Calculation

We perform with Abaqus a FEM evaluation of a stent considering the phenomenon physiological dynamics.
The analysis has been divided in two steps:

- Step 1: simulation of stent deployment. This step allows to evaluate the plastic strains induced in Cypher stent which guarantee the maintenance of expanded configuration.
  Then we take in account for stent elastic recoil, which induce a small stent diameter reduction.

- Step 2: simulation of diastolic and systolic induced stresses. This step has been implemented to evaluate the stress range which the heart beats (by vessel contact) induce on stent surface.

To perform the described steps, the following phases have been taken in account:

- Stent mesh implementation in Abaqus $v.6.8$;
- Elasto−Plastic evaluation, by displacement imposition, to analyze the deployment and elastic recoil maximum plastic deformation induced on stent struts;
- Results presentation;
- Physiological pressure (induced by heart beats by vessel contact) implementation to evaluate von Mises equivalent stress, Maximum principal stress and Stress range resulting on stent surface;
- Result presentation.

5.1.1 Stent Deployment Implementation

Cypher is a $SS316L$ steel maiden stent for coronary diseases. The stent acts as a scaffold to help hold the artery open in order to improve blood flow to the heart and relieve the symptoms caused by the blockage.
The stent is characterized by the following geometrical parameters:

- Initial external diameter: $d_0 = 1.15\ mm$;
- Strut thickness: $th = 0.3\ mm$;
- Expanded diameter: $d_{exp} = 3.0\ mm$ (vessel diameter);
- Recoil diameter: $d_{recoil} = 2.95\ mm$;
- Longitudinal initial length: $l_i = 8.4\ mm$;
- Longitudinal expanded length: $l_{exp} \approx 7.6\ mm$.

The Abaqus mesh for analysis running, has been taken from the Ghent Stent Research Unit (Belgium) dedicated link (*http : //www.stent-ibitech.ugant.be*) and implemented for the calculation (Fig.5.1).
To ensures analysis convergence, the elements used for mesh generation are:

Figure 5.1: Mesh for Cypher stent

- $C3D8R$ for stent elements;
- $SFM3D4$ for cylinder elements.

All the analysis was based on large deformation Abaqus modulus and we performed a static analysis with Abaqus standard modulus which implement an implicit integration scheme for results calculation.
To induce the expansion, a cylinder was inserted into the stent, imposing the contact between external cylinder and internal stent surfaces and applying the required displacements to cylinder nodes. So, the cartesian coordinates of each nodes has been transformed in cylindrical coordinates to ensure a correct expansion (Fig.5.2) and elastic recoil (Fig.5.2) simulation.

An elasto−plastic calculation related to the described stent deploy-

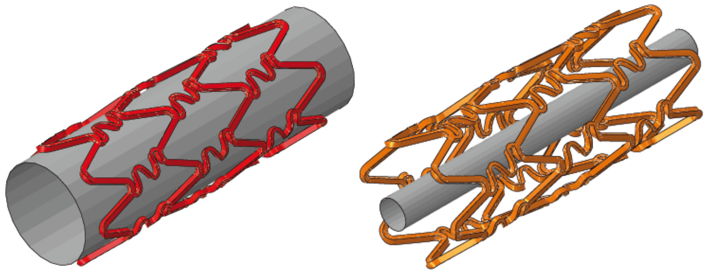

Figure 5.2: Expanded stent configuration followed by elastic recoil configuration.

ment and recoil has been performed to evaluate the maximum residual plastic strain dislocation to detect macrocrack initiation points. In figure 5.3 the plastic strain results are presented.

Finally a calculation of principal stress orientation in the elements

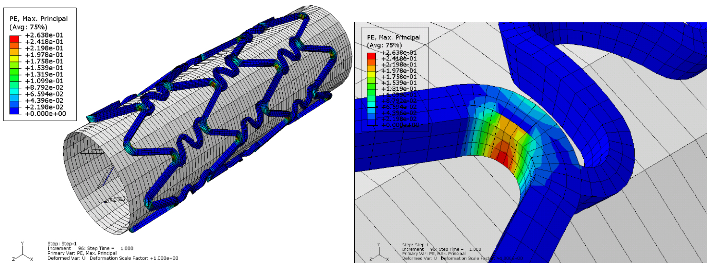

Figure 5.3: Residual plastic strain localization in consequence of stent deployment.

subjected to maximum plastic strain has been required to evaluate initial macrocrack orientation as shown in figure 5.4.

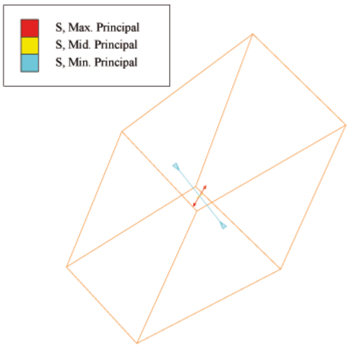

Figure 5.4: Maximum principal stress orientation to evaluate initial macrocrack orientation.

5.1.2 Diastolic and Systolic Stresses Calculation

Once we localized both macrocrack initiation points and macrocracks initial orientation, a heart beats induced stresses calculation has been required to establish the stresses induced on stent surface by both diastolic and systolic pressure.
So, an external cylinder has been designed to simulate the contact between the vessel internal and stent external surfaces.
We applied on the new cylinder surface firstly diastolic and secondly systolic pressure to evaluate the relative stress resulting on stent surface.
The maximum equivalent von Mises stress, the maximum principal stress and the stress range acting on stent surface are required to perform a fatigue life evaluation. The stresses calculation results are shown in figure 5.5 and 5.6.

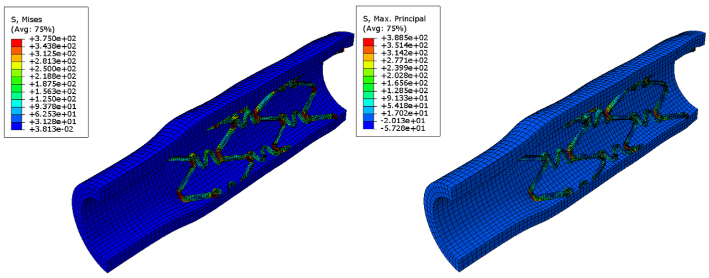

Figure 5.5: von Mises and maximum principal stresses induced on stent surface by diastolic pressure: section view.

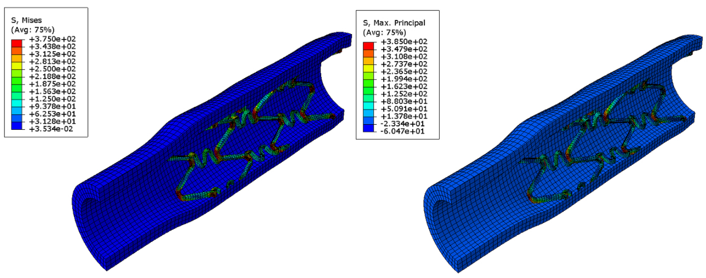

Figure 5.6: von Mises and maximum principal stresses induced on stent surface by systolic pressure: section view.

The analysis shows that:

- Maximum equivalent von Mises stress: 375 MPa ;
- Maximum principal stress: 388.5 MPa ;
- Stress range (referred to maximum preincipal stresses) near crack initiation point: $\approx$ 110 MPa .

5.2 Material and Damage Parameters Evaluation

We chose for this example the Cypher stent for two main reasons:

- It is a stent really used in cardiovascular diseases;
- It is a steel maiden stent, so its material parameters are known.

As shown in Chapter 2, a material parameters evaluation require both tensile and fatigue tests.

5.2.1 Identification from Tensile Tests

In the following the steel parameters which will be evaluated with a tensile application of fatigue machine presented in Chapter 4 are reported with reference to figure 5.7:

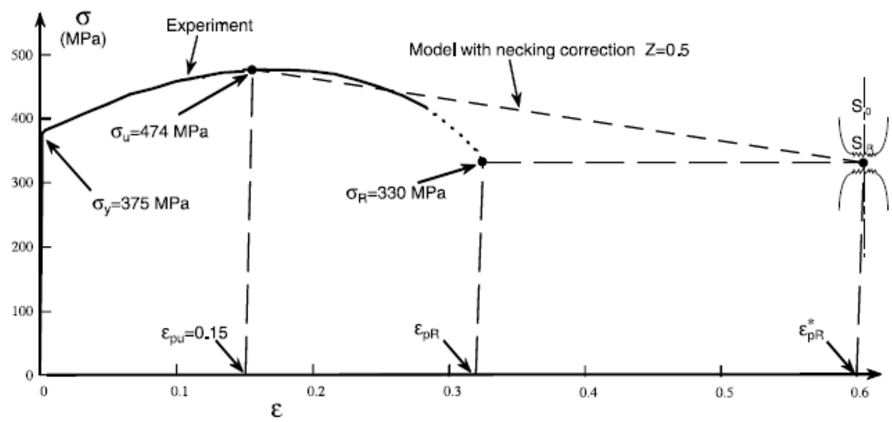

Figure 5.7: Cypher parameters identification from a tensile test on steel at room temperature. Engineering Damage Mechanics: Ductile, Creep, Fatigue and Brittle Failures; Springer.

- Young's modulus: $E = 200000\ MPa$;
- Poisson's ratio: $\nu = 0.3$;
- Yield stress: $\sigma_y = 375\ MPa \longrightarrow \sigma_{02} = 380\ MPa$;
- Ultimate stress: $\sigma_u = 474\ MPa \longrightarrow \varepsilon(\sigma_u) = 0.15$;
- Rupture stress: $\sigma_R = 330\ MPa$;
- Rupture strain: $\varepsilon_{pR} = 0.32$;
- Necking parameter: $Z = (S_0 - S_R)/S_0 = 0.5$;
- Local rupture strain in Necking zone: $\varepsilon^{\star}_{pR} = 2(1 - \sqrt{1-z}) = 0.6$.

These data are referred to SS316l steel, so they will allow us to check fatigue machine reliability.
Remembering that damage starts to grow up when plastic strain reaches the value corresponding to ultimate stress σ_u, we could evaluate the plastic deformation threshold for damage initiation:

$$\varepsilon_{\mathbf{pD}} \approx \varepsilon_{\mathbf{p}}(\sigma = \sigma_{\mathbf{u}}) = \mathbf{0.15} \tag{5.1}$$

Moreover, the critical damage value could be calculated:

$$\mathbf{D_c} = \mathbf{1} - \frac{\sigma_{\mathbf{R}}}{\sigma_{\mathbf{u}}} = \mathbf{0.3} \tag{5.2}$$

5.2.2 Identification from a Fatigue Test

As shown in figure 5.8, from two fatigue tests we could get:

- Fatigue limit (i.e. calculated for 10^6 cycles): $\sigma_f = 220\ MPa$;
- For $\Delta\varepsilon_{p1} = 0.027 \rightarrow N_R = 10$ and $\sigma_{M1} = 450\ MPa$;
- For $\Delta\varepsilon_{p2} = 0.0035 \rightarrow N_R = 100$ and $\sigma_{M2} = 340\ MPa$;

So by solving the following equation coming from Chapter 2 inserting the above presented values, s and m parameters are calculated:

$$\mathbf{N_R} = \frac{\varepsilon_{\mathbf{pD}}}{\mathbf{2\Delta}\varepsilon_{\mathbf{p}}} \left(\frac{\sigma_{\mathbf{u}} - \sigma_{\mathbf{f}}}{\sigma_{\mathbf{max}} - \sigma_{\mathbf{f}}^{\infty}}\right)^{\mathbf{m}} + \frac{\mathbf{1} - (\mathbf{1} - \mathbf{D_c})^{\mathbf{2s+1}}}{\mathbf{2}\,(\mathbf{2s+1})\,\mathbf{D_c}\varepsilon_{\mathbf{p}}} \left(\frac{\sigma_{\mathbf{u}}}{\sigma_{\mathbf{max}}}\right)^{\mathbf{2s}} (\varepsilon_{\mathbf{pR}} - \varepsilon_{\mathbf{pD}}) \tag{5.3}$$

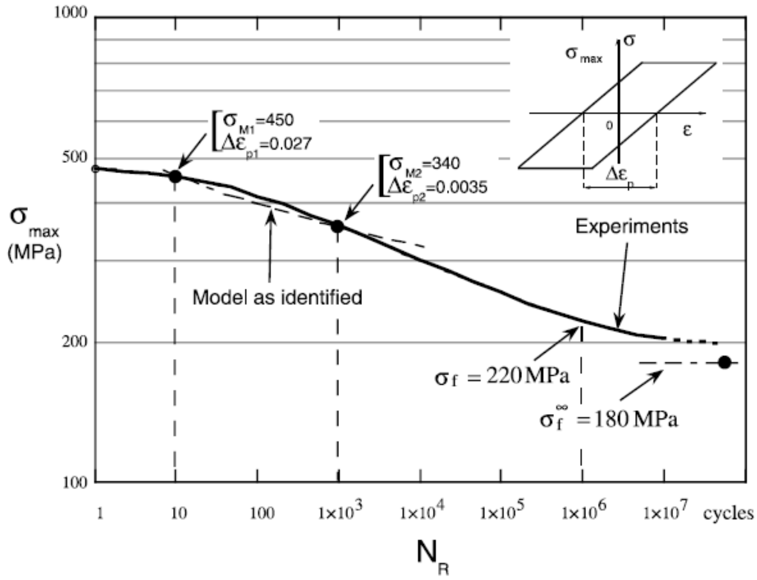

Figure 5.8: Material parameters from a Wohler curve of steel at room temperature. Engineering Damage Mechanics: Ductile, Creep, Fatigue and Brittle Failures; Springer.

$$\begin{aligned} s &= 2.4 \\ m &= 6 \end{aligned} \tag{5.4}$$

Finally, the last parameter, S, could be calculated from the following equation:

$$\mathbf{S} = \frac{\sigma_{\mathbf{u}}^{\mathbf{2}}}{\mathbf{2E}} \left(\frac{\varepsilon_{\mathbf{pR}}^{\star} - \varepsilon_{\mathbf{pD}}}{\mathbf{D_c}} \right)^{\mathbf{1/s}} = \mathbf{0.665}\ MPa \tag{5.5}$$

Now all material parameters are identified and we will be able (if machine calibration will be O.K.) to check the model agreement with test results.

Starting from figure 5.8 we could calculate N_R for every $\sigma_M - \Delta\varepsilon_{pR}$ values (where σ_M is any applied stress); then performing a fatigue test on a steel specimen for a number of cycles equal to the calculated N_R value we could check model validity by verifying if damage results in the following way:

- As mentioned, perform a fatigue test for a number of cycles equal to the calculated N_R;

- Stop the fatigue test and induce specimen static failure to measure the actual Young's modulus value which will be reduced by fatigue damaging;

- Calculate the damage value corresponding to N_R as follow:

$$\mathbf{D} = \mathbf{1} - \frac{\tilde{\mathbf{E}}}{\mathbf{E}} \tag{5.6}$$

where:

1. $\tilde{E}$: damaged Young's modulus;
2. $E =$: true Young's modulus.

- Check if: $D \approx D_c \longrightarrow$ the model is good.

If both described machine calibration and model check will give suitable result, we will be able to evaluate both Nitinol properties and Nitinol stent fatigue macrocrack initiation.

5.3 Analytical Stent Fatigue Life Evaluation

As shown in Chapter 2, to evaluate crack initial length, it could be used the procedure presented in section 2.7.
This procedure is based on the matching between the CDM energy related to both plastic and damage processes and FM energy required for crack initiation (G_c , fracture toughness).
So, the initial crack length, δ_0 , could be calculated as:

$$\delta_{\mathbf{0}} = \frac{\mathbf{G_c}}{\frac{\sigma_\mathbf{u}^\mathbf{2}}{\mathbf{2E}}\mathbf{D_c} + \sigma_\mathbf{u}\varepsilon_\mathbf{pR}} \tag{5.7}$$

In chapter 3 we define the relationship between G_c and K_c as follow:

$$\begin{aligned} K_c &= \sqrt{EG_c} = S\sqrt{\pi a} \longrightarrow 33\ MPa\sqrt{m}\ \text{(ASTM Material Handbook)} \\ G_c &= \frac{K_c^2}{E} = \frac{1089}{200000}\ MPa \cdot m = 0.005445\ MPa \cdot m \end{aligned} \tag{5.8}$$

So δ_0 could be calculated:

$$\delta_{\mathbf{0}} = \frac{\mathbf{0.005445}\ MPa \cdot m}{\mathbf{152.02}\ MPa} \approx \mathbf{35}\ \mu m \tag{5.9}$$

The crack is orientated in the principal stress direction as shown in figure 5.4.
Finally, macrocrack growth evolution comes from Paris law, which allow to evaluate N_p (number of cycles for crack propagation from its initial macro dimension to final failure):

$$\mathbf{N_p} = \frac{\mathbf{2}}{\mathbf{c} \cdot (\mathbf{n}-\mathbf{2}) \cdot \mathbf{f(g)^n \Delta s^n} \cdot \pi^{\frac{\mathbf{n}}{\mathbf{2}}}} \cdot \left(\mathbf{a_0^{1-\frac{n}{2}}} - \mathbf{a_f^{1-\frac{n}{2}}}\right) = \mathbf{2.14} \text{ x } \mathbf{10^8} \tag{5.10}$$

where:

- $c = 5.3$ x 10^{-14}: material parameter taken from ASTM Handbook (Steel);
- $f(g) = 0.629$: crack shape function taken from ASTM Handbook;
- $\Delta\sigma = 110\ MPa$: applied stress range;
- a_o: crack initial length (δ_0);
- a_f: crack final length (80% of stent width).

The result above presented is just a qualitative representation obtained with exemplifying parameter values.
With fatigue machine realization, the material parameters will be calculated for any specific stent material, allowing to evaluate stent fatigue life.

Chapter 6

Further Improvements and Conclusions

This work approaches stent fatigue life prediction, so it has matched a variety of problems which has been simplified. Consequently the following improvements can be performed:

- Analytical Approach:

    1. Non constant amplitude-non proportional loadings (random fatigue) to introduce in fatigue life investigation the stresses coming from external solicitations;
    2. Investigation on anisotropic damage behaviour and implementation of numerical solution to predict fatigue cracks initial size;
    3. Formulation of specific standard procedure customized for HCF.

- Experimental Approach:

    1. Realization of the designed fatigue machine;
    2. Back-loop control system of actuator I, to correct the progressive initial condition changes due to material induced plasticity;

3. Performance of non constant amplitude fatigue test, using the DC brushless ability to implement a specific speed profile as a consequence of a customized programming;
4. Realization of pump-grasping to perform stent radial test.

The aim of this work has been to identify a procedure allowing to evaluate stent fatigue life considering both analytical, experimental and numerical methods.
A review of fatigue theoretical aspects has been firstly presented to obtain the essential knowledge to understand physical mechanisms of fatigue. This review provided a qualitative fatigue description and the standard experimental procedures implemented for material fatigue characterization.
Then, analytical models to investigate the fatigue crack initiation and its evolution has been presented to predict stent fatigue life.
A customized fatigue machine has been designed. The realization of this test machine and the consequent calibration will allow firstly to investigate fatigue material parameters required by the presented analytical models and secondly a direct fatigue life evaluation of a real stent.
Finally, a practical application of the previously discussed methodology has been presented as an example to show how to apply the described procedure for stent fatigue life prediction.
In this practical application, a finite element analysis of Cypher stent has been performed to evaluate the stent stress state under a cardiac cycle.
Consequently the developed framework provides the basis for the evaluation of stent fatigue life ranging from the position, the orientation and the size of initial macrocrack to device final failure.

Appendixes

Appendix A

Griffith Criterion

Surface energy: quantifies the disruption of intermolecular bonds that occurs when a surface is created. In the physics of solids, surfaces must be intrinsically less energetically favourable than the bulk of a material; otherwise there would be a driving force for surfaces to be created, and surface is all there would be. The surface energy may therefore be defined as the excess energy at the surface of a material compared to the bulk.

Surface energy of a solid measurement: the surface energy of a solid is usually measured at high temperatures. At such temperatures the solid creeps and even though the surface area changes, the volume remains approximately constant. If γ is the surface energy density of a cylindrical rod of radius r and length l at high temperature and a constant mono-axial tension P, then at equilibrium, the variation of the total Gibbs free energy vanishes and we have:

$$\delta \mathbf{G} = -\mathbf{P}\delta \mathbf{l} + \gamma \delta \mathbf{A} = \mathbf{0} \tag{A.1}$$

where G is the Gibbs free energy and A is the surface area of the rod:

$$\mathbf{A} = \mathbf{2}\pi \mathbf{r^2} + \mathbf{2}\pi \mathbf{rl} \tag{A.2}$$

$$\delta \mathbf{A} = \mathbf{4}\pi \mathbf{r}\delta \mathbf{r} + \mathbf{2}\pi \mathbf{l}\delta \mathbf{r} + \mathbf{2}\pi \mathbf{r}\delta \mathbf{l} \tag{A.3}$$

Also, since the volume V of the rod remains constant, the variation δV of the volume is zero:

$$\mathbf{V} = \pi \mathbf{r^2 l} = \mathbf{constant} \tag{A.4}$$

$$\delta \mathbf{V} = \mathbf{2\pi rl\delta r} + \pi \mathbf{r^2 \delta l} = \mathbf{0} \tag{A.5}$$

$$\delta \mathbf{r} = -\frac{\mathbf{r}}{\mathbf{2l}}\delta \mathbf{l} \tag{A.6}$$

Therefore, the surface energy density can be expressed as:

$$\gamma = \frac{\mathbf{Pl}}{\pi \mathbf{r}(\mathbf{l} - \mathbf{2r})} \tag{A.7}$$

The surface energy density of the solid can be computed by measuring P, r, and l at equilibrium.

Gibbs free energy: in thermodynamics, the Gibbs free energy (IUPAC recommended name: Gibbs energy or Gibbs function) is a thermodynamic potential which measures the 'useful' or process-initiating work obtainable from an isothermal, isobaric thermodynamic system. Technically, the Gibbs free energy is the maximum amount of non-expansion work which can be extracted from a closed system or this maximum can be attained only in a completely reversible process. When a system changes from a well-defined initial state to a well-defined final state, the Gibbs free energy ΔG equals the work exchanged by the system with its surroundings, less the work of the pressure forces, during a reversible transformation of the system from the same initial state to the same final state. The Gibbs free energy is defined as:

$$\mathbf{G} = \mathbf{U} + \mathbf{pV} - \mathbf{TS} \tag{A.8}$$

which is the same as:

$$\mathbf{G} = \mathbf{H} - \mathbf{TS} \tag{A.9}$$

where:

- U is the internal energy;
- p is pressure;
- V is volume
- T is the temperature
- S is the entropy

- H is the enthalpy

Internal energy: the sum of all microscopic forms of energy of a system.

Appendix B

LEFM Mathematical Foundations

Linear elastic mathematical foundations starting from strain-displacement relationships:

$$\varepsilon_{\mathbf{xx}} = \frac{\delta \mathbf{u_x}}{\delta \mathbf{x}} \varepsilon_{\mathbf{xy}} = \frac{\delta \mathbf{u_y}}{\delta \mathbf{y}} \varepsilon_{\mathbf{xy}} = \frac{\mathbf{1}}{\mathbf{2}} \left(\frac{\delta \mathbf{u_x}}{\delta \mathbf{y}} + \frac{\delta \mathbf{u_y}}{\delta \mathbf{x}} \right) \tag{B.1}$$

where:

- x, y: respectively horizontal and vertical coordinates;
- ε_{xx},ε_{yy}, etc.: displacement components.

The stress-strain relationships could be express in term of:

1. plane-strain conditions

$$\sigma_{xx} = \frac{E}{(1+\nu)(1-2\nu)} \cdot [(1-\nu)\,\varepsilon_{xx} + \nu\varepsilon_{yy}]$$

$$\sigma_{yy} = \frac{E}{(1+\nu)(1-2\nu)} \cdot [(1-\nu)\,\varepsilon_{yy} + \nu\varepsilon_{xx}]$$

$$\tau_{xy} = 2\mu\varepsilon_{xy} = \frac{E}{(1+\nu)} \cdot [\varepsilon_{xy}]$$

$$\sigma_{zz} = \nu \cdot [\sigma_{yy} + \sigma_{xx}]$$

$$\varepsilon_{zz} = \varepsilon_{xz} = \varepsilon_{yz} = \tau_{xz} = \tau_{yz} = 0 \tag{B.2}$$

2. plane-stress conditions

$$\begin{aligned}
\sigma_{xx} &= \frac{E}{(1-\nu^2)} \cdot [\varepsilon_{xx} + \nu\varepsilon_{yy}] \\
\sigma_{yy} &= \frac{E}{(1-\nu^2)} \cdot [\varepsilon_{yy} + \nu\varepsilon_{yy}] \\
\tau_{xy} = 2\mu\varepsilon_{xy} &= \frac{E}{(1+\nu)} \cdot [\varepsilon_{xy}] \\
\varepsilon_{zz} &= -\frac{\nu}{(1-\nu)} \cdot [\varepsilon_{yy} + \varepsilon_{xx}] \\
\sigma_{zz} = \varepsilon_{xz} = \varepsilon_{yz} &= \tau_{xz} = \tau_{yz} = 0
\end{aligned} \tag{B.3}$$

where:

- σ, τ: normal and shear stress components;
- E: Young's modulus;
- ν: Poisson's ratio.

The equilibrium conditions are given by:

$$\begin{aligned}
\frac{\delta\sigma_{xx}}{\delta x} + \frac{\delta\tau_{xy}}{\delta y} &= 0 \\
\frac{\delta\sigma_{yy}}{\delta y} + \frac{\delta\tau_{xy}}{\delta x} &= 0
\end{aligned} \tag{B.4}$$

The compatibility equations is represented by:

$$\nabla^2 (\sigma_{xx} + \sigma_{yy}) = 0 \tag{B.5}$$

where:

$$\nabla^2 = \frac{\delta^2}{\delta x^2} + \frac{\delta^2}{\delta y^2} \tag{B.6}$$

For a two dimensional continuous medium, there exist a function $\Phi(x, y)$,the so called Airy stress function, from which the stresses can be derived:

$$\begin{aligned}
\sigma_{xx} &= \frac{\delta^2\Phi}{\delta y^2} \\
\sigma_{yy} &= \frac{\delta^2\Phi}{\delta x^2} \\
\tau_{xy} &= -\frac{\delta^2\Phi}{\delta x \delta y}
\end{aligned} \tag{B.7}$$

The equilibrium and compatibility equations are automatically satisfied if Φ has the following property:

$$\nabla^2\nabla^2\Phi = 0 \tag{B.8}$$

It is usually introduced polar coordinate system for strain-displacement relationships:

$$\begin{aligned}
\varepsilon_{rr} &= \frac{\delta u_r}{\delta r} \\
\varepsilon_{\theta\theta} &= \frac{u_r}{r} + \frac{\delta u_\theta}{\delta \theta} \\
\varepsilon_{r\theta} &= \frac{1}{2} \cdot \left(\frac{1}{r}\frac{\delta u_r}{\delta \theta} + \frac{\delta u_\theta}{\delta r} - \frac{u_\theta}{r} \right)
\end{aligned} \tag{B.9}$$

where u_r and u_θ are the radial and tangential components respectively. It is useful to write the stress-strain relationships in polar coordinates:

1. plane strain conditions:

$$\sigma_{rr} = \frac{E}{(1+\nu)(1-2\nu)} \cdot \left[(1-\nu)\,\varepsilon_{rr} + \nu\varepsilon_{\theta\theta} \right] \tag{B.10}$$

2. plane stress conditions:

$$\sigma_{rr} = \frac{E}{(1-\nu^2)} \cdot \left[\varepsilon_{rr} + \nu\varepsilon_{\theta\theta} \right] \tag{B.11}$$

Similarly, it is reintroduced the equilibrium equations in polar coordinates:

$$\begin{aligned}
\frac{\delta \sigma_{rr}}{\delta r} + \frac{1}{r}\frac{\delta \tau_{r\theta}}{\delta \theta} + \frac{\sigma_{rr} - \sigma_{\theta\theta}}{\delta r} &= 0 \\
\frac{\delta \tau_{r\theta}}{\delta r} + \frac{1}{r}\frac{\delta \sigma_{\theta\theta}}{\delta \theta} + \frac{2\tau_{r\theta}}{\delta r} = 0 &
\end{aligned} \tag{B.12}$$

and also the compatibility equations:

$$\nabla^2 \left(\sigma_{rr} + \sigma_{\theta\theta} \right) = 0 \tag{B.13}$$

where

$$\nabla^2 = \frac{\delta^2}{\delta r^2} + \frac{1}{r}\frac{\delta}{\delta r} + \frac{1}{r^2}\frac{\delta^2}{\delta \theta^2} \tag{B.14}$$

Finally we rewrite Airy stress function:

$$\nabla^2\nabla^2\Phi = 0 \tag{B.15}$$

where:

$$\begin{aligned}
\Phi &= \Phi(r,\theta) \\
\sigma_{rr} &= \frac{1}{r^2}\frac{\delta^2\Phi}{\delta\theta^2} + \frac{1}{r}\frac{\delta\Phi}{\delta r} \\
\sigma_{\theta\theta} &= \frac{\delta^2\Phi}{\delta r^2} \\
\tau_{r\theta} &= \frac{1}{r^2}\frac{\delta\Phi}{\delta\theta} + \frac{1}{r}\frac{\delta^2\Phi}{\delta\theta\delta r}
\end{aligned} \tag{B.16}$$

The boundary conditions for the plane problem are:

$$\sigma_{\theta\theta} = \sigma_{r\theta} = 0 \text{ for } \theta = \pm\pi \tag{B.17}$$

M.L. Williams [73] [74] was the first to demonstrate the universal nature of $\frac{1}{\sqrt{r}}$ singularity for elastic crack problems. He began by considering stresses at the corner of a plate with various boundary conditions and included angles; a crack is special case where the included angle of the plate corner is 2π and the surfaces are traction free (Fig.B.1). For the configuration in Fig.B.1b, Williams postulated the following stress function:

$$\begin{aligned}
\Phi = r^{\lambda+1}\left[c_1 \sin(\lambda+1)\theta^* + c_2\cos(\lambda+1)\theta^*\right] + \\
+ r^{\lambda+1}\left[c_3 \sin(\lambda-1)\theta^* + c_4\cos(\lambda-1)\theta^*\right] = r^{\lambda-1}\Phi(\theta^*,\lambda)
\end{aligned} \tag{B.18}$$

where c_1, c_2, c_3, c_4 are constants, and θ^* is defined in Fig.B.1b. The following expressions for the stresses is given by invoking the Airy stress function in polar coordinates:

$$\begin{aligned}
\sigma_{rr} &= r^{\lambda-1}\left[F''(\theta^*) + \lambda + 1F(\theta^*)\right] \\
\sigma_{\theta\theta} &= r^{\lambda-1}\left[\lambda(\lambda+1)F(\theta^*)\right] \\
\tau_{r\theta} &= r^{\lambda-1}\left[\lambda F'(\theta^*)\right]
\end{aligned} \tag{B.19}$$

where the primes denote derivate with respect to θ^* . If the crack faces are traction free, $\sigma_{\theta\theta}(0) = \sigma_{\theta\theta}(2\pi) = \tau_{r\theta}(0) = \tau_{r\theta}(2\pi) = 0$ and it implies the following boundary conditions:

$$F(0) = F(2\pi) = F'(0) = F'(2\pi) = 0 \tag{B.20}$$

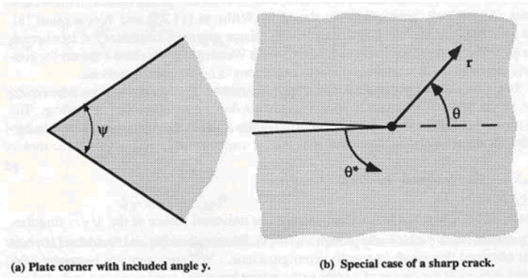

Figure B.1: Plate corner configuration analyzed by Williams.

Assuming that the constants in Eq.B.18 are non zero in the most general case, the boundary conditions can only be satisfied when:

$$\sin(2\pi\lambda) = 0 \text{ thus } \lambda = \frac{n}{2} \text{ where } n = 1, 2, 3, ... \tag{B.21}$$

There are an infinite numbers of λ values that satisfy the boundary conditions; the most general solution to a crack problem, is a polynomial of the form:

$$\Phi = \sum_{n=1}^{N} \left[r^{\frac{n}{2}+1} F\left(\theta^*, \frac{n}{2}\right) \right] \tag{B.22}$$

and the relative stresses are given by:

$$\sigma_{ij} = \frac{\Gamma_{ij}\left(\theta^*, -\frac{1}{2}\right)}{\sqrt{r}} + \sum_{m=0}^{M} \left[r^{\frac{m}{2}} \Gamma_{ij}\left(\theta^*, m\right) \right] \tag{B.23}$$

where Γ is a function that depends on F and its derivatives. The order of the polynomial stress function , N, must be sufficient to model the stresses in all region of the body. When $r \to 0$, the first term in Eq.B.23 approaches infinity, while the higher order of the terms remain finite (when $m = 0$) or approach zero (for $m > 0$). Thus the higher order terms are negligible close to the crack tip, and the stress exhibits a $\frac{1}{\sqrt{r}}$ singularity. By applying Eq.B.20 in Eq.B.16 , it is possible to eliminate two constants, resulting in:

$$\Phi\left(r, \theta\right) = r^{\frac{n}{2}+1} \left\{ c_3 \left[\sin\left(\frac{n}{2} - 1\right)\theta^* - \frac{n-2}{n+2} \sin\left(\frac{n}{2} + 1\right)\theta^* \right] \right\}$$
$$r^{\frac{n}{2}+1} \left\{ c_4 \left[\cos\left(\frac{n}{2} - 1\right)\theta^* - \cos\left(\frac{n}{2} + 1\right)\theta^* \right] \right\} \tag{B.24}$$

for a given value of n. The following stress function is obtained for the first few values of n, by substituting $\theta = \theta^* - \pi$ into Eq.B.24:

$$\Phi(r,\theta) = r^{\frac{3}{2}}\left[s_1\left(-\cos\frac{\theta}{2} - \frac{1}{3}\cos\frac{3\theta}{2}\right) + t_1\left(-\sin\frac{\theta}{2} - \sin\frac{3\theta}{2}\right)\right]$$
$$+s_2 r^2 (1-\cos 2\theta) + O\left(r^{\frac{\theta}{2}}\frac{\theta}{2}\right) + . \tag{B.25}$$

where s_i, t_i are constants to be defined. The stresses are given by:

$$\sigma_{rr} = \frac{1}{4\sqrt{r}}\left\{s_1\left[-5\cos\frac{\theta}{2} + cos\frac{3\theta}{2}\right] + t_1\left[-5\sin\frac{\theta}{2} + 3\sin\frac{3\theta}{2}\right]\right\} +$$
$$+4s_2\cos^2\theta + O\left(r^{\frac{1}{2}}\right) + ...$$
$$\sigma_{\theta\theta} = \frac{1}{4\sqrt{r}}\left\{s_1\left[-3\cos\frac{\theta}{2} - cos\frac{3\theta}{2}\right] + t_1\left[-3\sin\frac{\theta}{2} + 3\sin\frac{3\theta}{2}\right]\right\} +$$
$$+4s_2\sin^2\theta + O\left(r^{\frac{1}{2}}\right) + ...$$
$$\tau_{r\theta} = \frac{1}{4\sqrt{r}}\left\{s_1\left[-\sin\frac{\theta}{2}\sin\frac{3\theta}{2}\right] + t_1\left[\cos\frac{\theta}{2} + 3\cos\frac{3\theta}{2}\right]\right\} +$$
$$-2s_2\sin 2\theta + O\left(r^{\frac{1}{2}}\right) + \tag{B.26}$$

The constant s_1, t_1 can be replaced by the Mode I and Mode II stress intensity factors, respectively:

$$s_1 = -\frac{K_I}{\sqrt{2\pi}}; t_1 = \frac{K_{II}}{\sqrt{2\pi}} \tag{B.27}$$

The crack tip stress fields for symmetric loading, Mode I, are given by:

$$\begin{aligned}
\sigma_{rr} &= \frac{K_I}{\sqrt{2\pi r}}\left(\frac{5}{4}\cos\frac{\theta}{2} - \frac{1}{4}\cos\frac{3\theta}{2}\right)\\
\sigma_{\theta\theta} &= \frac{K_I}{\sqrt{2\pi r}}\left(\frac{3}{4}\cos\frac{\theta}{2} + \frac{1}{4}\cos\frac{3\theta}{2}\right)\\
\tau_{r\theta} &= \frac{K_I}{\sqrt{2\pi r}}\left(\frac{1}{4}\sin\frac{\theta}{2} + \frac{1}{4}\sin\frac{3\theta}{2}\right)
\end{aligned} \tag{B.28}$$

The singular stress field for Mode II is given by:

$$\begin{aligned}
\sigma_{rr} &= \frac{K_{II}}{\sqrt{2\pi r}}\left(-\frac{5}{4}\sin\frac{\theta}{2} + \frac{3}{4}\sin\frac{3\theta}{2}\right)\\
\sigma_{\theta\theta} &= \frac{K_{II}}{\sqrt{2\pi r}}\left(-\frac{3}{4}\sin\frac{\theta}{2} - \frac{3}{4}\sin\frac{3\theta}{2}\right)\\
\tau_{r\theta} &= \frac{K_{II}}{\sqrt{2\pi r}}\left(\frac{1}{4}\cos\frac{\theta}{2} + \frac{3}{4}\cos\frac{3\theta}{2}\right)
\end{aligned} \tag{B.29}$$

Converting Eq.B.28 and Eq.B.29 in Cartesian coordinates we obtain the equations given in the referred section. The accepted definition of stress intensity factor comes from the Irwin work [75], and it quantifies the amplitude of Mode I singularity with $\sqrt{GE}$, where G is the energy relies rate given in the Griffith criterion. Westergaard [76] showed that many problems could be solved by introducing a complex function $Z(z)$, where:

$$z = x + iy; i = \sqrt{-1} \tag{B.30}$$

The Westergaard stress function is related to Airy function by:

$$\Phi = Re\bar{Z} + yIm\bar{Z}; i = \sqrt{-1} \tag{B.31}$$

where $\bar{Z}$ represent the integration with respectto z. Applying Eq.B.7 gives:

$$\sigma_{xx} = ReZ + yImZ'\sigma_{yy} = ReZ + yImZ'\tau_{xy} = -yReZ' \tag{B.32}$$

The imaginary part of stresses vanish when $y = 0$. Also the shear stress vanishes when $y = 0$, implying that the crack plane is principal plane. Thus the stresses are symmetric about $\theta = 0$. Subsequent modification generalized the Westergaard approach to be applicable to a wider range of cracked configurations. If we apply this consideration in the situation showed in Fig.3.5, we obtain:

$$Z(z) = \frac{S_z}{\sqrt{z^2 - a^2}} \tag{B.33}$$

where S is the remote stress and a is half crack length. Consider the crack plane where $y = 0$: for $-a < x < a$, Z is pure imaginary, while Z is real for $\mid x \mid > \mid a \mid$. The normal stresses on the crack plane are given by:

$$\sigma_{xx} = \sigma_{yy} = ReZ = \frac{S_z}{\sqrt{z^2 - a^2}} \tag{B.34}$$

Considering the horizontal distance from each crack tip:

$$x^* = x - a \tag{B.35}$$

the following relationship is obtained by substitution in Eq.B.34:

$$\sigma_{xx} = \sigma_{yy} = \frac{S\sqrt{a}}{\sqrt{2x^*}} \text{ for } x^* << a \tag{B.36}$$

One advantage of this approach is that it relates the local stress to the global stress and crack size. From Eq.B.28 the stresses on the crack plane ($\theta = 0$) are given by:

$$\sigma_{rr} = \sigma_{\theta\theta} = \sigma_{xx} = \sigma_{yy} = \frac{K_I}{\sqrt{2\pi x^*}} \tag{B.37}$$

Comparing Eq.B.36 and Eq.B.37

$$K_I = \sigma\sqrt{\pi a} \tag{B.38}$$

which is the common accepted form for stress intensity factor Mode I. Substituting Eq.B.38 in Eq.B.34 it gives:

$$Z(z^*) = \frac{K_I}{\sqrt{2\pi z^*}} \text{ where } z^* = z - a \tag{B.39}$$

It is possible to solve for the singular stresses at the other angles by making the following substitution in Eq.B.39:

$$z^* = re^{i\theta} \text{ where } r^2 = (x-a)^2 + y^2; \theta = \tan^{-1}\left(\frac{y}{y-a}\right) \tag{B.40}$$

which leads to equation:

$$\begin{aligned}
\sigma_{xx} &= \frac{K_I}{\sqrt{2\pi r}}\cos\frac{\theta}{2}\left[1 - \sin\frac{\theta}{2}\sin\frac{3\theta}{2}\right] \\
\sigma_{yy} &= \frac{K_I}{\sqrt{2\pi r}}\cos\frac{\theta}{2}\left[1 + \sin\frac{\theta}{2}\sin\frac{3\theta}{2}\right] \\
\tau_{xy} &= \frac{K_I}{\sqrt{2\pi r}}\cos\frac{\theta}{2}\sin\frac{\theta}{2}
\end{aligned} \tag{B.41}$$

that are the same gave in the referred section.

With similar considerations it is possible to obtain the equations referred to mode II given in the referred section.

For Mode III it can be shown that:

$$\begin{aligned}
\sigma_{xx} &= \frac{K_{III}}{\sqrt{2\pi r}}\left(-\sin\frac{\theta}{2}\right) \\
\sigma_{xz} &= \frac{K_{III}}{\sqrt{2\pi r}}\left(\cos\frac{\theta}{2}\right)
\end{aligned} \tag{B.42}$$

coming from similar consideration.

Appendix C

EPFM Mathematical Foundations

In him description, Rice presents a mathematical proof of the path independence of the j contour integral. It is useful to remake the same passage he did.
Rice began by evaluating J along a closed contour, Γ^* (Fig.C.1):

$$\mathbf{J}^* = \int_{\mathbf{\Gamma}^*} \left(\mathbf{wdy} - \mathbf{T_i} \cdot \frac{\delta \mathbf{u_i}}{\delta \mathbf{x}} \mathbf{ds} \right) \tag{C.1}$$

where the various terms in this equation are defined in the respective section. By use the theorem of the divergence, Rice converts the upper equation into an area integral:

$$\mathbf{J}^* = \int_{\mathbf{A}^*} \left[\frac{\delta \mathbf{w}}{\delta \mathbf{x}} - \frac{\delta}{\delta \mathbf{x_j}} \left(\sigma_{\mathbf{ij}} \frac{\delta \mathbf{u_i}}{\delta \mathbf{x}} \right) \right] \mathbf{dxdy} \tag{C.2}$$

where A^* is the area enclosed by Γ^*. From the definition of strain energy density:

$$\frac{\delta \mathbf{w}}{\delta \mathbf{x}} = \sigma_{\mathbf{ij}} \frac{\delta \varepsilon_{\mathbf{ij}}}{\delta \mathbf{x}} \tag{C.3}$$

only if we assume elastic conditions. Combining the strain-displacement relationship with the above equation:

$$\frac{\delta \mathbf{w}}{\delta \mathbf{x}} = \frac{\mathbf{1}}{\mathbf{2}} \sigma_{\mathbf{ij}} \left[\frac{\delta}{\delta \mathbf{x}} \left(\frac{\delta \mathbf{u_i}}{\delta \mathbf{x_j}} \right) + \delta \delta \mathbf{x} \left(\frac{\delta \mathbf{u_j}}{\delta \mathbf{x_i}} \right) \right] = \sigma_{\mathbf{ij}} \frac{\delta}{\delta \mathbf{x_j}} \left(\frac{\delta \mathbf{u_i}}{\delta \mathbf{x}} \right) \tag{C.4}$$

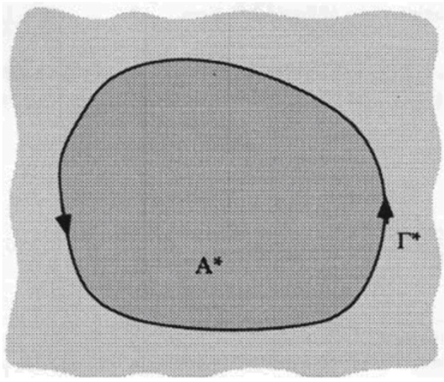

Figure C.1: Closed contour Γ^*, in a two dimensional solid.

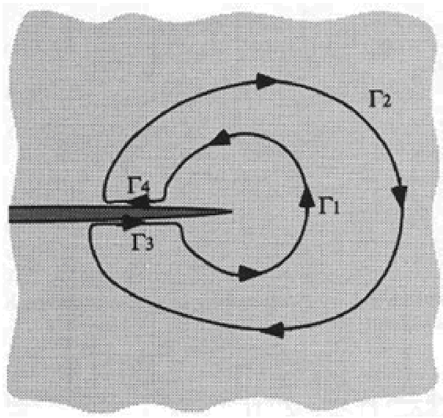

Figure C.2: arbitrary contours around a crack tip of a crack connected by two segments.

since $\sigma_{ij} = \sigma_{ji}$. Applying the equilibrium condition:

$$\sigma_{\mathbf{ij}} \frac{\delta}{\delta \mathbf{x_j}} = \left(\frac{\delta \mathbf{u_i}}{\delta \mathbf{x}} \right) = \frac{\delta}{\delta \mathbf{x_j}} \left(\sigma_{\mathbf{ij}} \frac{\delta \mathbf{u_i}}{\delta \mathbf{x}} \right) \tag{C.5}$$

which is identical with the second term in the bracket in J equation (Eq.C.2). Rice shows in this way that the second term of Eq.C.2 is equal to zero for any closed contour. Consider now two arbitrary contours around a crack tip (Fig.C.2). If $\Gamma 1$ and $\Gamma 2$ are connected by segments along the crack face ($\Gamma 3$ and $\Gamma 4$), a closed line is formed and in according with the previous considerations, $J = 0$ Therefore, any arbitrary path around a crack will yield the same value of J; J is path-independent. Now we want to introduce J as a non-linear elastic release rate by considering a two dimensional cracked body bounded by a curve, Γ (Fig.C.3), where A' denote the area of the body. In

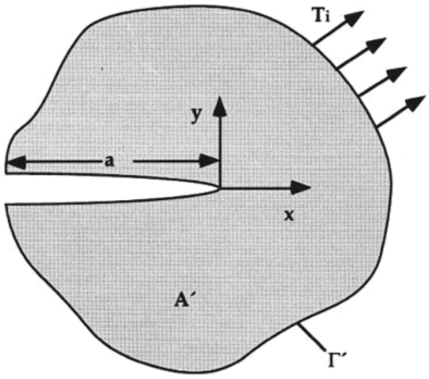

Figure C.3: A two dimensional cracked body bounded by a curve Γ'.

absence of body forces:

$$\mathbf{\Pi} = \int_{\mathbf{A'}} \mathbf{wdA} - \int_{\mathbf{\Gamma'}\prime} \mathbf{T_i u_i dS} \tag{C.6}$$

where Γ'' is the portion of the contour on which tractions are defined. With crack extension we have a potential energy change, described by:

$$\frac{\mathbf{d\Pi}}{\mathbf{da}} = \int_{\mathbf{A'}} \frac{\mathbf{dw}}{\mathbf{da}}\mathbf{dA} - \int_{\mathbf{\Gamma'}} \mathbf{T_i}\frac{\mathbf{du_i}}{\mathbf{da}}\mathbf{dS} \tag{C.7}$$

and the line integration in the above equation can be performed over the entire contour, Γ', because $\frac{du_i}{da} = 0$ over the region where displacements are specified; also over the region where the tractions are specified. When the crack growth, the coordinate axis moves and thus a derivative with respect to crack length could be written as:

$$\frac{\mathbf{d}}{\mathbf{da}} = \frac{\delta}{\mathbf{da}} + \frac{\delta\mathbf{x}}{\delta\mathbf{a}}\frac{\delta}{\delta\mathbf{x}} = \frac{\mathbf{d}}{\mathbf{da}} - \frac{\delta}{\delta\mathbf{x}} \tag{C.8}$$

Applying this result in Eq.C.7, it gives:

$$\frac{\mathbf{d\Pi}}{\mathbf{da}} = \int_{\mathbf{A'}} \left(\frac{\mathbf{dw}}{\mathbf{da}} - \frac{\mathbf{dw}}{\mathbf{dx}}\right)\mathbf{dA} - \int_{\mathbf{\Gamma'}} \mathbf{T_i}\left(\frac{\mathbf{du_i}}{\mathbf{da}} - \frac{\mathbf{du_i}}{\mathbf{dx}}\right)\mathbf{dS} \tag{C.9}$$

and with the assumption previously introduced we obtain:

$$\frac{\delta\mathbf{w}}{\delta\mathbf{a}} = \left(\frac{\delta\mathbf{w}}{\delta\varepsilon_{\mathbf{ij}}}\right)\frac{\delta\varepsilon_{\mathbf{ij}}\delta\mathbf{a}}{=}\sigma_{\mathbf{ij}}\frac{\delta}{\delta\mathbf{x_j}}\left(\frac{\delta\mathbf{u_i}}{\delta\mathbf{a}}\right) \tag{C.10}$$

Invoking the principle of virtual work:

$$\int_{\mathbf{A'}} \sigma_{\mathbf{ij}}\frac{\delta}{\delta\mathbf{x_j}}\left(\frac{\mathbf{u_i}}{\delta\mathbf{a}}\right)\mathbf{dA} = \int_{\mathbf{\Gamma'}} \mathbf{T_i}\left(\frac{\delta\mathbf{u_i}}{\delta\mathbf{a}}\right)\mathbf{dS} \tag{C.11}$$

and by substitution in the line integral equation:

$$\mathbf{\frac{d\Pi}{da}} = \int_{\mathbf{\Gamma'}} \mathbf{T_i} \left(\frac{\delta \mathbf{u_i}}{\delta \mathbf{x}} \right) \mathbf{dS} - \int_{\mathbf{A'}} \left(\frac{\delta \mathbf{w}}{\delta \mathbf{x}} \right) \mathbf{dA} \tag{C.12}$$

Applying the divergence theorem:

$$-\mathbf{\frac{d\Pi}{da}} = \int_{\mathbf{\Gamma'}} \left(\mathbf{wdy} - \mathbf{T_i} \frac{\delta \mathbf{u_i}}{\delta \mathbf{x}} \right) \mathbf{dS} \tag{C.13}$$

The J contour integral is equal to the energy release rate for a linear or non-linear material under quasi-static conditions.

Appendix D

Matlab for Cam Design

```
acc = e_max/(1/18*pi^2);

%T0 = 5*pi/180;
T1 = 170*pi/180;
T2 = 200*pi/180;
T3 = 230*pi/180;
T4 = 260*pi/180;
T5 = 270*pi/180;
T6 = 300*pi/180;
T7 = 330*pi/180;
theta1 = [0:0.001:T1];
rho1 = 0.02;

theta2 = [0:0.0001:pi/6];
theta3 = [pi/6:0.0001:pi/3];
theta4 = [pi/3:0.0001:pi/2];
theta5 = [0:0.0001:pi/18];


for i=1:length(theta1)
    rho(i) = rho1;
end
```

```
for i=1:length(theta2)
    rho2(i) = rho1 + 0.5*acc*(theta2(i))^2;
    rho6(i) = rho1+e_max - 0.5*acc*(theta2(i))^2;
end

for i=1:length(theta3)
    rho3(i) = rho1 + acc*(pi/6)*(theta3(i)-pi/12);
    rho7(i) = rho1+e_max - acc*(pi/6)*(theta3(i)-pi/12);
end

for i=1:length(theta4)
    rho4(i) = rho1 + acc*(pi/6)*(theta4(i)-pi/12)+
              -acc/2*(theta4(i)-pi/3)^2;
    rho8(i) = rho1+e_max - (acc*(pi/6)*(theta4(i)-pi/12)+
              -acc/2*(theta4(i)-pi/3)^2);
end

for i=1:length(theta5)
    rho5(i) = rho1+e_max;
end

radius=[rho rho2 rho3 rho4 rho5 rho6 rho7 rho8];
theta = [theta1 theta2+T1 theta3+T2-pi/6 theta4+T3-pi/3
        theta5+T4 theta2+T5 theta3+T6-pi/6 theta4+T7-pi/3];

figure
grid on
polar(theta, radius)
```

Bibliography

[1] ASTM E 1150-1987, Standard Definitions of Fatigue, 1995 Annual Book of Standards, ASTM.(1995), p 753 - 762.

[2] Raymond Browell; Calculating and Displaying Fatigue Results; Product Manager New Tecnologies, Ansys, Inc.

[3] Davidson, D.L. and Lankford, J. (1981); The Effect of Water Vapor on Fatigue Crack Tip Stress and Strain Range Distribution and the Energy Required for Crack Propagation in Low Carbon Steel; International Journal of Fracture 17, 257-75.

[4] Morris E. Fine and Yip-Wah Chung, R.R. McCormick School of Engineering and Applied Science, Department of Materials Science and Engineering, Northwestern University.

[5] A.H. Cottrell and D. Hull, PROC. R. SOC. (London) A, Vol A242, 1957, P 211.

[6] Callister, William D. Jr.; Fundamentals of Materials Science and Engineering; John Wiley and Sons, Inc. Danvers, MA. (2005).

[7] C. Laird and D.J. Duquette; Mechanisms of Fatigue Crack Nucleation; Corrosion Fatigue, National Association of Corrosion Engineers, P 88.

[8] P. Lukas, M. Klesnil, and J. Krejci, Phys. Status Solidi, Vol 27, 1968, P 545.

[9] P. Neumann; ACTA Metall., Vol 17, 1969, P 1219.

[10] N. Thompson, N.J. Wadsworth, and N. Louat, Philos. Mag., Vol 1, 1956, P 113.

[11] Forsyth, P.J.E.; The Physical Basis of Metal Fatigue; Blackie and Son, London (1969).

[12] E.O.Hall, Proc. Phys. Soc., Ser. B, Vol. 64, pp. 747-753, (1951).

[13] N.J.Petch; Iron and Steel Institute, pp. 25-28, May 1953.

[14] Bullen, W.P., Head, A.K. and Wood, W.A.; Structural changes during the fatigue of materials; Proc. Roy. Soc. Vol. A200 (1903), pp. 241-250.

[15] A.E., Hedlund, A., Zhao, W., Fathalla, A., Weiss, B. and Stickler, R.; Short fatigue crack growth in Al 2024 and Al 7475. Behaviour of short fatigue cracks; Blom; Symp., Sep. 1985, Sheffield. EGF 1, MEP (1986), pp. 37-66.

[16] P.C. PARIS, In Proc. 10TH Sagamore Army Materials Research Conf., Syracuse University Press, 1964, P 107.

[17] Ramesh V. Marrey, Robert Burgermeister, Randy B. Grishaber, R.O. Ritchie; Fatigue and life prediction for cobalt-chromium stents: A fracture mechanics analysis;2005 Elsevier Ltd.

[18] Whler, A.; Verusche ber die Festigkeit der Eisenbahnwagenachsen. Zeitschrift fr Bauwesen 10; English Summary (1867), Engineering 4,
160-1.

[19] ASTM Standards E466-E468.

[20] Basquin, O.H. (1910); The exponential law of endurance tests; Proceedings of the American Society for Testing and Materials 10, 625-30.

[21] Gary B. Marquis; LUT Fatigue Design.

[22] Morrow, J.D.;Fatigue Designe Handbook-Advances in Engineering, vol.4, Sec.3.2, pp.21-29; Warrendale, PA: Society of Automotive Engineers.

[23] Technical Report on Fatigue Properties, SAE J1099, Society of Automotive Engineers, 1985.

[24] ASTM E 606-92, Standard Practice for Strain Controlled Fatigue Testing, Annual Book of ASTM Standards, Vol 03.01, ASTM, 1995.

[25] J.A. Bannantine, J.J. Comer, and J.L. Handrock; Fundamentals of Metal Fatigue Analysis; Prentice-Hall, 1990.

[26] A.A. Griffith, The Phenomena of Rupture and Flow in Solids, Phil. Trans. Roy. Soc. London, Series A, Vol 221, 1920, p 163-198.

[27] A.A. Griffith, The Theory of Rupture, Proc. First International Congress for Applied Mechanics, Delft, The Netherlands, 1924, p 55-63.

[28] G.R. Irwin; Fracture Dynamics; Trans. ASM, Vol 40A, 1948, p 147-166.

[29] H. Tada, P.C. Paris, and G.R. Irwin; The Stress Analysis of Cracks Handbook; 2nd ed., Paris Productions Inc., St.Louis, MO, 1985.

[30] Standard Method for Plane-Strain Fracture Toughness Testing of Metallic Materials; ASTM E 399-91, ASTM, Vol 3.01, 1991, p 488-512.

[31] Rice, J.R.; A path independent integral and the approximate analysis of strain concentration by notches and cracks; Journal of Applied Mechanics 35, 379-86.

[32] Hutchinson, J.W.; Fundamentals of the phenomenological theory of non-linear fracture mechanics; Journal of Applied Mechanics 50, 1042-51.

[33] Suresh, S and Ritchie, R.O.;Propagation of short fatigue cracks; International Metals Review 29, 445-76.

[34] Ritchie, R.O. and Lankford, J.; Small Fatigue Cracks; the Metallurgical Society of the American Institute of Mining, Metallurgical and Petroleum Engineering.

[35] R. Craig McClung, Kwai S. Chan, Stephen J. Hudak, Jr., and David L. Davidson; Behavior of Small Fatigue Cracks; Southwest Research Institute.

[36] A state-of-the-art review on fatigue life prediction methods for metal structures; Weicheng Cui; School of Naval Architecture and Ocean Engineering, Shanghai Jiao Tong University, 1954 Huasham Road, Shanghai 200030, China.

[37] Hobson PD, Brown MW, de los Rios ER (1986) In: Miller KJ, de los Rios ER (eds) EGF (ESIS) Publication No. 1; The behavior of short fatigue cracks. Mechanical Engineering Publications; London, pp 441-459.

[38] Navarro A, de los Rios ER (1988); A micro-structurally short fatigue crack growth equation. Fatigue Fract Eng Mater Struct 11:383-396.

[39] Davidson D.L., Chan K.S., and McLung R.C.; Metall. and Mater. Trans., Vol. 27A, 1996, P 2540-2556.

[40] J.C. Newman, JR.; Fracture Mechanics Parameters for Small Fatigue Cracks, Small Crack Test Methods, STP 1149, J.M. Larsen and J.E. Allison, ED., American Society for Testing and Materials, 1992, P 6-33.

[41] Dugdale, D.S.; Yielding of steel sheets containing slits; Journal of the Mechanics and Physics of Soids 8, 100-8.

[42] Mc Lung, R.C. and Sehitoglu, H.; ASME J. Engng.Mater. Technol., Vol. 113, 1991, P 15-22.

[43] Gangloff, R.P.; Metall. Trans. A, Vol. 16, 1985, P 953-969.

[44] Gangloff, R.P. and wei, R.P.; Small Crack-Environment Interactions: the Hydrogrn Embrittlement Perspective, Small Fatigue Cracks; R.O. Ritchie and J. Lankford, ED., the Metallurgical Society, 1986, P 239-264.

[45] Vasudevan AK, Sadananda K, Louat N.; A review of crack closure, fatigue crack threshold and related phenomena; Mater. Sci. Eng. A 1994;A188:1-22.

[46] L. Lawson, E.Y. Chen, M. Meshii; Near-threshold fatigue: a review; International Journal of Fatigue 21 (1999) S15-S34.

[47] Christensen RH.; Fatigue crack growth affected by metal fragments wedged between opening-closing crack surfaces; Appl. Mater. Res. 1963, 207-10.

[48] Elber W.; Fatigue crack closure under cyclic tension. Eng Fract Mech 1970;2:37-45.

[49] Elber W. The significance of fatigue crack closure. In: Damage tolerance in aircraft structures, ASTM STP-486. Philadelphia (PA, USA): American Society for Testing and Materials, 1971: 230-42.

[50] Ritchie RO. Near threshold fatigue crack propagation in steels, review 245. Int Metals Rev 1979;5-6:205-30.

[51] Anuschewski P, Detzel W, Horstmann H, Pfuff M, Wellenkotter B.; AC potential measurement of hydrogen-induced geometrical crack closure during fatigue crack growth. In: Hydrogen effects on material behavior. Warrendale (PA, USA): The Minerals, Metals and Materials Society, 1990: 929-37.

[52] Schmidt RA, Paris P. Threshold for fatigue crack propagation and the effects of load ratio and frequency. Progress in flaw growth and fracture toughness testing, ASTM STP 536.

Philadelphia (PA, USA): American Society for Testing and Materials, 1973: 79-94.

[53] Ritchie, R.O., Suresh, S. and Moss, C.M. (1980); Near-threshold fatigue crack growth in 2 Cr - 1 Mo pressure vessel steel in air and hydrogen.

[54] Suresh, S., Zamiski, G.F. and Ritchie, R.O.; Oxide-induced crack closure: an explanation for near-threshold corrosion-fatigue crack growth behavior; Metallurgical Transactions 12A, 1435-43.

[55] Suresh, S., Ritchie, R.O.; Near-threshold fatigue crack propagation: a perspective on the role of crack closure. In Fatigue Crack Growth Threshold Concepts; eds. D.L. Davidson and S. Suresh, pp. 227-61. Warrendale: The Metallurgical Society of the American Institute of Mining, Mineral and Petroleum Engineers.

[56] R.P. Gangloff and R.P. Wei, Metall. Trans. A, Vol. 8A, 1977, P 1043.

[57] P.S. Pao; Mechanisms of Corrosion Fatigue; Materials Science and Technology Division, Naval Research Laboratory.

[58] H.L. Logan, J. Res. Natl. Bur. Stand.; VOL 48, 1952, P 99.

[59] W. Cullen, G. Gabetta, and H. Hanninen, A Rewiew of the Models and Mechanisms for the Environmentally-Assisted Crack Growth of Pressure Vessel and Piping Steels in PWR Environments; Nureg/CR-4422 MEA-2078, U.S. Nuclear Regulatory Commission, Dec. 1985.

[60] Van der Sluys, W. and Emanuelson, R.; Overview of Data Trends in Cyclic Crack Growth Results in LWR Environments, Proc. 2ND IAEA specialists Meeting on Subcritical Crack Growth (Sendai, Japan); U.S. Nuclear Regulatory Commission; 15-17 May, 1985.

[61] Scott, P.M. and Truswell, A.E.; Corrosion Fatigue Crack Growth in Reactor Pressure Vessel Steels in PWR Primary Water; J. Pressure Vessel Steels Technol, Vol. 105, 1983, P. 245-254.

[62] Pao,P.S. , Bayles, R.A. and Yoder, G.R.; J. Eng. Mater. Technol. (Trans. ASME); Vol. 113, 1991, P 125.

[63] Rolfe, S.T. and Barsom, J.M.; Fracture and Fatigue Control in Structures; Prentice-Hall, 1977.

[64] Gerberich, W.W., Birat, J.P. and Zacky, V.F.; Corrosion Fatigue: Chemestry, Mechanics and Microstructure; National Association of Corrosion Engineers, 1971, P. 396.

[65] Simmons, G.W., Pao P.S. and Wei, R.P.; Metall. Trans. A, Vol. 9A, 1978, P. 1147.

[66] El-Hakeem, H. A. and Culver, L. E.; The superposition model and environmental crack propagation in low-density polyethylene.

[67] Schtz W.; A history of fatigue; Eng. Fract. Mech. 1996; 54:263-300.

[68] Madayag, A.F.; ED., Metal Fatigue, Wiley, 1969.

[69] ASTM Standard E 606; Standard Recommended Practice for Constant Amplitude Low Cycle Fatigue Testing.

[70] ASTM Standard E 647; Standard Test Method for Constant Load Amplitude Fatigue Crack Growth Rates Above $110E-08$ Meters/Cycle.

[71] Bucci, R.J.; Effect of residual stress on Fatigue Crack Growth Rate Measurement; In STP 743, ASTM, 1981, P 28-47.

[72] Koster W.; Effects of Residual Stress on Fatigue of Structural Alloys, Practical Alloys, Practical Applications of Residual Stress Technology; ASM International, 1991, P. 1-10.

[73] Williams, M.L.; On the Stress Distribution at the base of a stationary Crack; Journal of Applied Mechanics, Vol. 24, 1957, pp. 109-114.

[74] Williams, M.L.; stress Singularities Resulting from Various Boundary Conditions in Angular Corners of Plates in Extension; Journal of Applied Mechanics, Vol 74, 1952, pp. 526-528.

[75] Irwin. G.R.; Analysis of Stress and Strains near the end of a Crack Traversing a Plate; Journal of Applied Mechanics, Vol. 24, 1957, pp.361-364.

[76] Westergaard, H.M.; Bearing Pressure and Cracks; Journal of Applied Mechanics, Vol. 6, 1939,pp. 49-53.

[77] A.R. Pelton et Al.; Optimisation of processing and properties of medical grade Nitinol wire.

[78] John M. Barsom, Stanlet T. Rolfe; Fracture and Fatigue Control in Structures (2Nd Ed).

Ringraziamenti

Finalmente posso scrivere l'unica pagina che ho sempre avuto in mente.
Non avrei mai potuto raggiungere questo risultato se non fossi circondato da persone eccezionali.
Prima di tutto voglio ringraziare la mia famiglia, che mi spinge sempre a cercare occasioni per crescere e migliorare.
A voi, mamma e papà, dovrei dire grazie per talmente tante cose che una vita non mi basterebbe, quindi vi abbraccio e per adesso vi dedico questo traguardo.
Ai miei fratelli, perchè siete le colonne su cui so di potermi appoggiare ogni volta che ne sento il bisogno.
Ringrazio Barbara, che mi ha sempre appoggiato, incoraggiato e soprattutto sopportato...
A Giro e Guido devo dire grazie, perchè il vostro esempio mi ha dato una valanga di motivazioni (e per un bel pò di altre cose che è meglio non scrivere...).
A Paolo, Gian, Zucca (il b.....n), Edo, lo Sbiru, Adri, la Vale, va un grazie per ogni splendido momento che abbiamo passato insieme.
Ad Alessandra, Chiara e Denise va buona parte del merito della mia laurea...
A Michele e Simone per l'amicizia e il supporto che mi hanno sempre dedicato.
A tutti quelli con cui mi sono divertito, con cui ho festeggiato o che semplicemente mi hanno regalato un sorriso...grazie davvero!